Department of Physics and Astronomy
University of Heidelberg

Bachelor Thesis in Physics
submitted by

Lars Henkelmann

born in Darmstadt (Germany)

2015

Optical Measurements of Vibration and Deformation of the Mu3e Silicon Pixel Tracker

This Bachelor Thesis has been carried out by Lars Henkelmann at the
Institute of Physics in Heidelberg
under the supervision of
Prof. Dr. André Schöning

Abstract

The Mu3e Experiment will search for the charged lepton flavor violating decay $\mu^+ \to e^+e^+e^-$ with a sensitivity of 10^{-16}. In a Standard Model extended by massive neutrinos, this decay is unobservable, with a branching ratio of 10^{-54}. Any signal would indicate new physics.
In order to reach this high sensitivity, a detector with good momentum, time and vertex resolution is necessary. Since the muons decay at rest, the decay particles have energies of $\leq 53\,\mathrm{MeV}$. Therefore, multiple Coulomb scattering dominates the spatial and thereby the momentum resolution. Thus, a low material budget is required. To fulfill this requirement, the planned silicon pixel tracker is a few hundred micrometer thin, and cooled with gaseous helium. Therefore, flow induced vibration or static deformation could impede spatial resolution.
In this thesis, the extent of these effects is investigated experimentally. Flow induced vibration is studied using a Michelson interferometer. The directly observed vibration amplitudes at the planned coolant flow velocity of $20\,\frac{\mathrm{m}}{\mathrm{s}}$ are below $10\,\mu\mathrm{m}$, the average amplitudes below $2\,\mu\mathrm{m}$. This is significantly smaller than the chip thickness of $50\,\mu\mathrm{m}$, and thus no limit to resolution. Static module deformations large enough ($100\,\mu\mathrm{m}$) to limit resolution were observed. However, they should not limit the resolution as long as the coolant flow is kept constant during alignment and measurement.

Zusammenfassung

Das Mu3e Experiment wird mit einer Sensitivität von 10^{-16} nach dem Leptonen-Flavor verletzenden Zerfall $\mu^+ \to e^+e^+e^-$ suchen. In einem um massive Neutrinos erweiterten Standardmodel ist dieser Zerfall mit einem Verzweigungsverhältnis von 10^{-54} nicht beobachtbar. Ein Signal wäre ein Hinweis auf neue Physik.
Um diese hohe Sensitivität zu erreichen, ist ein Detektor mit sehr hoher Vertex-, Zeit- und Impulsauflösung notwendig. Da die Myonen in Ruhe zerfallen, haben die Zerfallsprodukte Energien von 53 MeV oder kleiner. Daher dominiert Mehrfachstreuung die Ortsauflösung. Deswegen bedarf es eines geringen Materialbudgets des Detektors, um die notwendige Orts- und damit Impulsauflösung zu erreichen. Um diese Bedingung zu erfüllen, ist der geplante Silizium-Pixeltracker wenige hundert Mikrometer dünn und wird mit gasförmigem Helium gekühlt. Daher könnten Fluss-induzierte Vibration oder statische Verformung aufgrund des Flusses möglicherweise die Ortsauflösung einschränken.
In dieser Arbeit wird das Ausmaß dieser Effekte experimentell untersucht. Flussinduzierte Vibration wird mit einem Michelson-Interferometer untersucht. Die direkt beobachteten Vibrationensamplituden beim geplanten Kühlfluss von $20\,\frac{\mathrm{m}}{\mathrm{s}}$ sind kleiner als $10\,\mu\mathrm{m}$, die mittleren Amplituden kleiner als $2\,\mu\mathrm{m}$. Dies ist signifikant kleiner als die Chipddicke von $50\mu\mathrm{m}$, und daher keine Beschränkung der Auflösung. Statische Modulverformungen, die ausreichend groß sind ($100\,\mu\mathrm{m}$), um für die Auflösung relevant zu sein, wurden beobachtet. Allerdings sollten sie die Auflösung nicht beschränken, solange der Kühlfluss während der Detektorausrichtung und Messung konstant gehalten wird.

Contents

Chapter 1

Introduction

The standard model of particle physics is an extremely successful description of the fundamental constituents of matter and their interactions. However, there are reasons to believe that the standard model is just a (very good) approximation of a more fundamental theory that would, for example include quantum gravity, or could explain the matter-antimatter asymmetry seen in the observable universe.

One avenue of looking for physics beyond the standard model experimentally is the search for processes that do not conserve lepton flavor, which is a conserved quantum number within the standard model.

A possible process is the charged lepton flavor violating decay $\mu^+ \to e^+e^+e^-$, which is suppressed to unobservable levels in minimal extensions of the standard model that include neutrino mixing.

Mu3e is a planned experiment looking for this decay with a branching ratio sensitivity of 10^{-16}. In order to achieve this sensitivity large statistics and high vertex, timing and momentum resolution are required to reduce backgrounds. Momentum resolution is limited by multiple coulomb scattering in the active detector region, which depends strongly on the amount of material present. Therefore the detector and its cooling system are designed to keep the material budget minimal.

The detector is built to be extremely thin and light, and cooled by forced convection with gaseous helium flowing across the detector surface. This opens the question of how stable the detector setup is. The cause of concern is whether the planned cooling scheme causes the detector to vibrate or deform in ways which may reduce the vertex resolution of the detector.

That is the question investigated in this thesis. Chapter 2 gives a very brief overview of the standard model and motivates the search for lepton flavor violating decays. Chapter 3 discusses the lepton flavor violating decay $\mu^+ \to e^+e^+e^-$ and the planned search for it in the Mu3e experiment. Chapter 4 discusses the Michelson interferometer, which is the device used to do the measurements described in chapters 5, 6, and 8. Chapter 5 describes the measurement of the frequency response of the detector to mechanical excitation, to identify and avoid in the design dangerous resonant frequencies. Chapter 6 discusses the measurements of vibrations induced by the cooling flow. Chapter 7 contains the measure-

ments of the tilting of the detector surface as the detector is deformed by the cooling flow. Chapter 8 describes the complementary measurements of the detector deformation done using the Michelson interferometer. A brief summary and discussion of all the results gathered in the previous chapters is provided in chapter 9, as well as an outlook on problems not addressed in this thesis.

Chapter 2

Motivation and Background

2.1 The Standard Model of Particle Physics

The Standard Model of Particle Physics is a quantum field theory describing the fundamental constituents of matter and their interactions. The Standard model encompasses 12 fermions with their anti-fermions, all of which have spin $\frac{1}{2}$, four gauge bosons with spin 1, and the Higgs-Boson, with spin 0 (Fig. 2.1). [2]

The 12 fermions consist of six quarks and 6 leptons. The six leptons can again be divided in neutrinos, which carry no electrical charge, and the electron, muon and tau, which have a charge of 1. The fermions of the standard model are considered to make up ordinary matter, often via composite particles and bound states.

The four gauge bosons mediate the three fundamental interactions that are described in the Standard Model. The gluon is the gauge boson of the strong interaction. Only quarks interact strongly. The $W^{\pm}$- and Z-bosons are the mediators of the weak interaction. All elementary fermions interact weakly. The photon is the gauge boson of electromagnetic interaction, which all elementary fermions with the exception of the three neutrinos take part in. In the Higgs-Mechanism, the particle masses are explained by their interaction

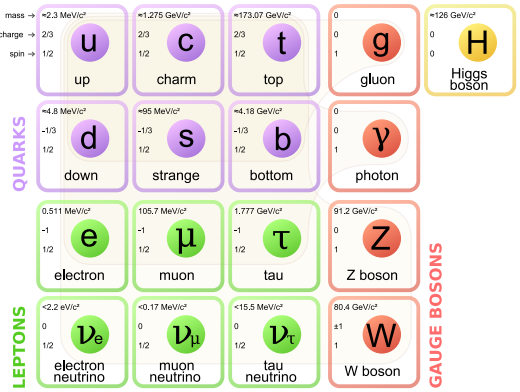

Figure 2.1: Elementary particles in the Standard Model[3]

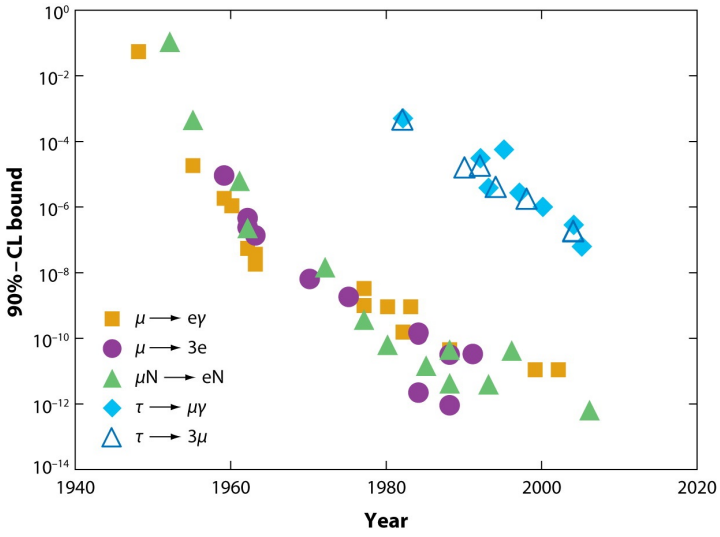

Figure 2.2: Record of LFV searches [4]

with the Higgs-field. The part of the Higgs-field not taking part in the Higgs-Mechanism has a particle excitation, the Higgs-Boson [2]. While gravity is considered a fundamental force of nature, the Standard Model does not include gravitational interaction.

The Standard model has been very successful in describing the fundamental constituents of matter and their interaction, but there are a number of problems and open questions associated with it. For example, as previously mentioned, it does not include gravity. Another open question is how dark matter and dark energy can be described to be in agreement with cosmological observations. So, there is room for new physics beyond the Standard Model.

2.2 Lepton Flavor Violation

Another example of a phenomenon not included in the standard model is Lepton Flavor Violation (LFV). In the Standard Model, each of the three families of leptons has an associated quantum number, called lepton flavor. In the standard model as it was sketched above, this quantum number is a conserved quantity. However, there have been observations that neutrinos do exist in states whose flavor changes over time. This process is called neutrino oscillation. It can be added to the above version of the standard model by allowing neutrinos small, but nonzero masses. Then, the eigenstate of a freely propagating neutrino - the mass eigenstate - is not equal to any of the three flavor eigenstates, but a superposition. This allows a neutrino to be prepared in one flavor eigenstate, propagate, and then be observed in another flavor eigenstate[1].[2]

Since lepton flavor violation is known to be possible, the question arises whether neu-

[1]this approach is also known as neutrino mixing

trino oscillation is the only physical process that does not conserve lepton flavor, or whether there are more. If any of the charged lepton states were to be observed to change its flavor directly (charged Lepton Flavor Violation, cLFV), this would be a clear indication of new physics. However, cLFV has not been observed yet. There have been searches for cLFV in a variety of decay channels, however, they were only able to provide exclusion limits on the branching ratios of these decay channels (Fig. 2.2).

Chapter 3

The Mu3e Experiment

Mu3e is a planned search for the LFV decay $\mu \to e^- e^+ e^+$. The projected branching ratio sensitivity is 10^{-16} at 90% confidence level in the final Phase of the experiment [1], making the experiment four orders of magnitude more sensitive than the SINDRUM experiment, which was the last experiment to search for the decay $\mu \to e^- e^- e^+$ and reached a branching ratio limit of $1.0 \cdot 10^{-12}$ [5].

3.1 The Decay $\mu \to eee$

3.1.1 Feynman-Diagrams

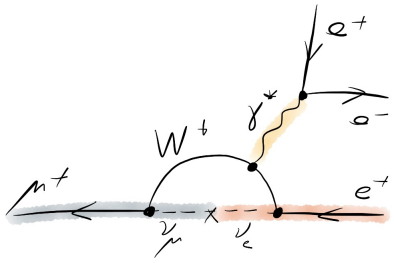

Figure 3.1: Feynman diagram of the lowest order contribution to $\mu \to eee$ in an extended SM [1]

The SM contribution to the signal decay $\mu \to eee$ is depicted in Fig. 3.1. Due to neutrino oscillation, there is a contribution to the signal decay in a minimally extended Standard Model that includes at least two massive neutrinos.

However, since there are two neutrinos with extremely low mass, and a rather heavy W boson running in the loop, the contribution has a branching ratio of $\ll 10^{-54}$ [1]. Thus, the contribution from neutrino mixing is unobservable.

Figure 3.2: Loop (left) and tree (right) level theoretical SUSY contributions to $\mu \to eee$ [1]

This in turn makes this decay an interesting channel to study with respect to new physics. New physics beyond the Standard Model could for example contribute via a penguin diagram with supersymmetric (SUSY) particles running the loop [1](an example is given in Fig. 3.2). Another possibility are tree-level diagrams involving new particles (Fig. 3.2).

3.1.2 Kinematics

For the contributions discussed above, there would be only a single vertex. Assuming that the muons are stopped before the decay (as will be the case for the Mu3e experiment), the rest frame of the muons will be the laboratory frame, so the summed momenta of all decay products should vanish:

$$\vec{p}_{total} = \sum \vec{p}_i = 0 \tag{3.1}$$

Accordingly, the total energy of the decay particles may never exceed the muon rest mass, meaning that the maximum energy of one decay particle is half the muon rest mass, or 53 MeV. Also, the decay particles must lie in a plane.

3.2 Background Decays

There are essentially two processes that can generate background to the signal previously discussed. One is accidental background, where different processes generate three particles with vertices close to each other, and a small time difference. The other is radiative decay with internal conversion, where all decay particles do share a common vertex and are produced simultaneously [1].

3.2.1 Accidental Background

Accidental background is due to more than one non-signal decay producing two positrons and one electron. A common source of positrons is the Michel decay $\mu^+ \to e^+\nu_e\bar{\nu}_\mu$. Elec-

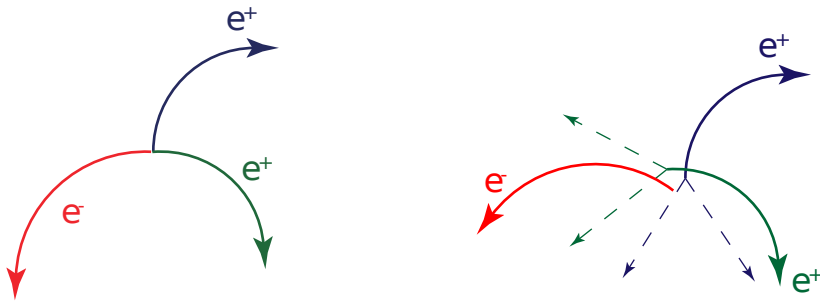

Figure 3.3: Topology of a signal decay (left) and an accidental background decay (right)

trons can be produced when a positron from e.g. a Michel decay scatters off an electron from the target material $e^+e^- \to e^+e^-$ (Bhabha-Scattering). Fig. 3.3 shows the topology of such accidental background events in comparison to that of an actual signal event. To suppress the accidental background contribution, good vertex and time resolutions are necessary to resolve the time difference and vertex separation.

3.2.2 Internal Conversion

In internal conversion events $\mu^+ \to e^+e^+e^-\nu_e\bar{\nu}_\mu$, a muon decays weakly, and an off-shell photon is emitted, which decays into an electron-positron pair (Fig. 3.4).

Due to the high branching ratio of this process, and the fact that the decay particles share a vertex and are generated simultaneously, this background cannot be addressed via vertex or time resolution. To suppress it, the decay neutrinos have to be reconstructed from the momenta of the decay positrons and the electron. Events where the momenta do not add up to zero and the total invariant mass is not equal to the muon rest mass are rejected. Fig. 3.5 shows how the achieved branching ratio sensitivity depends on the missing energy cut level. A very high energy resolution is required to achieve the sensitivity of 10^{-16} that the final phase of the experiment aims at.

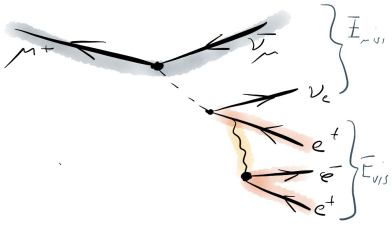

Figure 3.4: Feynman diagram of the lowest order $\mu^+ \to e^+e^+e^-\nu_e\bar{\nu}_\mu$ contribution [1]

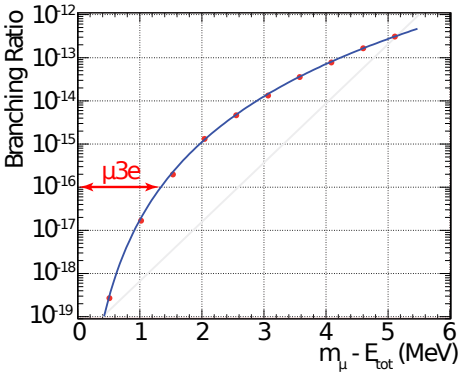

Figure 3.5: The energy cut dependency of the branching ratio sensitivity [6]

3.3 The Mu3e Detector

3.3.1 Concept and Geometry

As discussed in the previous section, the Mu3e experiment requires good vertex and timing resolution, in addition to excellent momentum resolution, in order to suppress the background. This is reflected in the detector design (Figs. 3.6 and 3.7).

A high intensity muon beam is stopped in a hollow double cone target. The target stops more than 80 % of the incoming muons. At the same time the material budget stays very low. The 2 cm wide and 10 cm double cone also serves to spread the decay vertices along its length, making vertex separation easier.

Around the target, an inner double layer of silicon pixel detector modules allows position measurements leading to an expected vertex resolution of about 200μm [1]. The innermost layer (layer 1) has a radius of 2.4 cm, while the outer layer (layer 2) has a radius of 3.0 cm.

The inner double layer is surrounded by an outer double layer of silicon pixel detectors. The outer two layers have radii of 7.3 cm (layer 3) and 8.5 cm (layer 4). The outer double

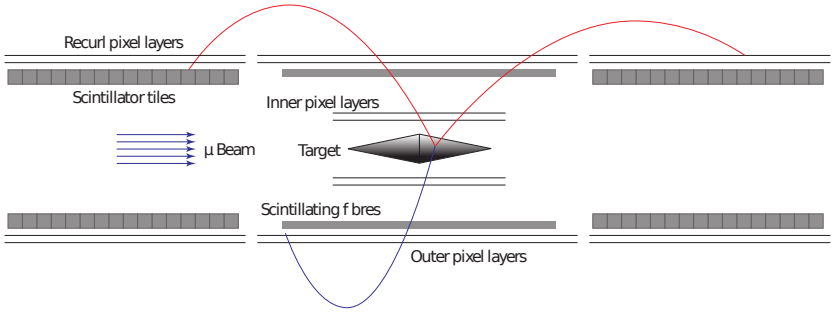

Figure 3.6: Schematic of the detector geometry viewed transverse to the beam axis [1]

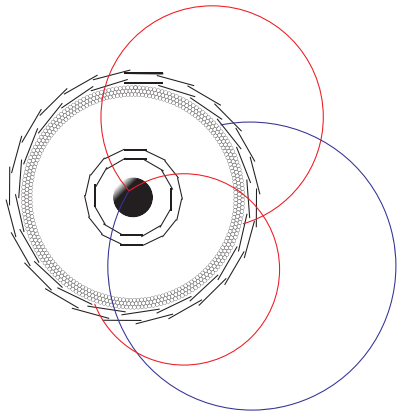

Figure 3.7: Schematic of the detector geometry looking along the beam axis[1]

layer is on the inside covered with a layer of scintillating fibers that allow precise time measurements (down to several hundred picoseconds [1]). The scintillating fibers will be placed at approximately 6 cm radius.

In order to allow high precision momentum measurements, the entire experiment will take place inside a large solenoid magnet, generating a constant magnetic field of 1 T. In the detector region, the field is aligned with the beam axis, causing decay particles to curl around the beam axis on helix-shaped tracks. These tracks are reconstructed using the information from the four silicon pixel detector layers. The particle momentum is then determined from the reconstructed tracks.

To increase the precision of the momentum measurement, recurl stations are added on the end of the central tracking station. The recurl stations contain a double layer of silicon pixel detectors on the outside (this double layer is the same as the layers 3 and 4 of the central tracking station), and a scintillating tile detector on the inside, which gives additional time information, with a time resolution of or below 100 ps [10].

In a first run (Phase I A) the experiment is planned to run with just the central tracking station in place, lacking the scintillating fiber hodoscope. This run is intended for early commissioning and physics. In Phase I B, the full central tracker will be used along with the recurl stations (this is depicted in Fig. 3.6), for physics runs with increased time and momentum resolution and tile detector commissioning. The expected sensitivity in Phase I B is of the order of 10^{-14} [1]. The full sensitivity of the experiment of 10^{-16} is planned to be reached in Phase II, when two additional recurl stations will be added, one upstream and one downstream of the Phase I B Setup sketched in Fig. 3.6.

3.3.2 Multiple Coulomb Scattering

A charged lepton traversing matter is subject to many small scattering events. These scattering events are due to coulomb interaction with the nuclei of the atoms making up the matter. This phenomenon is called multiple coulomb scattering. The cumulative effect of multiple coulomb scattering can be described by the quantities shown in Fig. 3.8. The

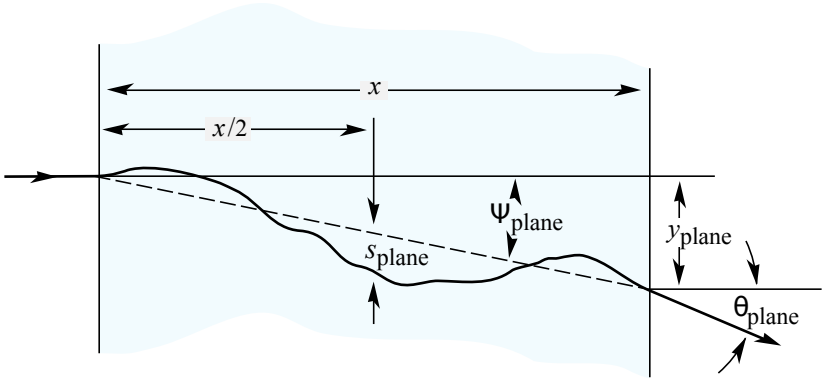

Figure 3.8: Quantities used to describe multiple coulomb scattering [7]

distribution of angular deflections θ_{plane} can be approximated as Gaussian, with an rms width given by: [7]

$$\theta_0 = \frac{13.6\text{MeV}}{\beta cp} z \sqrt{\frac{x}{X_0}} \left[1 + 0.038 \ln\left(\frac{x}{X_0}\right)\right] \tag{3.2}$$

where βc , p, and z denote velocity, momentum and charge number of the particle, and X_0 the radiation length of the material.

Since the Mu3e experiment depends on determining the particle tracks to measure particle momentum and uses energy cuts to suppress the internal conversion background, θ_0 has to be kept minimal whenever a particle passes through matter in the active detector region. This is especially important since the decay particles will be low-momentum (below 53 MeV). Thus, any material in the active region has to be chosen and placed such that $\frac{x}{X_0}$ is kept minimal.

3.3.3 The Pixel Detector

The silicon pixel tracker of the Mu3e experiment will consist of High-Voltage Monolithic Active Pixel Sensors (HV-MAPS). These are silicon semiconductor detectors, which have part of the readout electronics already on the chip (Fig. 3.9). An ordinary MAPS chip would collect the ionization charges produced by a passing particle via diffusion. A HV-

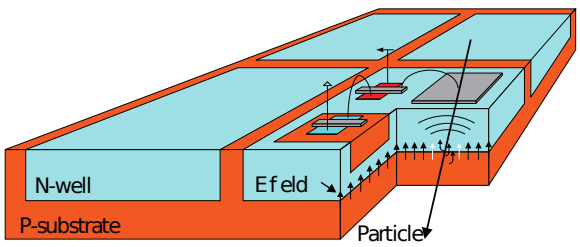

Figure 3.9: HV-MAPS working principle [8]

Component	Thickness[μm]	$\frac{x}{X_0}$
kapton support frame	25	0.018
kapton flex-print	25	0.018
aluminum traces	12.5	0.008
HV-MAPS	50	0.053
Adhesive	10	0.003
full detector layer	125	0.100

Table 3.1: Pixel layer radiation length by components [1]

MAPS chip, on the other hand, collects charges mainly via drift. The drift is caused by applying a high ($\approx$ 90 V) bias voltage. This allows a time resolution of about 16 ns [14].

One advantage of using HV-MAPS technology in the tracking detector is that because the active chip area itself already carries the readout electronics, no additional readout chips are needed, which reduces the amount of material in the detector. Another advantage is that HV-MAPS can be thinned down to 50 μm, further reducing the material budget. Together with 37 μm thin kapton-aluminum flex-prints used to supply power to the chips and read out data, and the kapton support structure with a thickness of 35 μm, the resulting thickness of one tracker layer will be only $\frac{x}{X_0} \approx 0.1\%$ (Table 3.1 shows a more detailed listing of the individual contributions).

3.3.4 The Time of Flight Detector

One of the requirements of the Mu3e detector is a good timing resolution, which is needed to suppress accidental background. A good time resolution also helps to prevent pileup, which would otherwise be a problem at high muon rates (Fig. 3.10).

The Mu3e time of flight detector will consist of two parts: A scintillating fiber tracker in the central tracking station, and a scintillating tile detector in the recurl stations (Fig. 3.6).

The scintillating fiber tracker is located insides the central tracking station, below the third pixel layer at a radius of about 6 cm. Since it is located in the active detector region, it is designed to add as little material as possible while keeping an acceptable time resolution. The planned time resolution of the scintillating fiber tracker is < 1 ns. The scintillating fiber tracker consists of ribbons of three to four layers of scintillating fibers. The fibers have a diameter of 250 μm, and are bundled into ribbons that are 1.6 cm wide and 36 cm long. At both ends of the fibers, Silicon Photo Multipliers (SiPM) are placed to detect the produced photons. SiPMs combine high counting rates, high gain, and compact dimensions.[1]

The scintillating tile detector (Fig. 3.12) is the second part of the time of flight detector. The scintillating tiles are placed within the recurl stations, underneath the third pixel layer. Because decay particles will pass this detector component last, it can be optimized for time resolution only, with no regard for the material budget. The tiles making up the tile

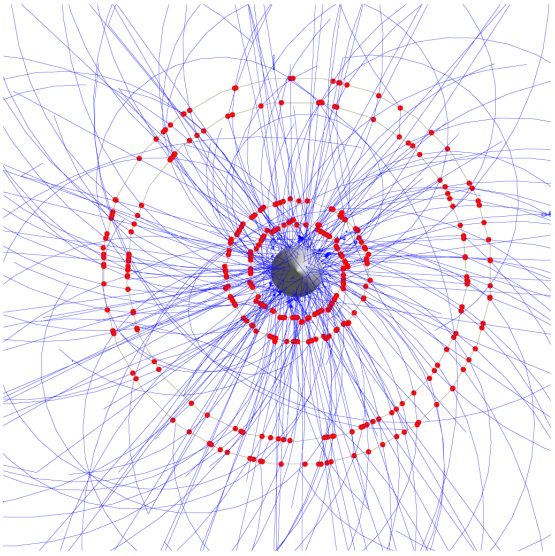

Figure 3.10: Simulated events during one 50 ns read-out frame at a muon rate of $2 \cdot 10^9\,\mathrm{s}^{-1}$ [1]

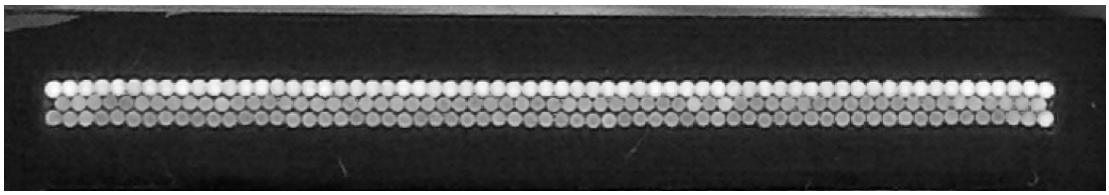

Figure 3.11: Transverse cut through a scintillating fiber ribbon [9]

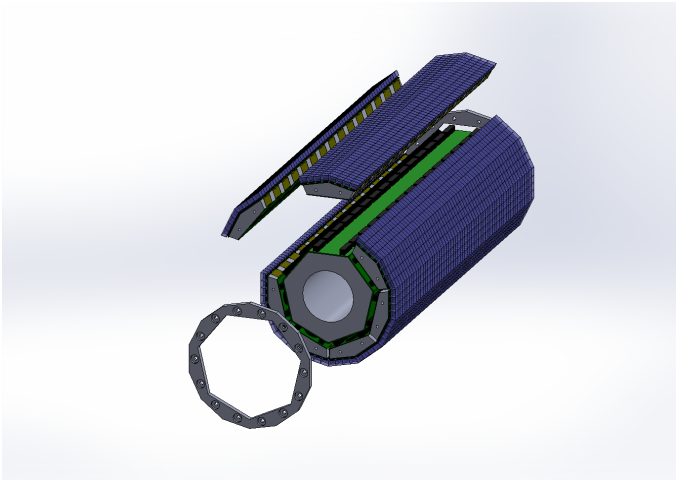

Figure 3.12: Exploded drawing of a full tile detector station [10]

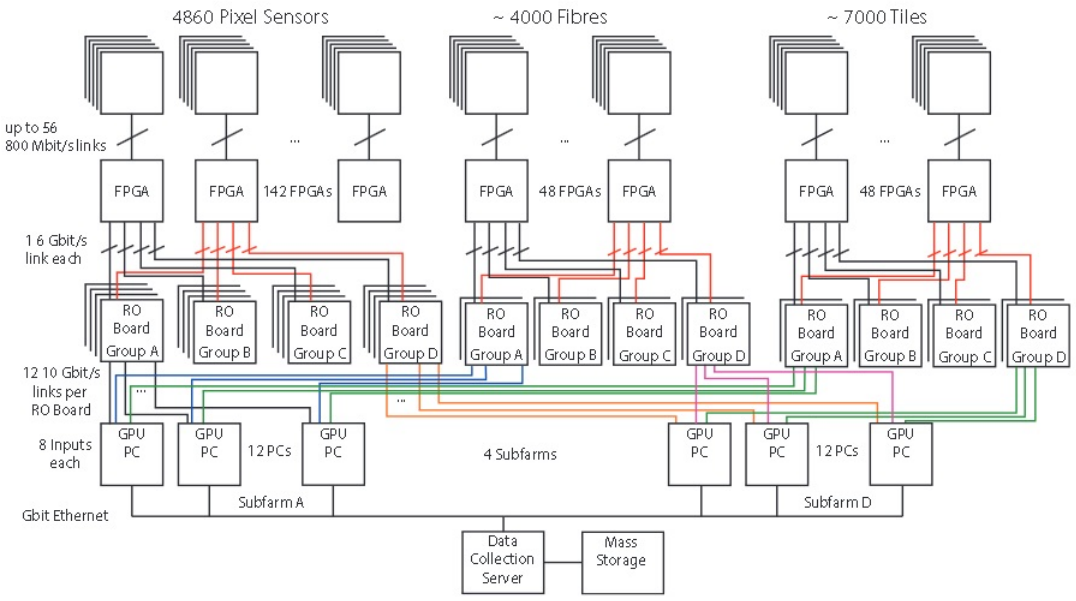

Figure 3.13: Mu3e readout scheme [1]

detector will be about $1\,\mathrm{cm}^3$ large. They photons they emit will be measured with SiPMs. The aim is to achieve a time resolution below 100 ps, and in testbeam measurements of the scintillating tile prototype, time resoltions of up to 56 ps have been achieved.[10]

3.3.5 Data Acquisition and Readout

The intended read out scheme of the Mu3e experiment is depicted in Fig. 3.13. The various detectors are continuously sending data at a rate of about $1\frac{\mathrm{Tbit}}{\mathrm{s}}$. The data coming from the detectors is first collected and buffered at the front end Field-Programmable Gate Arrays (FPGAs), which are located inside the recurl stations (underneath the scintillating tile detector). The information is then sent on to the read out boards, which select complete sets of event information from the entire detector and send these sets on to the filter farm PCs. The PCs perform online track reconstruction using commercially available Graphics Processing Units (GPUs) and use the reconstructed tracks to filter for potentially interesting events. The selected events are then aggregated in the data collection server, which will write them to mass storage at a rate of about $50\,\frac{\mathrm{MByte}}{\mathrm{s}}$ [1].

3.3.6 Mechanics

The design of the mechanical structure that supports the pixel detectors is dominated by the necessity of a low material budget, to minimize multiple scattering. Apart from this, high acceptance and ease of assembly and repair are also design goals. A drawing of the planned support structure of the central tracking station is shown in Fig. 3.14 .

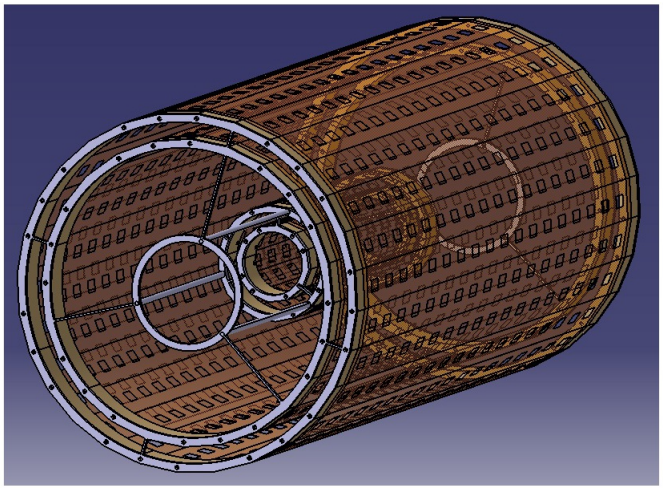

Figure 3.14: Drawing of the kapton support frame and the endrings

Figure 3.15: Mechanical prototype of the inner double layer

Figure 3.16: Mechanical prototype of an inner layer module

Figure 3.17: Mechanical prototype of an outer layer module

The pixel sensors are planned to be glued to 35 μm thick kapton-aluminum flex-prints. The flex-prints are further stabilized by prism-shaped kapton folds underneath the flex-prints. The folds add material, but the tremendous gain in stability outweighs that downside.

The kapton frame will be mounted on the beampipe using aluminum endrings (3.14). These endrings will also serve as the distribution system of the local helium cooling flow, which will be discussed in more detail in the next section.

The silicon sensors will have a dead area of about 0.5 mm on one side. To avoid acceptance losses, the sensors are placed on the support frame with an overlap of roughly 1 mm (Fig. 3.7).

To make the assembly process easier, the tracker layers will be divided into modules.

The inner double layer (Fig. 3.15) will be divided into two half shells per layer. The half shells will have an active length of 12 cm. Layer 1 will have eight sides with silicon detector strips, layer 2 will have ten.

The two outer layers will have 24 (layer 3) and 28 (layer 4) sides. Their active length will be 36 cm. Layer 3 will consist of six modules, and layer 4 of ten.

Mechanical prototypes were constructed using kapton or kapton-aluminum strips instead of flex-prints, and $6\times2\,\mathrm{cm}^2$ large and $50\,\mu\mathrm{m}$ thin glass plates instead of silicon detector chips (Figs. 3.15, 3.16, and 3.17). The glass plates were used because their flexibility is similar to that of the silicon detectors.

3.3.7 Cooling

The silicon detectors have an expected power output of roughly $250\,\frac{\mathrm{mW}}{\mathrm{cm}^2}$ [14]. Together with the other detector electronics, the total power that is lost thermally is 4000 W [11]. Because the HV-MAPS silicon pixel detector chips are designed to operate at a temperature below 70 °C [15], that power needs to be cooled away.

The planned cooling system of the Mu3e Detector has two components: beampipe cooling with water or a water based liquid coolant, and cooling with gaseous helium (Fig. 3.18). The liquid cooling in the beampipe will also be used to cool part of the readout electronics, which will be placed on the beampipe. Both the helium gas and the coolant liquid will be at a temperature slightly above[1] 0 °C.

Helium is used as coolant in the active detector region because it has a low atomic number[2] and is an effective coolant.

The helium cooling system will have three parts: a global helium flow encompassing the entire length of the detector, a helium gap flow in the gaps between layers 3 and 4, and a local helium flow in the folds underneath the silicon detector chips (Figs. 3.18 and 3.19). The global helium flow is planned to have a flow velocity of about $4\,\frac{\mathrm{m}}{\mathrm{s}}$, as is the gap flow velocity. The speed of the local helium flow is set at roughly $20\,\frac{\mathrm{m}}{\mathrm{s}}$ [11, 12].

The local helium flow is used because it increases the cooling power, decreases the temperature gradient along the length of the detector, and allows cooling parts of the

[1] to avoid freezing water

[2] the relative radiation length of a 1 m layer of helium is $\frac{x}{X_0} \approx 0.019\%$

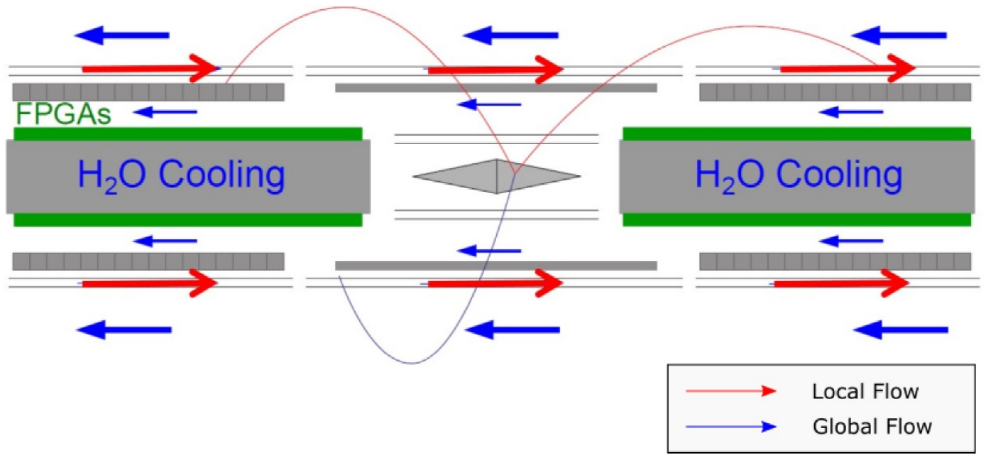

Figure 3.18: Schematic of the Mu3e cooling System [11]

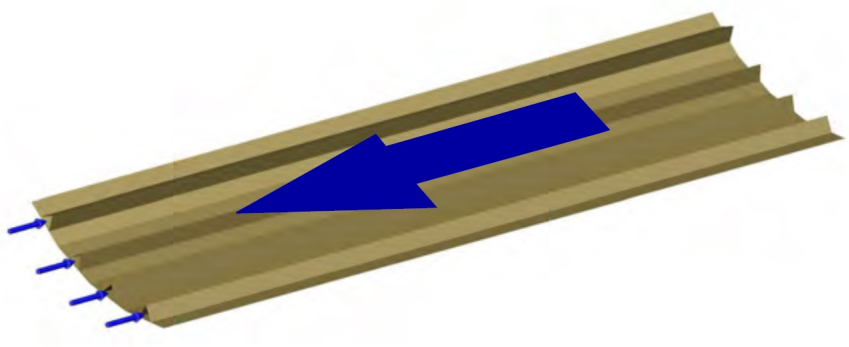

Figure 3.19: Geometry of local and global flow. Local flow flows through the V-shaped folds of the module, global flow flows outside the folds in the opposite direction.

detector that are not reached by the global helium flow.

The reasoning behind the gap flow is similar. The gap between layer 3 and 4 is not reached by the global helium flow, because the readout electronics between the different detector stations are in the way. Thus layer 3 is not sufficiently cooled. The dedicated gap flow out of the distribution system in the end-ring solves this problem [11].

Chapter 4

Michelson Interferometer

4.1 Basics

A Michelson Interferometer was used for three major measurements done in the context of this thesis: measurements of flow induced vibration, of the frequency response of the detector module prototypes, and of the module deformation when being subject to flow. The Michelson Interferometer was used because this minimizes the influence of the measurement on the observed module. Since the wavelength of the light source is known, no additional calibration of the measurement is necessary. Beyond being intrinsically calibrated, the absolute measurement of the displacement amplitude of the module vibration with a Michelson Interferometer is very precise. The uncertainty is in the order of a fraction of wavelength of the light used. For optical wavelengths, this is just a few hundred nanometers. This is two orders of magnitude below the range of 50 μm[1] at which module movement might endanger detector precision [12].

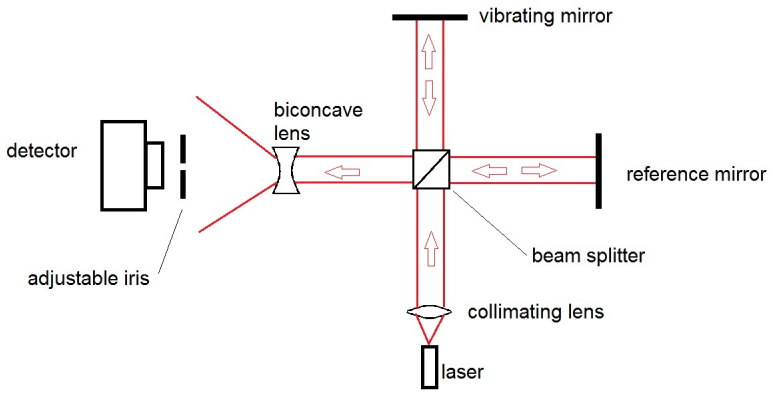

Figure 4.1: Principle of operation of the Michelson Interferometer

The principle of the Michelson Interferometer is shown in Fig. 4.1. The laser diode

[1]The thickness of one detector chip

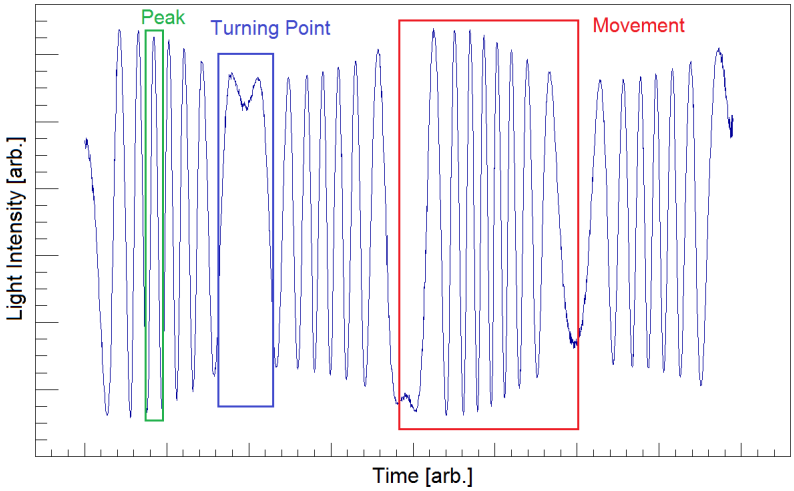

Figure 4.2: An exemplary plot of an interferogram

emits coherent[2] light with a highly monochromatic spectrum. The coherent light is then collimated by the biconvex lens. Moving the lens forward or backward leads to either a divergent beam, or a focused one.

The non-polarizing cubic beam splitter in the center of the setup then diverts half of the incoming intensity towards the reference mirror, the other half towards the vibrating mirror. The light that is reflected off both mirrors is then again joined in the beam splitter[3] and projected towards the biconcave lens.

The biconcave lens turns the collimated beam that exits the beam splitter into a divergent beam. If the beam is already slightly divergent, the lens will widen that divergence. The advantage of a divergent beam is that it leads to a wider interference pattern, which in turn makes it easier to pick out a specific fringe with the adjustable aperture. The light selected by the adjustable aperture then passes into the photo-detector. The photo-detector converts the intensity of the incoming light into a voltage which is measured and recorded using an oscilloscope.

Thus this setup allows to determine the intensity integrated over an area determined by the aperture iris in the interference pattern and its time evolution. This information of intensity over time is also called an interferogram (Fig. 4.2).

The interferogram contains information about the vibrating mirror's movement. This is because the beams reflected off the two mirrors interfere after they are again joined in the beam splitter. The phase difference of the two beams is due to the different optical

[2] in time

[3] To be precise, only half of the reflected light is exiting the beam splitter in the direction of the detector. The other half is projected back onto the laser, not shown in Fig. 4.1). Both exiting beams are composed of a superposition of light reflected off each of the mirrors, as the beam splitter "joins" the beams by splitting them.

paths they have covered. Because the light has to cover the distance from the beam splitter to the mirror twice, a displacement of the vibrating mirror of x induces a phase difference of $\frac{x}{4\pi\lambda}$.

Because one peak (Fig. 4.2) in the interferogram corresponds to a phase change of 2π, it is interpreted as a displacement of $\frac{\lambda}{2}$ of the vibrating mirror. In principle any other feature of the sinusoid, like minima, or zero crossings, which repeats with a fixed phase period could be used instead. After all, we are only interested in the change in phase.

Such peaks will show up for as long as the mirror keeps moving, when it stops, the phase change also stops, and the resulting pattern in the interferogram will look a lot less regular. Such a pattern is called a "turning point[4]" in this thesis (Fig. 4.2). The irregularity is due to small vibrations of the module which are much smaller than $\frac{\lambda}{2}$. Thus they only show up when larger movements have momentarily stopped.

Turning points are crucial to the interpretation of the data, because they mark the points where one starts and stops counting the peaks. The pattern of peaks inbetween two turning points is interpreted as a movement (Fig. 4.2). The movements length is $N\frac{\lambda}{2}$, where N is the number of peaks in the movement (in the example movement in Fig. 4.2, one would have $N = 8$). The precision of this measurement of the modules displacement is $\frac{\lambda}{2}$.

4.2 Limitations and Scales

Using a Michelson interferometer for measuring vibration amplitudes is useful only in certain ranges of amplitude and frequency. This is not much of a limitation for a mirror moving with a single mode of oscillation, but in the case of more complex movement, it can become problematic, as we will see later in this section.

Considering the scale of the movement, there is no principal upper limit to the number of fringes one can count. Consequently the only upper limit is the coherence length of the light source used. For short movements, counting peaks is only possible for movement lengths larger than $\frac{\lambda}{2}$.

Smaller movements can still be measured with the same setup. To do so, one measures the intensity at the end points of the small movement. Then the phase difference can be calculated, using a model for the phase dependency of the intensity such as [16]:

$$I(t) = I_0 \left[1 + V \sin\left(\Phi(t)\right)\right] = I_0 \left[1 + V \sin\left(\Phi_0 + \frac{4\pi}{\lambda} x(t)\right)\right] \tag{4.1}$$

Because the point of the measurements was mainly to either see in what conditions large movements occured (frequency response) or to confirm the absence of such large movements (flow induced vibration), this approach was never used here.

Movements smaller than $\frac{\lambda}{2}$ can still become a problem however, if the intensity modulation is too large. Intensity modulation means that the parameters V and I_0 in 4.1 are

[4]because one thinks of the movement reverting direction; however, from just one interferogram, the direction of the movement cannot be deduced

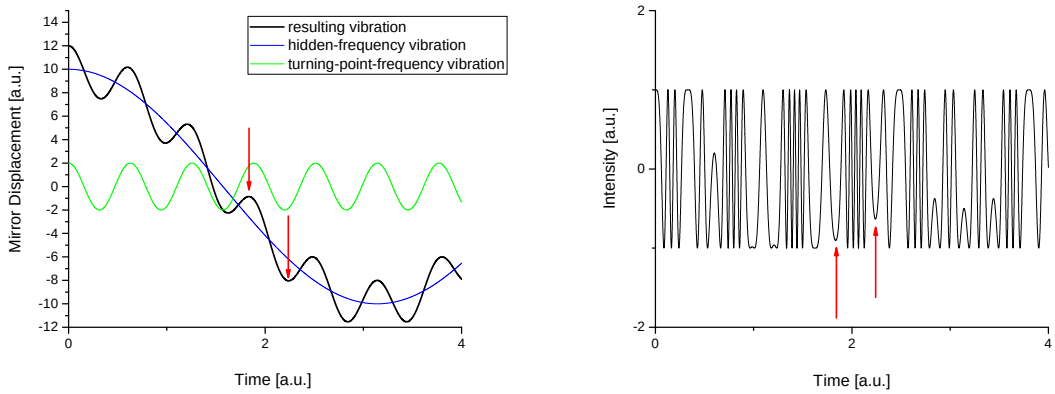

Figure 4.3: Mirror vibration in a superposition of modes with a large hidden amplitude. The left plot shows the actual movement of the mirror, the right plot shows the resulting interferogram. The low frequency contribution (blue curve) is hidden. This is because the turning points (red arrows) of the high frequency contribution determine the turning points in the interferogram.

time dependent, for example $V = V_0 \sin(\phi_V + \omega t)$, or dependent on the phase $\Phi(t)$. Such a modulation is usually present to some degree, it is also clearly visible in Fig. 4.2. It can be minimized by carefully adjusting the optical components of the setup, and usually it is small enough not to pose a problem. If it does not, however, then the problem is to distinguish between intensity variations that are smaller than $\frac{\lambda}{2}$, and modulate the interferogram by modulating $x(t)$, and full-phase peaks in a region where V is much smaller than its maximum value. This is an important problem, because variations in $x(t)$ smaller than $\frac{\lambda}{2}$ can safely be disregarded, while a movement of several peaks length could be large enough to threaten detector precision[5], and consequently needs to be considered. Since the interferogram data does not allow to distinguish the two cases, careful adjustment of the optical system is the only way to avoid this problem. To be on the safe side, when in doubt, a large movement was assumed.

Another limitation of this method is that the direction of the vibrating mirror's movement can not be determined. This makes it necessary to make assumptions about the way the mirror moves when interpreting the data. In this thesis it is always assumed that a turning point in the interferogram is in fact the result of the mirror changing direction.

Hidden Modes

A further problem are superposed modes of vibration. For example, one can consider a superposition of vibrational modes where a large amplitude, low frequency vibration and a small amplitude, high frequency vibration are superposed (Fig. 4.3). If the amplitude of the high frequency vibration is not smaller than $\frac{\lambda}{2}$, one will see only the turning points of

[5]With $\lambda = 635\,\text{nm}$, dangerous movements are several hundred peaks long

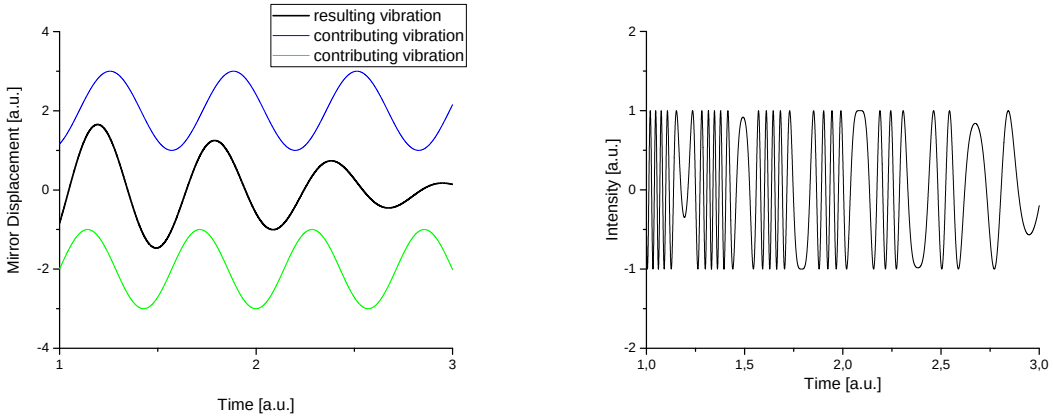

Figure 4.4: Example of superposed vibration modes without large hidden amplitudes

the high frequency vibration in the interferogram (Fig. 4.3). This means that one will end up determining a value for the largest observed vibration amplitude that is too small. In the example of Fig. 4.3 the observed amplitude is more than a factor of 2 to small. Since we want to prove the absence of large movement amplitudes this is a serious problem.

There is a way to mitigate this problem, which will be explained below. Modes contribute significantly to the interferogram if their amplitudes are larger than $\frac{\lambda}{2}$. By interferometry, one will always see turning points at twice[6] the frequency of that contributing mode which has the highest frequency. In order to find vibration amplitudes at lower frequencies, one can add up a large number of consecutive movement lengths, alternating the sign of the addends:

$$A(n(t)) = \sum_{i=0}^{n(t)} (-1)^i a_i \tag{4.2}$$

where $a_{i(t)}$ is the amplitude of the i^{th} movement, which stopped at time t. The result of this alternating sum is the mirror displacement at the different turning points as a function of time $A(t)$. From this one can infer the largest overall distance that the mirror covered.

The scaling behavior of the alternating sum uncertainty can be understood by considering a superposition of two modes of vibration. One of the modes is assumed to have a frequency f_h lower than that of the other mode, f_{tp}. The amplitude $n_h \frac{\lambda}{2}$ of the hidden mode is assumed to be larger than the amplitude $n_{tp} \frac{\lambda}{2}$, because this is the interesting case (Fig. 4.3).

The alternating sum over an interval at least as long as one hidden movement will need $\left\lfloor \frac{1/(2f_h)}{1/(2f_{tp})} \right\rfloor = \left\lfloor \frac{f_{tp}}{f_h} \right\rfloor$ addends.

Assuming there are no counting errors, the absolute uncertainty of each indivdual addend a_i will be $\delta a_i = \frac{\lambda}{2\sqrt{12}}$.

[6] A full period contains two turning points

With that one can estimate the minimal relative error of the hidden mode amplitude as determined by the alternating sum. Using (4.2) and Gaussian error propagation one gets:

$$\frac{\delta A}{A} = \frac{\sqrt{\sum_{i=0}^{\lfloor f_{tp}/f_h \rfloor} \delta a_i^2}}{\sum_{i=0}^{\lfloor f_{tp}/f_h \rfloor} (-1)^i a_i} \approx \frac{\sqrt{\sum_{i=0}^{\lfloor f_{tp}/f_h \rfloor} \left(\frac{\lambda}{2\sqrt{12}}\right)^2}}{n_h \frac{\lambda}{2}} = \frac{\sqrt{\left\lfloor \frac{f_{tp}}{f_h} \right\rfloor}}{\sqrt{12} n_h} \tag{4.3}$$

This is a promising result, because in case of a large hidden mode, n_h is large. Thus the relative error should be small. However, this result still depends on the frequency ratio of the superposed modes, and there is no obvious reason why it should not be large.

If we further assume that the velocity amplitudes $fn\frac{\lambda}{2}$ of the modes are similar to one another, we can use that $\left\lfloor \frac{f_{tp}}{f_h} \right\rfloor \approx \frac{n_h}{n_{tp}}$ to get:

$$\frac{\delta A}{A} \approx \frac{1}{\sqrt{12\, n_h n_{tp}}} \tag{4.4}$$

for the relative error of the alternating sum.

This is encouraging, because the relative error scales with $1/\sqrt{n_h}$. If a hidden amplitude is large enough to threaten detector precision, it will have n_h of the order of $\frac{50\,\mu\text{m}}{635\,\text{nm}} \approx 80$ [7]. The precise relative error will of course depend on the velocity scaling and the amplitude of the high-frequency mode, but it will be of the order of 10%. This is sufficient to confidently identify such a movement amplitude. Of course, the alternating sum is very imprecise for low amplitude hidden modes, but these are not relevant to the vertex resolution in any case. Relevant hidden modes are those $50\,\mu$m large or larger, and these can be found reliably.

4.3 Setup

The Michelson interferometer is shown in Fig. 4.5. The laser that was used is a 4.5 mW CW laser that emits monochromatic light with 636.5 ± 0.5 nm wavelength. Based on the laser spectrum provided by the manufacturer, the width of the spectrum is of the order of $\Delta\lambda \approx 0.5$ nm. This corresponds to a coherence length of $\frac{\lambda^2}{\Delta\lambda} \approx 1$ mm.

The collimating lens is mounted in the laser casing, and its position can be adjusted by turning a screw on the casing, enabling adjustment of collimation or focus as needed. In order to comply with safety regulations, two grey filters were mounted in the casing behind the collimating lens, so that the laser beam exiting the casing has a power of less than 1 mW. An additional diode inside the lasers casing measured the emitted power and adjusted the voltage applied to the laser diode to ensure a constant power output. Since the laser is a diode laser, the beam has an elliptical intensity profile, with a long axis of 5 mm length and a short axis of 1.9 mm if the beam is collimated. The complete specifications of the laser used are given in appendix A.

[7] 160 and 320 if one counts in steps of $\frac{\lambda}{2}$ and $\frac{\lambda}{4}$, respectively

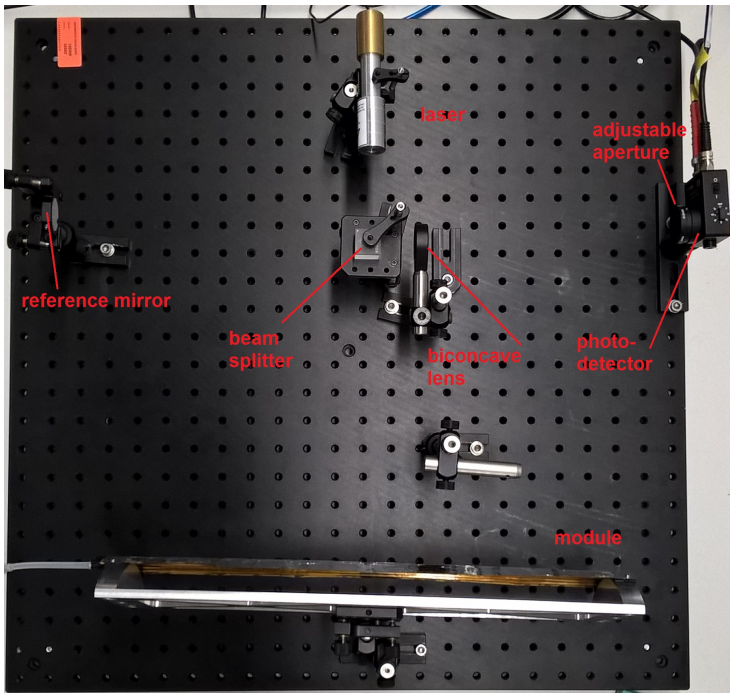

Figure 4.5: Michelson interferometer with the layer 4 module prototype

To measure the intensity of the light, a silicon photodiode detector with an active area of $13\,\mathrm{mm}^2$ and bandwidth of up to $10\,\mathrm{Mhz}$ which is sensitive to light of wavelengths between $350 - 1100\,\mathrm{nm}$ is used. Its amplification can be adjusted from $0\,\mathrm{dB}$ to $80\,\mathrm{dB}$ in steps of $10\,\mathrm{dB}$, but increasing amplification means decreasing bandwidth due to the internal electronics. Because of this, for all measurements amplification was chosen as high as necessary, but as low as possible.

All optical components with the exception of the mirror on the module were mounted on top of a $1\,\mathrm{m}^2$ breadboard. The breadboard rested on four flat cylindrical feet made from isopropane, which were meant to isolate it from vibrations of the environment. The module was positioned at the side of the breadboard. For all measurements, the distance between the reference mirror and the beam splitter was chosen roughly equal to that of the vibrating mirror from the beam splitter, in order to have the best coherence of the two beams and make sure that the images of the two mirrors overlapped as congruently as possible.

The reference mirror was mounted on a kinematic mount that allowed precise adjustment of its tilts in two directions. The laser was mounted such that it was tilted slightly below the horizontal plane, to avoid reflection of the beams into the laser. This was done not to avoid damaging the laser because of the external resonator, but to avoid instabilities in the laser power due to the photodiode in the laser picking up intensity variations in the reflected beam due to interference, and trying to reduce them by adjusting the voltage applied to the laser diode.

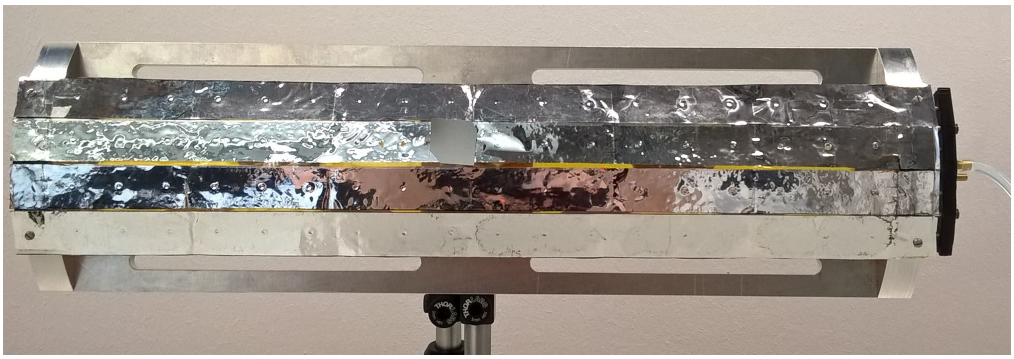

Figure 4.6: Layer 4 module prototype

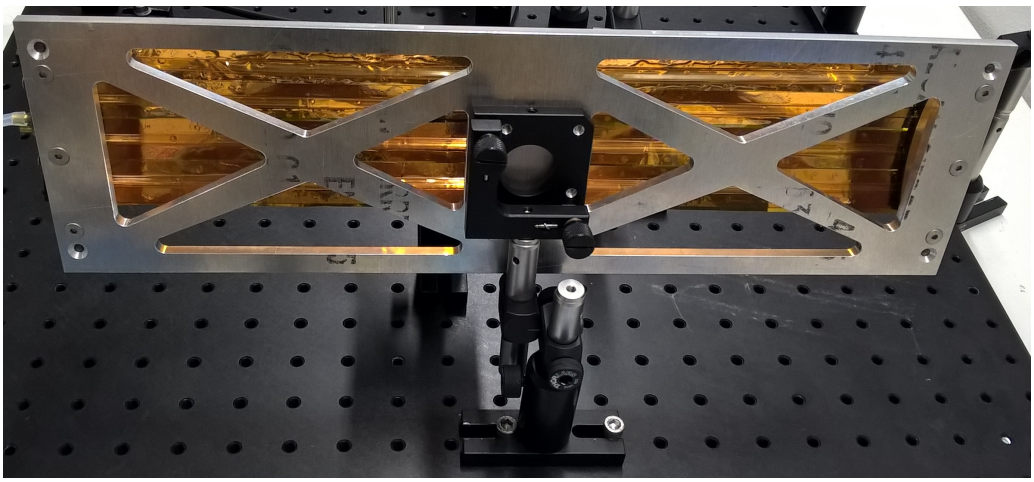

Figure 4.7: Mounting of the layer 4 module prototype

4.4 Modules

The measurements were done with module prototypes built from strips of kapton and aluminum, with 50 μm thick glass plates glued on to it (to simulate the behavior of silicon chips). Two different models were used: one of an outdated version of the outer layer (layer 4) detector modules and an up to date model of a layer 3 detector module.

4.4.1 Layer 4 Module Prototype

The module was screwed onto a CNC-milled aluminum mounting using the same screws and slots that would be used in the actual mounting of the module. The mounting was fixed on a kinematic mirror mount that allowed tilting the Module with high precision (Fig.4.7). The mirror mount could either be mounted on the breadboard, or on a separate base that could be placed besides the breadboard.

The vibrating mirror was glued directly onto the module with instant glue. For the mirror a 0.3 mm thick and 2 mm $\times$ 2 mm large glass piece was used, onto which a mirroring

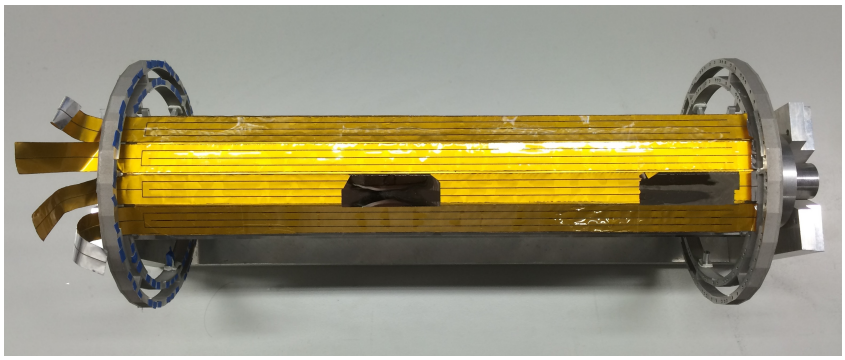

Figure 4.8: Layer 3 module prototype with endrings. The beam pipe prototype is obstructed by the module.

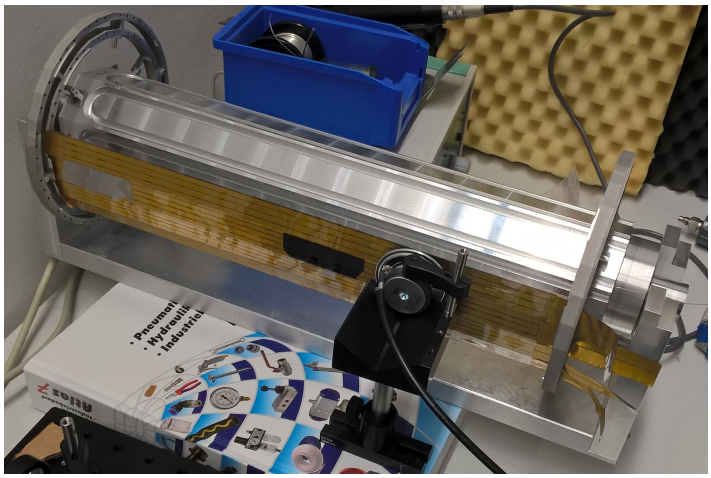

Figure 4.9: Layer 3 module prototype with beam pipe prototype. The speaker in front of the module was used for frequency response measurements (chapter 5) and is not part of the module mounting.

surface of gold-palladium alloy had been deposited evenly by sputtering.

4.4.2 Layer 3 Module Prototype

The Layer 3 module prototype was screwed onto an aluminum model of the central tracking station endrings (Fig. 4.8). The endrings were connected by a steel model of the beam pipe (Fig. 4.9). The endrings contained a gas distribution system that allowed attaching tubes to inject gas into the distribution system from outside, which is then fed into the attached modules. The beam pipe model with the endrings and layer three module attached was supported by a steel contraption that allowed it to be turned around its long axis.

There were two mirror surfaces on the Layer 3 Module Prototype, one located near the center of the module, the other near its end (Fig. 4.8). Both were placed in the 3rd Row (out of four) of glass plates on the module. Both mirrors were basically the same

$2\,\text{cm} \times 2\,\text{cm} \times 50\,\mu\text{m}$ glass plates used for the construction of all module prototypes, but they were coated with a thin Au-Pd alloy by sputtering before they were built into the module.

4.5 Background

The module prototypes are very light and thin. Thus one can expect that even if no vibrations are excited by a speaker or by local flow, the modules will move. This background movement can be caused by low frequency vibrations of the building, nearby traffic and construction work, opening and closing of doors, loud sounds, air movement etc. It can be observed with the Michelson interferometer. An exemplary interferogram of the background movement of the layer 4 module prototype is given in Fig. 4.10. By comparing it with an interferogram of flow induced vibration of the same module (Fig. 4.11), one can see that the background movements are significantly slower and less large than the flow induced vibration variant. This is fortunate, because the slower background movement is automatically filtered from the flow induced vibration interferometry data, due the effect discussed in section 4.2(Fig. 4.3 in particular). The same holds for the background movement of layer 3 (Figs. 4.12 and 4.13).

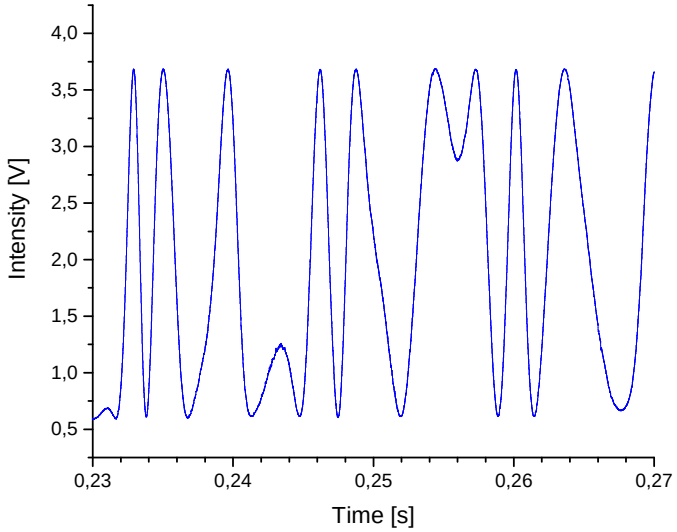

Figure 4.10: Exemplary background interferogram of the layer 4 module prototype. The movement speed and the distances covered are significantly lower than in the case of flow induced vibration (Fig. 4.11).

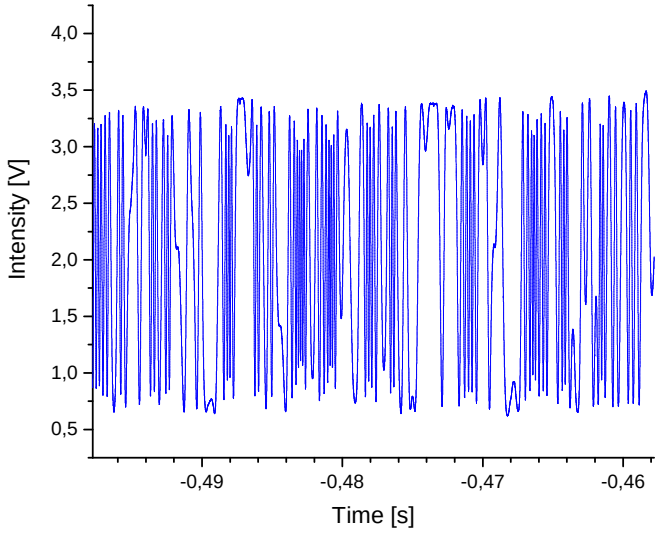

Figure 4.11: Exemplary interferogram of flow induced vibration in layer 4.The movement speed and the distances covered are significantly higher than in the case of background movement (Fig. 4.10).

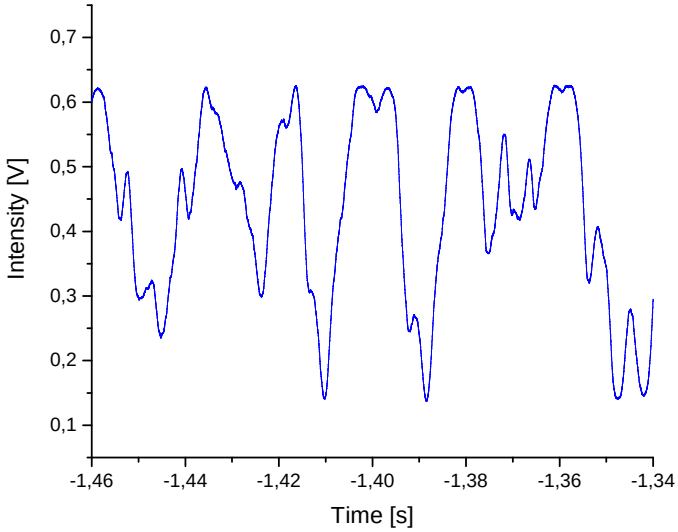

Figure 4.12: Exemplary interferogram of the layer 3 background movement.The movement speed and the distances covered are significantly lower than in the case of flow induced vibration (Fig. 4.13).

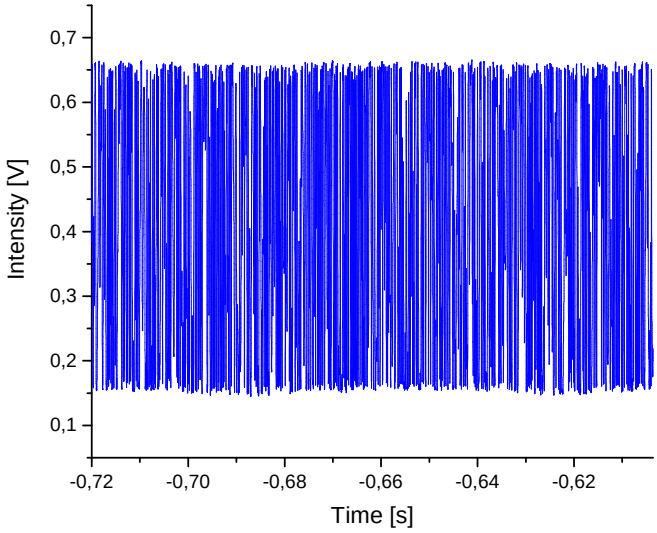

Figure 4.13: Exemplary interferogram of flow induced vibration of layer 3. The movement speed and the distances covered are significantly higher than in the case of background movement (Fig. 4.12).

Chapter 5

Frequency Response

The Mu3e detector is planned to be extremely light, in order to reduce multiple Coulomb scattering. However, the thin, low weight detector structure could also lead to strong vibrations if the gaseous helium cooling flow excites the detector at a frequency close to a resonant frequency. This can be prevented by building the experiment such that these resonant frequencies are avoided. To do this it is necessary to know the relevant resonant frequencies beforehand. In order to get to know the resonant frequencies, the frequency response of the detector modules was investigated experimentally. In this chapter these measurements and their results are described.

5.1 Resonance Measurements

The module prototypes whose frequency response was measured were the layer 4 and layer 3 module prototypes. The modules' mechanical response was measured with the Michelson Interferometer, since it allows to keep the influence of the measurement procedure on the modules at a minimum.

To excite vibrations in the modules at specific frequencies, a small speaker was placed directly in front of the modules (but without touching them), near their center but to the side of the mirrors (Fig. 5.1). The speaker was connected to a waveform generator, which generated sine-shaped AC voltages with precisely controllable amplitude and frequency. The speaker was used because it allowed to drive the modules to oscillation with a moderate amount of force, small enough not to break the modules, and large enough to be observable with the Michelson Interferometer via counting interference maxima.

However, using the speaker to drive the modules to vibration in this manner means that there is the potential not just for finding the resonant frequencies of the detector modules, but also those of the speaker. To make sure that the speaker resonances are not mistakenly interpreted as resonances of the modules, the frequency response of the speaker was also measured. The frequency dependence of the impedance of the speaker was obtained by measuring the electric current through the speaker as an AC signal with a constant peak-to-peak amplitude of $U_{pp} = 10\,\mathrm{V}$ was applied. The frequency of the AC

Figure 5.1: Placement of the speaker

voltage was varied from 10 Hz to 1680 Hz by adjusting the waveform generator in steps of 10 Hz. For each frequency, the RMS current I_{RMS} through the speaker was measured using a multimeter. The impedance was then calculated according to

$$|Z| = \frac{U_{pp}}{\sqrt{2^3} I_{RMS}} \tag{5.1}$$

The error of the impedance values thus obtained was estimated based on the multimeter accuracy of $\delta I_{RMS} = 0.1\,\mathrm{mA}$ to be:

$$\delta|Z| = \frac{U_{pp}}{\sqrt{2^3} I_{RMS}^2} \delta I_{RMS} \tag{5.2}$$

using Gaussian error propagation.

Additionally, using two microphones, the acoustic frequency Response of the speaker was recorded. The microphones were differently responsive and the sound pressure of the speaker varied strongly with frequency. This meant that the microphone that allowed good measurements in one frequency range would saturate or be noise dominated in another. Thus, both microphones were across in different parts of the desired frequency range.

In order to access also very low frequencies, the gain of the internal amplification electronics of the microphones was varied over its full range.

To get a continuous result, in frequency ranges were the microphones or their settings were changed, overlapping frequency intervals were recorded. By taking the averages in the overlap regions, the relative scale of the measurements was determined, to account for different sensitivities of the microphones, and the different gain settings. The full frequency response was then merged together out of the separate datasets. Because of the factors used to align the data, the unit of the acoustic response is given as arbitrary.

By considering the frequency response of the speaker, one potential source of wrongly attributed module resonances is taken care of. Another such source of “fake” resonances

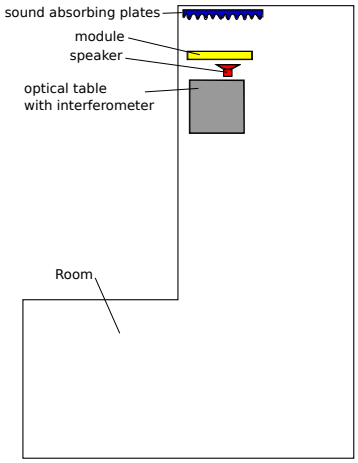

Figure 5.2: Position of speaker and sound absorbing plates in the room

are the walls of the room the measurement takes place in. If opposite walls happen to be at distances equal to integer multiples of the half-wavelength of the soundwave generated by the speaker, a standing sound wave could occur. Such a standing soundwave is a resonance of the room, and might show up in the frequency response data. With the speed of sound in dry air of roughly $322\,\frac{\mathrm{m}}{\mathrm{s}}$, the frequency range under consideration (tens of Hz to kHz) corresponds to wavelengths ranging from a couple meters down to a few centimeters. This is certainly the range of length scales relevant to the dimensions of the laboratory (if one keeps in mind that multiples of wavelengths should also be considered). Thus, sound absorbing plates were placed on the wall nearest to the setup (Fig. 5.2) to reduce the influence of the rooms resonances.

For each measured frequency on each of the two module prototypes, a several seconds long interferogram was recorded using an oscilloscope, and then saved as an ASCII file. From the file the information about the displacement amplitude of the modules vibration was then extracted by an algorithm developed by [17].

The algorithm used has a slight tendency to report too high movement amplitudes if the input data corresponds to movements with an amplitude of one wavelength or lower [17]. This is due to difficulties in identifying the ends of movements, meaning that a turning point (Fig. 4.2) is found by the program even though there is none, or failing to recognize an existing turning point.

To deal with this problem, after all the movements were identified and counted, a filter was applied. The duration of each movement was determined by the algorithm, and all movements whose inverse doubled[1] duration was larger than 120% or lower than 80% of the speaker frequency of the measurement in question, were discarded. This means that

[1]since one counts from turning point to turning point, a movement duration is not one period of oscillation, but half that.

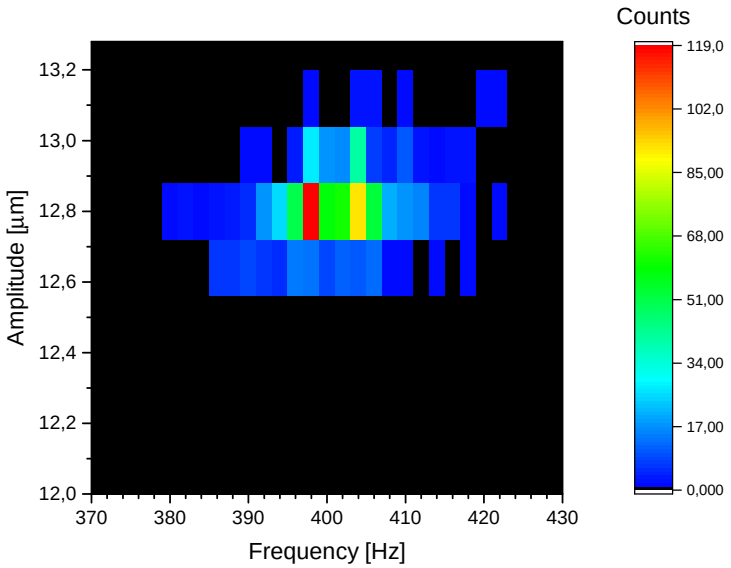

Figure 5.3: Amplitude-frequency histogram of the layer 4 module movement at a speaker frequency of 400 Hz

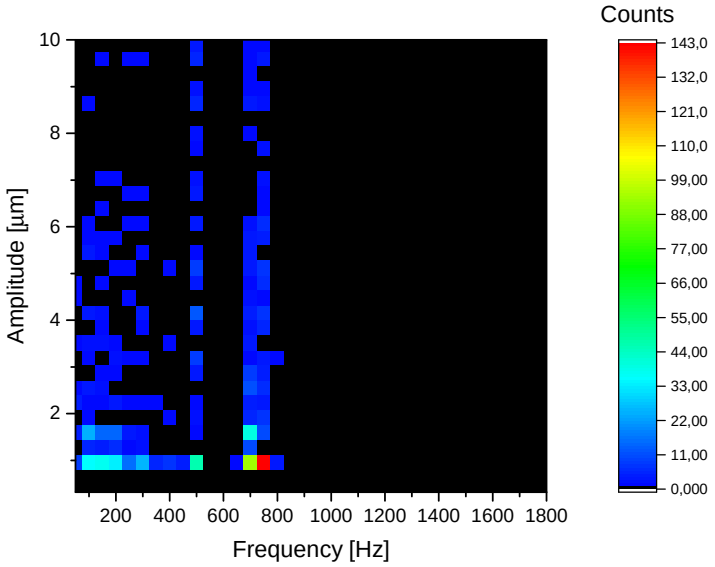

Figure 5.4: Amplitude-frequency histogram of the layer 4 module movement at a speaker frequency of 1400 Hz

obviously over or under-counted movements are filtered out, since they are shorter or longer in duration than the half-period of the driving speaker signal. An additional benefit is that physical movements of the module not excited by the speaker (e.g. background vibration, noise) are also cut away.

Exemplary histograms showing the amplitude-frequency distribution found by the algorithm are given in Figs. 5.3 and 5.4. One can see that the module responds moderately strongly to the speakers driving frequency of 400 Hz (Fig. 5.3). Moreover the width of the frequency distribution is far smaller than the ±20% band allowed by the frequency filter, so no potentially relevant contributions are cut away. On the other hand, at a driving frequency of 1400 Hz, the module does not respond at all (Fig. 5.4). This is an example of how the frequency filter helps in dealing with low amplitude, or no response data. While the algorithm does find movement, it is not related to the driving frequency, and does not pass the filter, so the algorithm correctly reports an absence of movement.

5.2 Results

5.2.1 Speaker Frequency Response

Impedance Measurement

Fig. 5.5 shows the impedance curve of the speaker. Three resonances can be distinguished. The first is the most prominent. The corresponding resonant frequency was determined

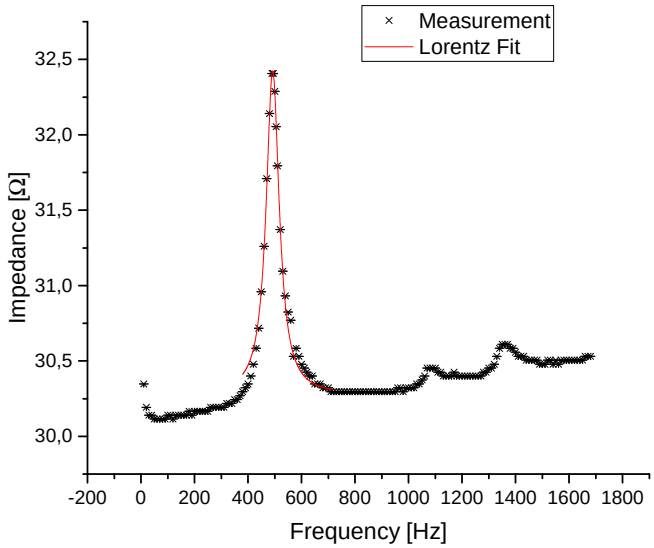

Figure 5.5: Frequency dependence of the speaker impedance

by fitting a Lorentz model to the impedance Z as a function of the frequency ν

$$Z(\nu) = Z_0 + \frac{2A}{\pi} \frac{\Gamma}{4\left(\nu - \nu_0 \tilde{\mathrm{A}}\mathrm{ij}\right)^2 + \Gamma^2} \tag{5.3}$$

where Z_0 is the baseline impedance, A is the peak area, Γ is the Full Width at Half Maximum (FWHM) of the peak, and ν_0 is the resonant frequency. According to the fit, the resonant frequency is $492.2 \pm 0.6\,\mathrm{Hz}$. The fitted data were weighted with the errors estimated according to 5.2. The fit has $\chi^2_{red.} = 0.0049$, indicating that the errors of the individual measurements were overestimated. There are two further peaks in the plot, however, they are not strong enough to give significant fit results. The two weak peaks are positioned at $1080 \pm 5\,\mathrm{Hz}$ and $1360 \pm 5\,\mathrm{Hz}$, respectively.

Acoustic Measurements

The results of the acoustic response measurement are given in Fig. 5.6. The final measurement of the module response was done in units of displacement, and microphones record sound pressure. So to get a more comparable result, the sound pressure recorded by the microphone was divided by the squared frequency the speaker was running at. Thus, the final acoustic speaker response data was in units of sound displacement.

The steep rise at the low frequency end in Fig. 5.6 is an artifact of this re-scaling. As the sound pressure data approaches zero due to low sensitivity, it cannot negate the effect of the $\frac{1}{\nu^2}$ re-scaling factor anymore. Thus the sound displacement amplitude increases, but not due to a physical response of the speaker-microphone system. This is also why the errors increase so rapidly in that region.

Two resonances are visible in the acoustic response (Fig. 5.6). They were fitted with the same Lorentz-Model used for the peak in the impedance response plot (egn. (5.3)). Fit 1 has $\chi^2_{red.} = 0.19$ and gives a resonant frequency of $507.0 \pm 0.8\,\mathrm{Hz}$, while Fit 2 has $\chi^2_{red.} = 0.015$ and a resonant frequency of $137 \pm 1\,\mathrm{Hz}$. The low $\chi^2_{red.}$ indicate overestimated errors, which is directly visible in Fig. 5.6, especially in the case of Peak 2.

The acoustic resonance at 507 Hz can be identified with the 492 Hz peak observed in the impedance measurement. The errors of the fit parameters suggest a significant deviation, but the lowered $\chi^2_{red.}$ due to overestimated data uncertainties mean that the fit parameter uncertainties are underestimated by the fit. Additionally, systematic effects could play a role as well. The acoustic and electric resonance behavior of the speaker are coupled, but not identical, since the physical systems are not identical. so there might be a shift of the resonance peak because mechanical damping has a stronger effect on the acoustic part, or because the coupling itself is frequency dependent. Beyond these effects of the speaker system, the different methods of measurement introduce further systematic effects. The microphones have unkonown frequency dependencies of their own, whereas the multimeter used for the impedance measurement should have a flat response by comparison.

The impedance peaks at 1080 Hz and 1360 Hz and the acoustic resonance at 137 Hz do not have corresponding features in the other respective plot. This is due to the low number

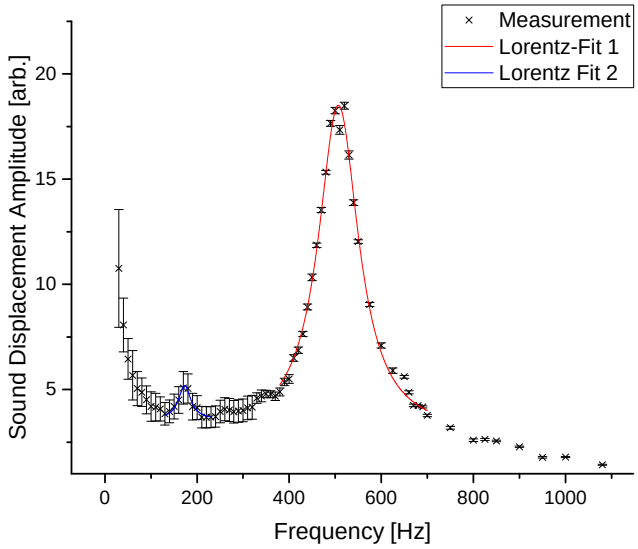

Figure 5.6: Acoustic response of the speaker

of samples in the case of the impedance peaks, so there might be acoustic resonances there too, but one would not see them due to lack of data. But there is plenty of data in the 137 Hz region (fig. 5.5), yet no resonance can be seen. This might mean that either the smaller acoustic resonance is due to the microphone resonating at that frequency, but it could just as well be canceled out by some filtering effect of the speaker electronics, thus making it invisible in the impedance plot. Since neither the layer 3 nor the layer 4 frequency response show any discernible peaks in the area around 137 Hz, it is considered to be irrelevant (Figs. 5.8 and 5.11).

5.2.2 Frequency Response of the Layer 4 Module Prototype

The frequency response of the layer 4 module prototype is depicted in Fig. 5.7. The module prototype responds over a wide range of frequencies, starting at 50 Hz and ending at about 1000 Hz. Four clusters of resonances may be distinguished in this frequency range. The first consists of two distinct resonances at 50 Hz and 56 Hz (Fig. 5.8). They are followed by another double-peak of resonances at 106 Hz and 117 Hz.

After that, there is a uniform plateau of moderate response ranging from 135 Hz to 215 Hz. This could be a superposition of a large number of smaller resonances, such as may be caused by individual parts of the module resonating. The wide frequency distribution suggests a wide range of sizes of these parts, so this could be due to broken glass plate parts on the module resonating. The slightly stronger maximum at the low frequency end might then be explained as the resonance of mostly intact glass plates.

The final resonance cluster is also the largest. It begins at 250 Hz and ends at about

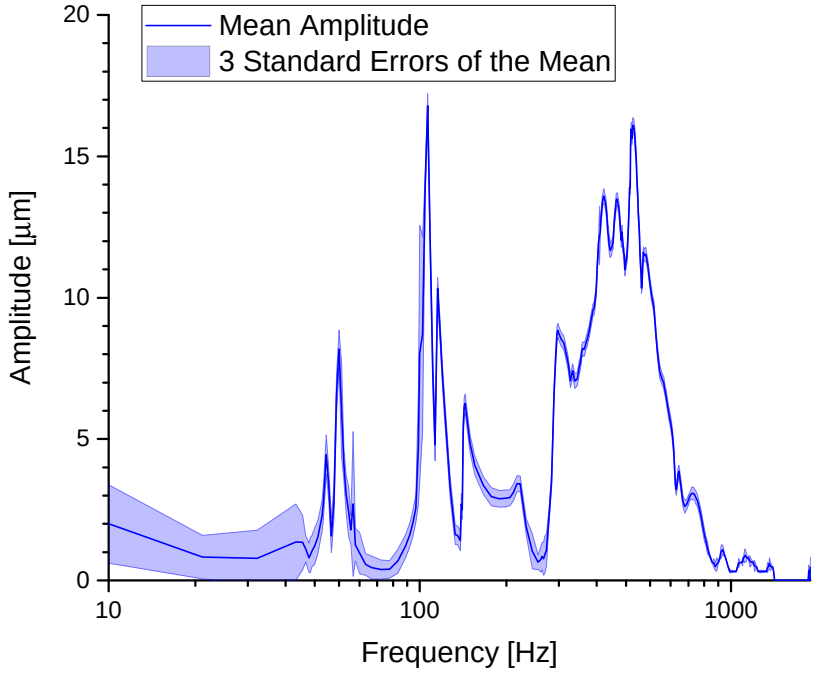

Figure 5.7: Entire frequency response of the layer 4 module prototype

800 Hz. There are small peaks beyond that, but they are an order of magnitude lower in amplitude. This cluster is again a superposition of resonances, however, there a re several peaks that can be distinguished here. Notably, there is strong peak at 492 Hz, which is likely due to the first speaker resonance (Fig. 5.6) at 492 Hz. The remaining resonances in the cluster do not, however, correspond to any speaker resonance, and must be inherent properties of the module.

Following the final large cluster, there are three small individual resonances at 950 Hz, 1150 Hz, and 1330 Hz, respectively. The 1150 Hz resonance is particularly broad, so it may be composed of several more narrow resonances. In that case, one of them could be due to the speaker resonance at 1080 Hz. The 1330 Hz peak is likely due to the speaker resonance at 1360 Hz.

At even higher frequencies, the modules response falls below $\frac{\lambda}{2} = 318\,\text{nm}$ in amplitude, meaning that it can no longer be measured using the method of counting peaks. An exemplary interferogram of this case is shown in Fig. 5.9. A scan of those frequencies up to several hundred kHz yielded no module responses larger than 318 nm over the entire scanned range.

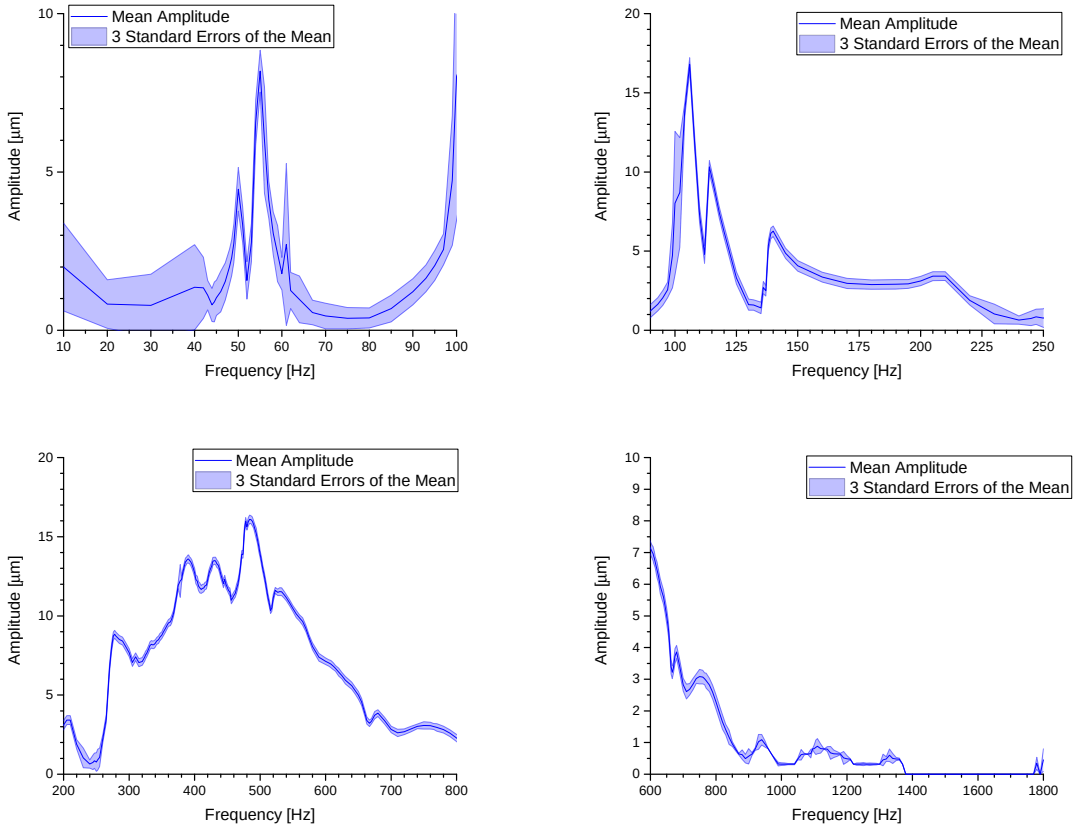

Figure 5.8: Frequency response of the layer 4 module prototype in four close-up views

5.2.3 Frequency Response of the Layer 3 Module Prototype

The Frequency Response of the layer 3 module prototype is shown in Fig. 5.10. The resonances are all inside an interval ranging from 100 Hz to about 900 Hz.

Beginning from the low frequency end, first there is a pair of weak resonances at 104 Hz and 116 Hz (Fig. 5.11).

The next resonance is at 180 Hz, followed by a peak at 250 Hz.

After the 250 Hz peak the vibration amplitude remains at an intermediate plateau level. This could either be a broad tail of one or several of the neighboring resonances or a superposition of several small peaks. Since there is some structure to the plateau, the latter seems more likely.

Following the plateau, there are two strong resonances at 460 Hz and 550 Hz. The dip between the two resonances is rather shallow, possibly suggesting a third, less strong resonance at about 500 Hz. This resonance, if it exists, can be identified as the 492 Hz speaker resonance (Fig. 5.5).

Finally, two weak resonances at 725 Hz and 800 Hz are visible at the high end of the resonance spectrum. The two speaker resonances at 1080 Hz and 1360 Hz (Fig. 5.5) are

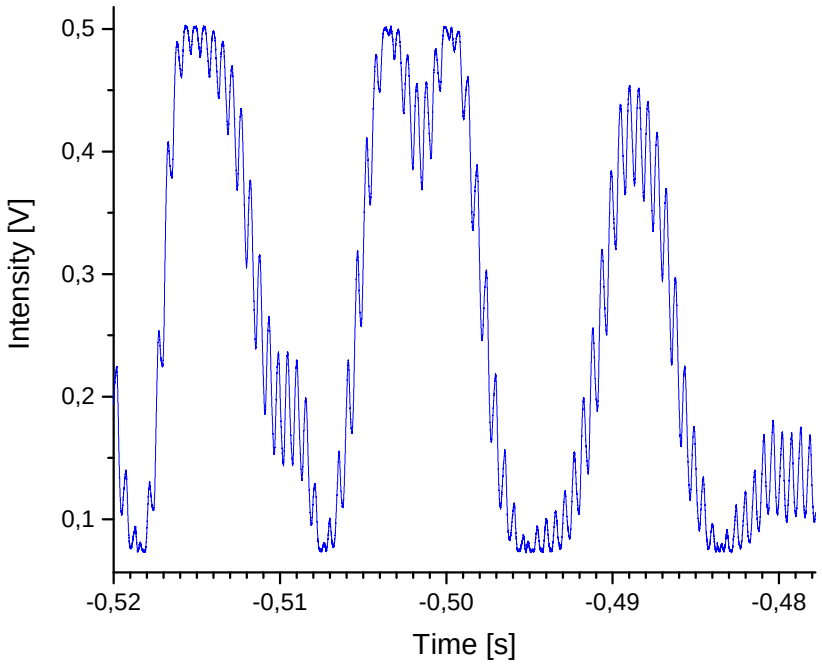

Figure 5.9: Interferogram of the layer 4 module vibration at a speaker frequency of 1800 Hz

not visible in this frequency response, but this may be due to the high noise in the relevant region (Fig. 5.11). As for the layer 4 module prototype, the response of the layer 3 module prototype was scanned for higher frequency resonances up to several kHz, but none were found.

5.2.4 Comparison

The frequency ranges covered by the layer four and layer 3 module resonances are roughly similar.

However, while the resonances in the layer four frequency response are similar in amplitude and none higher than 20 μm, the layer 3 frequency response shows large amplitude differences between the individual resonances. Also, the largest resonances in the layer 3 frequency response are more than twice as large as the largest layer 4 peaks. This could be due to the additional mass of the mirror glued to the layer 4 module prototype, since a higher mass means the same amount of energy transferred to the module leads to a smaller resulting module momentum, and thus a smaller momentum.

The added mirror mass would also lead to a decrease in the resonant frequencies (assuming a superposition of simple harmonic oscillators with $\omega_0 = \sqrt{\frac{k}{m}}$). This can indeed be seen when comparing the resonance spectra, for example, the first two resonances of layer

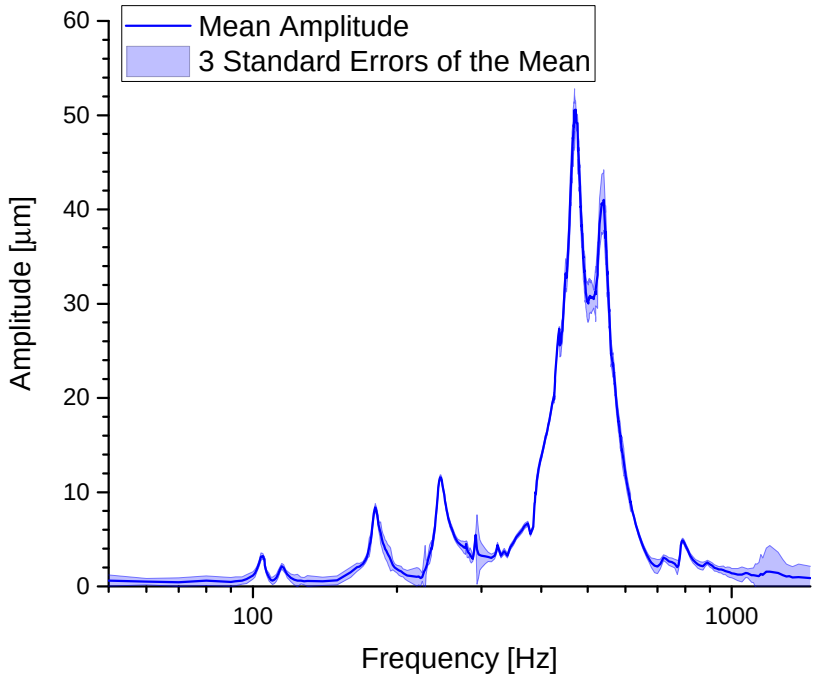

Figure 5.10: Full frequency response of the layer 3 module prototype

3 are at about 100 Hz, whereas the first two peaks in the layer 4 frequency response are at roughly 50 Hz.

Keeping in mind the mass-induced frequency shift, it is now possible to compare the structure of the resonance spectra of the module prototypes.

Both begin with a pair of weak resonances in the low frequency range, followed by two stronger resonances. Layer 4 then exhibits a very flat plateau of increased response, which is not seen in the layer 3 frequency response. There may be such a plateau in the layer 3 response as well, but it would overlap with the adjacent peaks, and is a lot more structured than the layer 4 counterpart. The frequencies of the plateau regions exhibit the same relative factor of roughly 2 that is known from the other features of the frequency response, however. If one accepts the explanation of the layer 4 plateau being individual resonances of broken glass plates superposed, then the increased structure in the layer 3 frequency response could be due to the glass plates in the newer layer 3 module prototype being mostly intact. This means that only a few different individual resonances contribute, and thus the plateau is less smooth.

After the plateau, layer 4 exhibits a superposition of a number of strong resonances, the strongest of which is the speaker resonance at about 500 Hz. This is very different from the layer 3 behavior, which has two strong resonances in this region, and if there is a peak at 500 Hz, it is far weaker than these resonances. The two frequency responses both

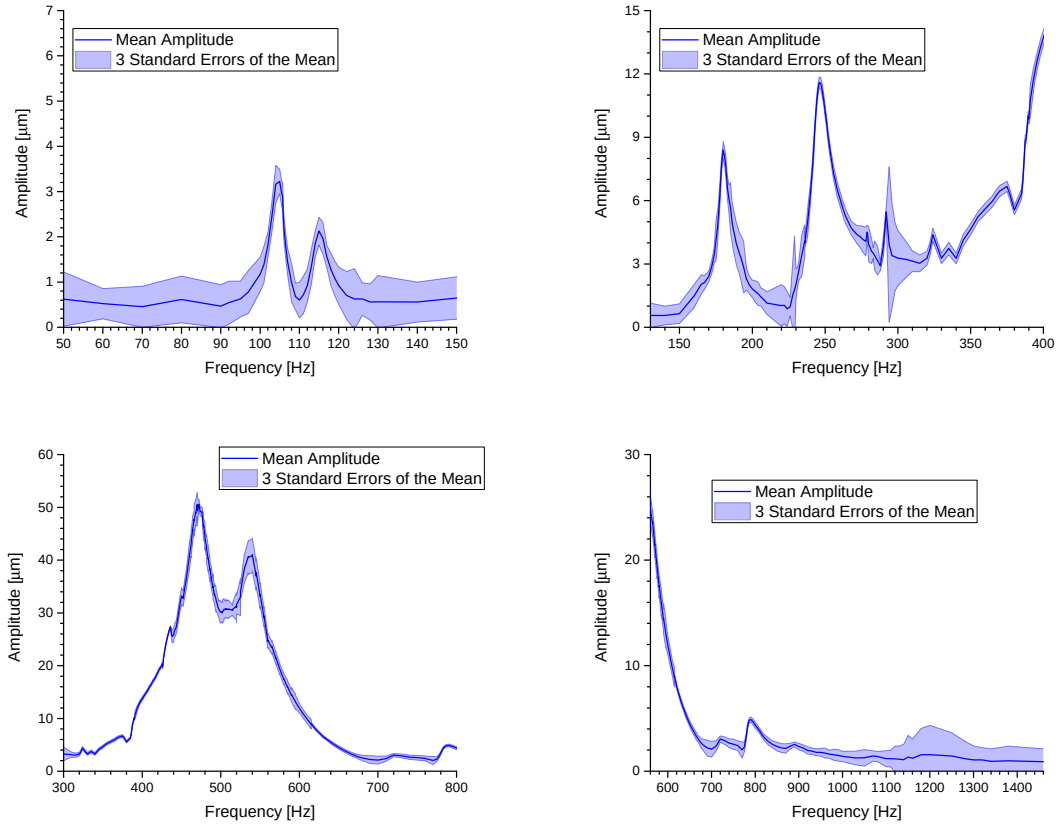

Figure 5.11: Frequency response of the layer 3 module prototype in four close-up views

exhibit a weak peak at about 800 Hz. However, this is not likely to be the same feature, since then one would expect a mass induced change in frequency. Additionally, while the layer 3 variant is well separated from the previous strong resonances, the layer 4 variant clings to the side of the stronger peaks.

After their strongest resonances, both module prototypes respond only very weakly to the speaker excitation, and beyond 1000 Hz, there are no more strong resonances.

5.3 Conclusion

In this chapter, the frequency response of the layer 3 and layer 4 module prototypes was examined. This was done using a speaker to excite vibrations at a range of frequencies, and recording the modules response with the Michelson interferometer. The aim of the measurement was to identify the resonant frequencies of the system so as to be able to avoid exciting these resonances in the final detector setup, which might impede detector precision.

For both modules, a wide range of resonances was observed. While there was some

distortion observed in the layer 4 measurement due to the added mass of the thick glass mirror, both modules showed a similar frequency spectrum. In general, frequencies between 50 Hz and 1000 Hz should be avoided, and the range between 300 Hz and 700 Hz is the most dangerous, since it exhibits the strongest resonances.

Chapter 6

Flow Induced Vibration

The planned cooling system of the Mu3e detector depends on cooling the pixel detectors and adjacent hardware by forced convection [12]. The forced convection will be realized using gaseous helium as coolant. The helium gas coolant will flow along the length of the detector in a slow ($4\,\frac{\mathrm{m}}{\mathrm{s}}$) global flow in the space between the detector elements, and a fast ($20\,\frac{\mathrm{m}}{\mathrm{s}}$) local flow, which will flow through the v-shaped folds in the kapton structure supporting the detector chips [11, 12]. Since both the support structure and the chips themselves are very lightweight and not very rigid, there is a potential risk of the cooling flow inducing vibration in the module. This could be problematic if the displacement amplitude of the module vibration would be large enough to decrease the resolution of the detector. A relevant vibration amplitude would need to be comparable to $50\,\mu$m, the thickness of one chip [1, 12]. To investigate whether the cooling-flow induced vibration is problematic or not, measurements with the Michelson interferometer were carried out. This chapter describes these measurements, the results of these measurements, and the conclusions drawn from the measurement results.

6.1 Measurements

For the measurement of flow induced vibration, the Michelson interferometer was used. The interferometer was mounted on an breadboard, which in turn rested on vibration isolating isopropane feet. Two module prototypes were tested: the layer 3 prototype, and the layer 4 prototype. For both prototypes, their response to local flow of air and helium was measured. Helium was used because it is the coolant that is planned to be used in the actual experiment. However, helium is less dense than air, and the measurements were carried out in an air atmosphere. To check whether the difference in density or the heterogeneity of the gas in the local flow and the surrounding gas might distort the measurement result, local air flow was used as well. The local gas flow velocity was varied across a wide range for both air and helium by varying the pressure difference between the gas at the inlet in to the module and the surrounding atmosphere. Gas flow was measured using two rotameters (one calibrated for helium, the other calibrated for air).

measurement on module	$\tilde{p}$ [bar]	q [Nl/min]	$\chi^2_{red.}$
layer 4	0.91	57.2	2.02
layer 3	0.94	62.1	0.37

Table 6.1: Fit parameters for the helium flow uncertainty estimate

Since the flow value read off from the rotameters is dependent on the density of the gas, and the density in turn is pressure dependent, a correction factor [1] was applied to the read-off flow value Q_r [12]:

$$Q = Q_r \sqrt{\frac{p_{cal}}{p}} \tag{6.1}$$

where $p_{cal} = 2\,\text{bar}$ is the pressure at which the rotameters were calibrated by the manufacturer, and p is the gas pressure during the measurement, which was measured using barometers.

With the cross-sectional area of one v-fold $A = 10\,\text{mm}^2$ and $n = 4$ the number of v-folds [12], the flow velocity is:

$$v = \frac{Q}{nA} \tag{6.2}$$

The uncertainties for the flow measurements are based on the accuracy to which the rotameters could be read off, which was $\delta Q_r = 0.05\,\frac{\text{Nl}}{\text{h}}$ for the air measurements, and $\delta Q_r \approx 1.1\,\frac{\text{Nl}}{\text{min}}$ in the case of helium[2]. The error of the pressure measurements was estimated to be $\delta p = 0.05\,\text{bar}$ for the helium measurements, and $\delta p = 0.25\,\text{bar}$ for the air measurements.

The coolant gas pressures measured are highly correlated with the normed flow values read off of the rotameter (Figs. 6.1 and 6.2). Thus simple Gaussian error propagation without taking into account the correlation would lead to wrong uncertainty estimates for the gas flow Q.

In the case of helium , the correlation can be parametrized with an exponential model (Fig. 6.1):

$$p = \tilde{p} e^{\frac{Q_r}{q}} \tag{6.3}$$

with $\tilde{p}$ and q model parameters. To estimate the uncertainty of the helium flow Q, (6.3) was inserted in (6.1). Using $\tilde{p}$ and q as determined from a fit of (6.3) to the data, the

[1] Whether the correction factor has already been applied or not on a particular value is marked by the units used: uncorrected values are given in normed units: $\frac{\text{Nl}}{\text{min}}$ or $\frac{\text{Nm}^3}{\text{h}}$, whereas pressure-corrected values are given in $\frac{\text{l}}{\text{min}}$ or $\frac{\text{m}^3}{\text{h}}$ instead

[2] The resolution of the calibration table provided by the rotameter manufacturer varied slightly, thus there is a slight variance in the normed helium flow uncertainty

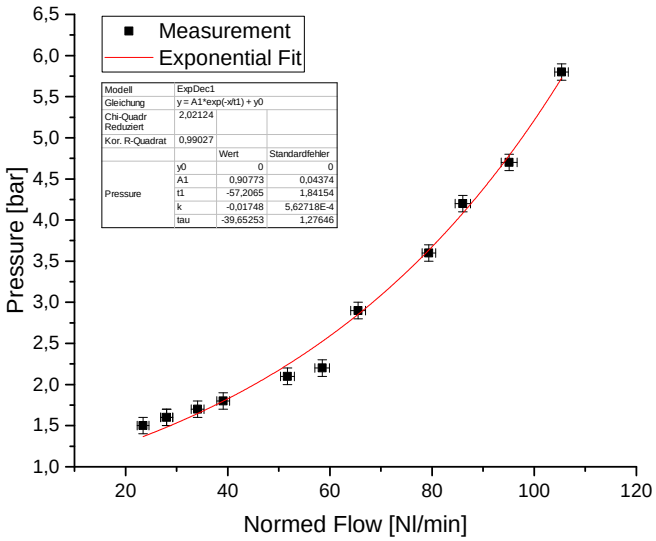

Figure 6.1: Correlation of normed helium flow and absolute coolant gas pressure

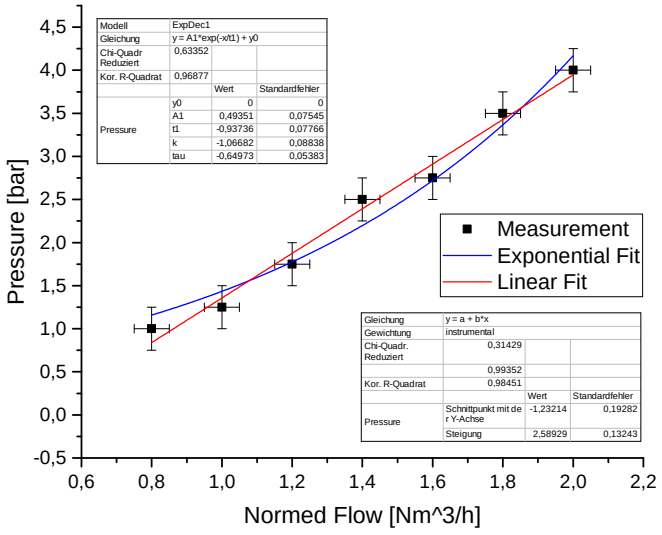

Figure 6.2: Correlation of normed air flow and absolute coolant gas pressure

measurement on module	correlation coefficient
layer 3	0.99004
layer 4	0.97226

Table 6.2: Correlation coefficients used in the air flow uncertainty estimate

uncertainty δQ was then estimated using Gaussian error propagation and the read-off accuracy of the helium rotameter δQ_r:

$$\delta Q = \sqrt{\left(\frac{\partial Q}{\partial p}\frac{\partial p}{\partial Q_r} + \frac{\partial Q}{\partial Q_r}\right)^2} = \sqrt{\frac{p_{cal}}{\tilde{p}}} e^{-\frac{Q_r}{2q}} \left|1 - \frac{Q_r}{2q}\right| \delta Q_r \tag{6.4}$$

The fit results used are given in table 6.1.

In the case of air flow, the correlation of normed flow and coolant gas pressure is linear (Fig. 6.2). The uncertainty of the air flow δQ was thus estimated as:

$$\begin{aligned}(\delta Q)^2 &= \begin{pmatrix}\frac{\partial Q}{\partial Q_r}\\ \frac{\partial Q}{\partial p}\end{pmatrix} \cdot \begin{pmatrix}(\delta Q_r)^2 & \mathrm{Corr}(Q_r,p)\delta Q_r \delta p\\ \mathrm{Corr}(Q_r,p)\delta Q_r \delta p & (\delta p)^2\end{pmatrix} \cdot \begin{pmatrix}\frac{\partial Q}{\partial Q_r}\\ \frac{\partial Q}{\partial p}\end{pmatrix}^T \\ &= (\delta Q_r)^2 \frac{p_{cal}}{p} - Q_r \frac{p_{cal}}{p^2}\mathrm{Corr}(Q_r,p)\delta Q_r \delta p + (\delta p)^2 \frac{Q_r p_{cal}}{4p^3}\end{aligned} \tag{6.5}$$

where $\mathrm{Corr}(Q_r, p)$ is the Pearson product-moment correlation coefficient as determined from the data and δQ_r and δp are the estimated read-off uncertainties of the normed flow and pressure measurement, respectively. The correlation coefficients used are given in table 6.2.

Because the flow induced vibrations were expected to be strongest near the center of the modules, the central mirrors were used in all flow induced vibration measurements.

6.2 Results

6.2.1 Amplitude of Flow Induced Vibration

For each flow velocity, a several second long interferogram was recorded and movement amplitudes were counted using a program and counting algorithm that were developed in the context of another bachelor thesis [17]. This resulted in a wide distribution of vibration amplitudes counted for each flow value, and a high number of counted amplitudes (Fig. 6.5). The precise number of counts varies with frequency of vibration and length of interferogram, but several thousand movements per interferogram are a typical number. To describe and compare these distributions, three characteristics are considered: the average movement amplitude of the sample, the movement amplitude one standard deviation above the average movement amplitude, and the largest observed amplitude. The uncertainty of the maximum amplitude was estimated as the uncertainty of a single movement count,

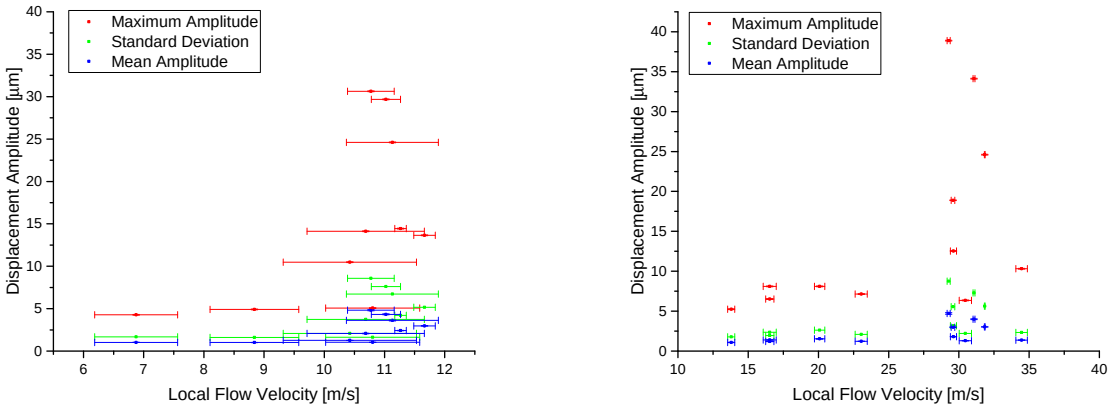

Figure 6.3: Flow induced vibration amplitudes in the layer 4 module prototype. (left: air flow; right: helium flow.) For higher velocities, increased pressure increases mass-flow by increasing the gas density, and not the flow velocity. This effect is only apparent after applying the pressure correction (6.1) and leads to the multiple overlapping data points at high flow velocities.

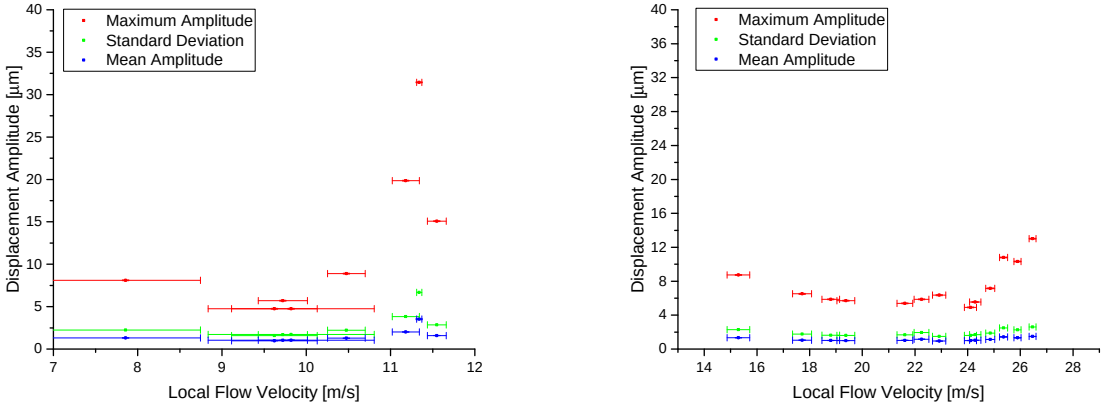

Figure 6.4: Flow induced vibration amplitudes in the layer 3 module prototype. left: air flow; right: helium flow.

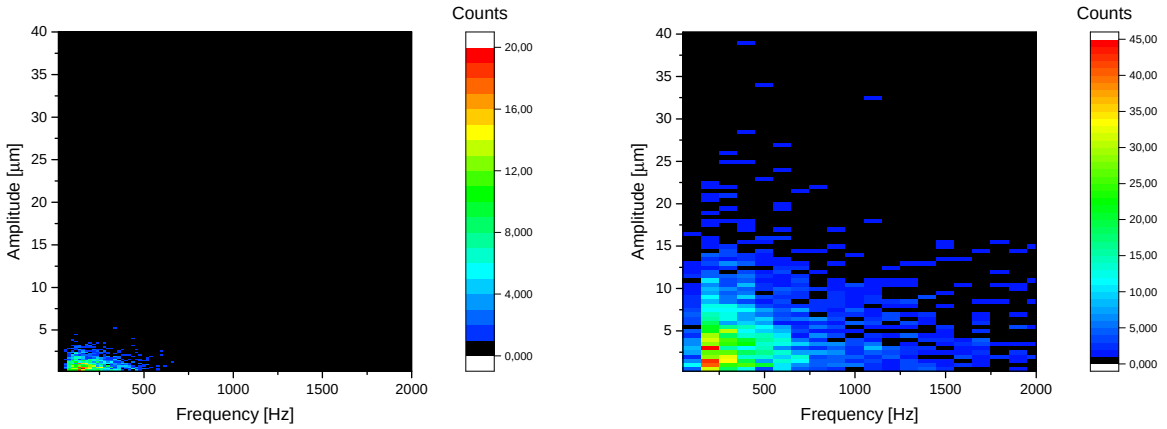

Figure 6.5: Distribution of observed helium-flow induced vibrations in layer 4 across frequencies and amplitudes (left: $14\,\frac{\mathrm{m}}{\mathrm{s}}$ flow velocity, right: $30\,\frac{\mathrm{m}}{\mathrm{s}}$ flow velocity)

which is $\frac{636.5\,\mathrm{nm}}{4\sqrt{12}} \approx 0.013\,\mu\mathrm{m}$. Because the program counted not from intensity maximum to intensity maximum, but from extremum to extremum, $\frac{\lambda}{4}$ was the smallest unit of counting, and thus the uncertainty was $\frac{\lambda}{4\sqrt{12}}$. The uncertainty of the averages was estimated as the standard error of the mean. The results are shown in Fig. 6.3 and Fig. 6.4.

The largest vibration amplitudes occur at high local flow velocities (Figs. 6.3 and 6.4). In the case of air flow, high flow velocities are above $10\,\frac{\mathrm{m}}{\mathrm{s}}$. At this point, pressure increases begin to primarily compress the air instead of accelerating it. However, air flow is not the relevant case, which is helium flow. For helium, high flow velocities, where pressure increases dominantly compress, are at $30\,\frac{\mathrm{m}}{\mathrm{s}}$ and above. As in the case of air, these are the flow velocities where the highest maximum amplitudes are. Thus both helium and air behave similarly: In the respective low velocity range, the vibration amplitudes are of comparable, noncritical size. In the respective high velocity region near the highest velocity achievable by increasing pressure, dangerously large movements can be found. The size of these movements is similar for both helium and air flow. Thus the only difference between the behavior of air and helium is in the velocity scale, which is due to different gas properties (density, compressibility etc.). Therefore the fact that the gas used for the local cooling flow differed from the surrounding atmosphere does not cause larger flow induced vibration amplitudes.

The maximum amplitudes are below $40\,\mu\mathrm{m}$ for layer for and layer 3, with both helium and air (Figs. 6.4 and 6.3). In several cases the amplitudes found come close to this limit. However, the counting algorithm sometimes misidentified turning points [17]. Thus it is not certain that the largest movement amplitudes found, being individual counting results, are not due to counting errors.

The average flow amplitudes are significantly smaller than $5\,\mu\mathrm{m}$. This is true for both the layer 3 and the layer 4 module, for air and for helium flow, and across all flow velocities. The sample standard deviations are usually similarly large. At the highest flow velocities,

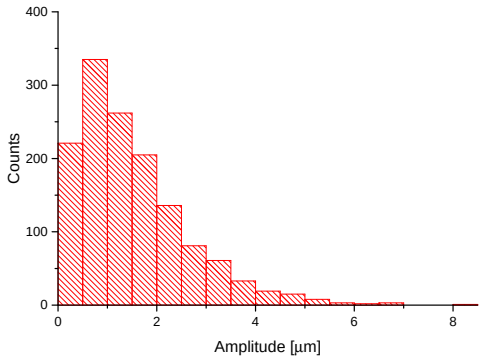

(a) Layer 4 at 20 $\frac{\mathrm{m}}{\mathrm{s}}$ flow velocity

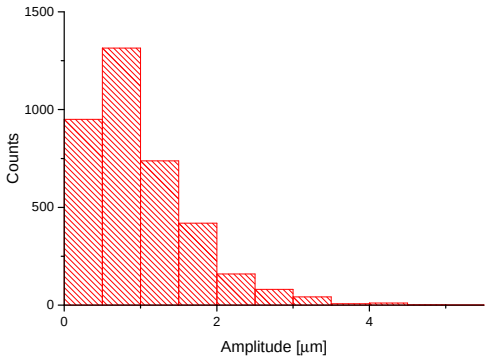

(b) Layer 3 at 21.6 $\frac{\mathrm{m}}{\mathrm{s}}$ flow velocity

Figure 6.6: Amplitude histograms for helium flow induced vibrations

they tend to be larger than at lower velocities. For those there are movement amplitudes at a scale which can influence the spatial detector resolution (Figs. 6.4 and 6.3).

For layer 4, at the relevant helium flow speed of 20 $\frac{\mathrm{m}}{\mathrm{s}}$, the average vibration amplitude is 1.5 μm, the standard deviation is 1.1 μm. The highest amplitude found at this flow velocity is 8.1 μm. It is removed from the average by about 6 σ. The duration of the corresponding movement is approximately 2.5 ms. With a measurement lasting 4 s, the highest amplitude occurred once in about 1600 of the periods it might have occurred. This is far more often than the frequency of once in $5 \cdot 10^9$ that 6 σ suggests when assuming a Gaussian distribution. However, the observed amplitude distribution is not Gaussian (Fig. 6.6a). It is wider than its sample standard deviation would suggest. Thus one cannot conclude that the highest value observed is at a significant distance from the average. In a comparable measurement it might therefore show up as well.

For layer 3 there is no data point precisely at a flow velocity of 20 $\frac{\mathrm{m}}{\mathrm{s}}$. There is data at 21.6 $\frac{\mathrm{m}}{\mathrm{s}}$ and 19.4 $\frac{\mathrm{m}}{\mathrm{s}}$ flow velocity however. These samples have maximum displacement amplitudes of 5.4 μm and 5.7 μm. With mean amplitudes of 1.0 μm and 0.99 μm and standard deviations of 0.7 μm and 0.6 μm, the maximum values differ from the averages by about 6.7 σ and 6.3σ, respectively. However, because the amplitude distribution is not Gaussian (Fig. 6.6b), this does not necessarily mean that the difference is significant. With movement durations of approximately 0.83 ms and 1.6 ms and a measurement duration of 4 s, the respective frequencies of occurrence of the maximum amplitudes are about once in 5000 and 2500 potential periods.

6.2.2 Frequency of Flow Induced Vibration

In Figs. 6.3 and 6.4, there is only a small correlation between volume flow and average vibration amplitude. This is because the module tends to react to higher local flow not so much with larger movements, but predominantly with faster ones. An example is given in

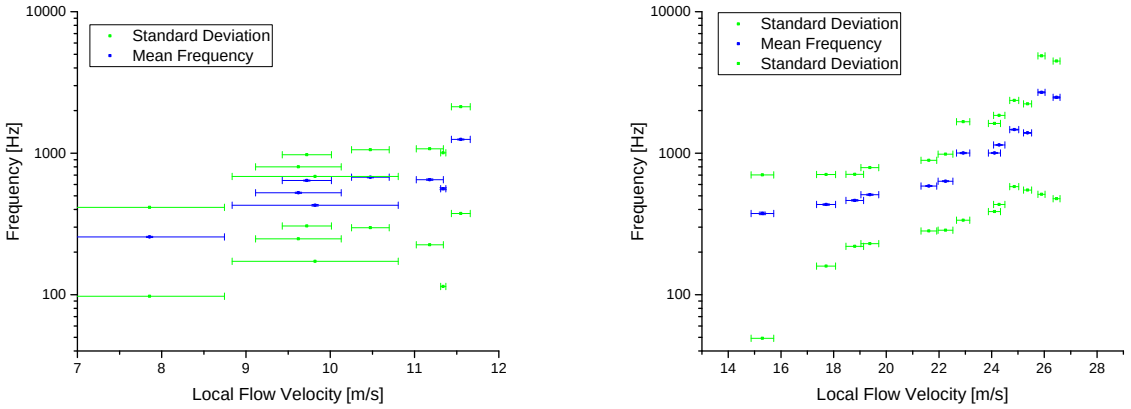

Figure 6.7: Flow induced vibration frequencies in the layer 3 module prototype (left: air flow; right: helium flow)

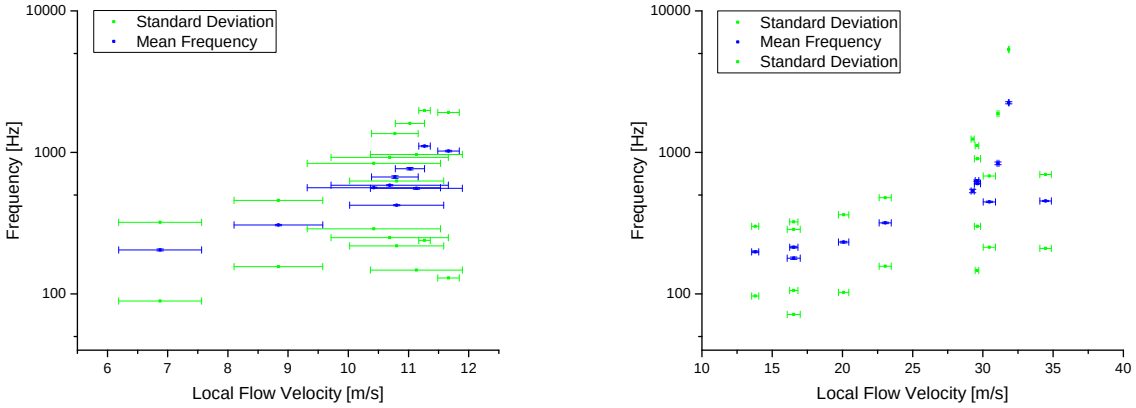

Figure 6.8: Flow induced vibration frequencies in the layer 4 module prototype (left:air flow; right: helium flow)

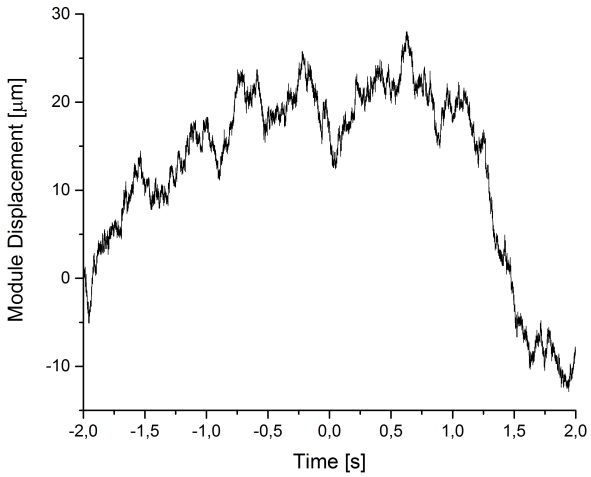

Figure 6.9: Alternating sum of module movements for the layer 3 module at 19.4 $\frac{\mathrm{m}}{\mathrm{s}}$ helium flow velocity

Fig. 6.5. The increase in flow velocity means a slightly higher occurrence of high-amplitude movements, but mostly it leads to a dramatic increase in vibration frequency[3].

This increase of vibration frequency with increasing flow velocity is shown in Figs. 6.7 and 6.8. The distribution is described by the average frequency and the standard deviation from the average. The uncertainty of a single frequency is estimated as the standard error of the mean. However, there are systematic effects in either the measurement or the counting procedure this uncertainty does not account for. This can be seen by looking at the right plot in Fig. 6.8. The measurement at 17 $\frac{\mathrm{m}}{\mathrm{s}}$ was done twice. While the difference between the measurements is small compared to the width of the distribution, it is far larger than the standard error of the mean. On the other hand, this might be because the observed frequency distributions are not Gaussian. They show significant asymmetry (Fig. 6.5).

The distributions observed in the frequency range are wider than the amplitude distributions, they typically span half an order of magnitude. They also show a strong correlation with the local gas flow. This indicates that although it does not show in the amplitude data very much, the local flow has a strong effect on the module movement.

Furthermore, the frequency distributions are such that the majority of vibrations has frequencies between 100 Hz and 1000 Hz. This is in agreement with the frequency response results from chapter 5.

6.2.3 Hidden Modes of Vibration

As previously mentioned in section 4.2, the direct counting of maxima in the interferogram can only reveal the highest-frequency vibration of all those vibrations that have amplitudes

[3]The term is used very loosely here. Inverse movement duration would be more accurate.

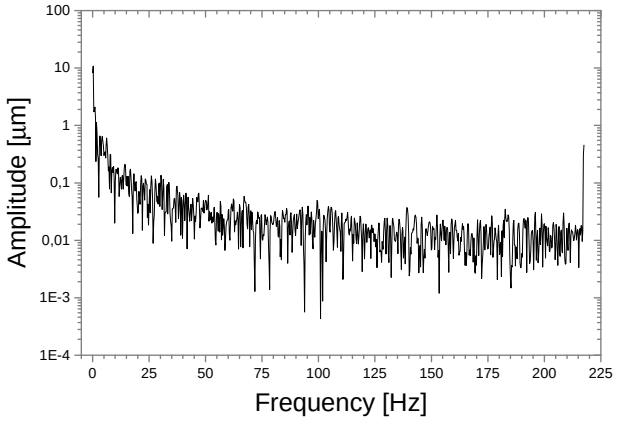

Figure 6.10: FFT of the Data in Fig. 6.9

larger than $\frac{\lambda}{2}$.

To check whether there were lower frequency modes that were not observed directly but still had amplitudes large enough to endanger detector precision, the individual movement lengths were added up in chronological order, with an alternating prefactor of 1 or -1 as specified in (4.2). The result is the module displacement at the time of the turning points, over time. An example is given in Fig. 6.9. It should be noted that there is a certain random error in the data, due to the fact that the counting algorithm sometimes misses movements, or counts slightly wrongly [17].

To more specifically check for hidden modes, a Fast Fourier Transform (FFT) of the module position over time was calculated from the alternating sums for all measurements.

The upper end of the FFT result frequency spectrum is determined by the sample rate of the input data. In this case, this is the frequency of turning points, or twice the frequency of the module vibration. Thus the FFT covers exactly the interesting range of frequencies below the directly observable ones.

The lower end of the FFT result is determined by the frequency resolution of the discrete Fourier Transform, which is approximately[4] the inverse duration of the sample. In a typical measurement of e.g. 4 s duration, this means a lower frequency limit of about 250mHz. The frequency response measurements of the modules indicate that this is well below the frequencies at which the module should be expected to respond strongly. Thus the FFT should be capable of giving a reasonable indication of whether there are hidden modes in the flow induced vibration signals or not. In order to keep the amplitude accuracy of the FFT as high as possible, a Blackman window function was used.

As an example, the absolute value of the FFT of the data in Fig. 6.9 is given in Fig. 6.10. The spectrum is very flat, except for the edges.

The rise at the edges of the spectrum could be a numerical effect. Frequencies near the low end are close to the frequency resolution. Because of this they are susceptible to noise

[4]The exact frequency resolution depends on the window function used

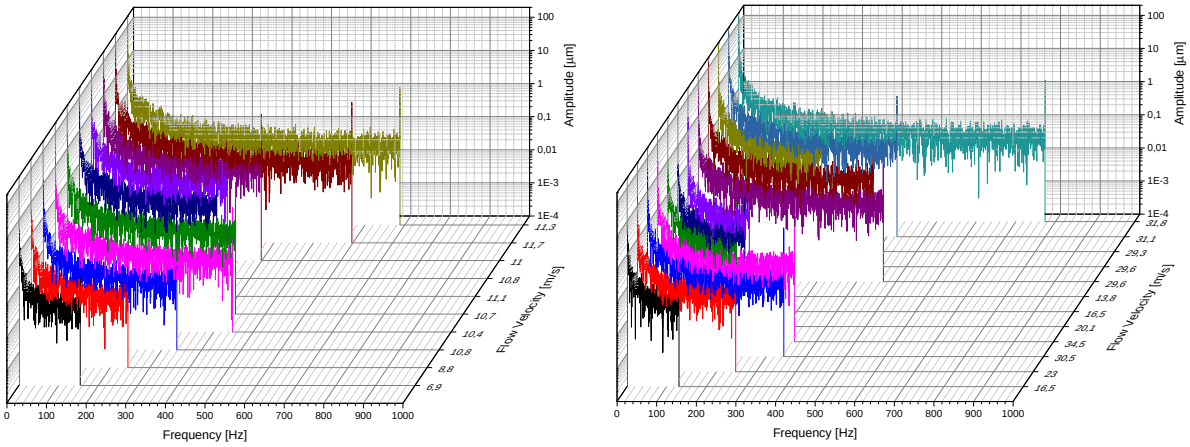

(a) Air flow (b) Helium flow

Figure 6.11: Discrete Fourier transform results of the module displacement of layer 4

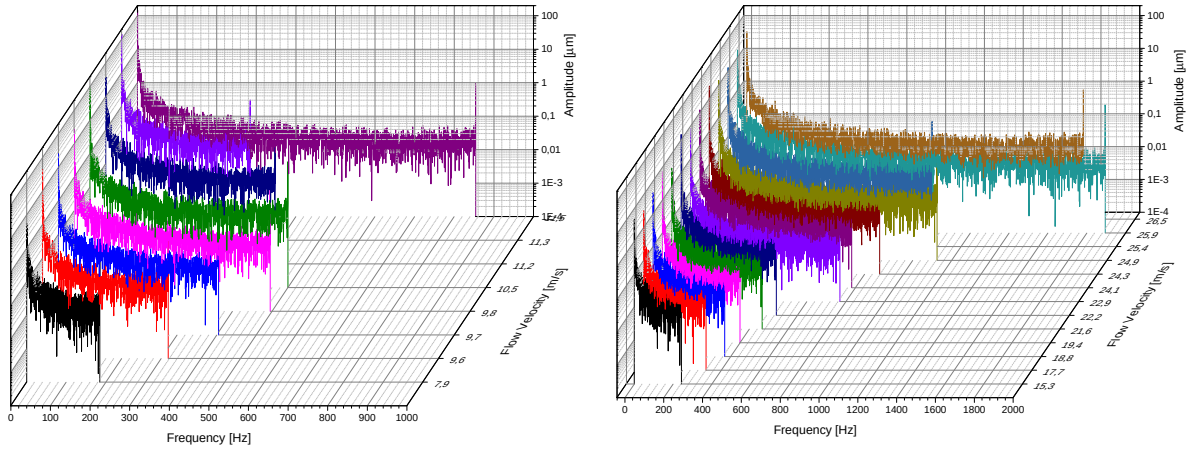

(a) Air flow (b) Helium flow

Figure 6.12: Discrete Fourier transform results of the module displacement of layer 3

in the input data, and edge effects. Frequencies near the high end are difficult to treat numerically, because the alternating sum does not give data at a single fixed rate. This is because of the width of the frequency distribution of flow induced vibrations (Figs. 6.8 and 6.7). The average frequency of the turning points was used for the sampling. This can distort the result at the upper end of the spectrum.

Alternatively, the rise at the high end could mark the beginning of the frequency distribution that is seen in Fig. 6.7.

The rise at the low end could alternatively be due to the increasing uncertainty of the alternating sum across large time intervals.

This increase in uncertainty for larger time intervals is due to the way that the alternating sum was calculated. The alternating sum picks up all errors along its way. This means that a small amplitude and low frequency mode will have a huge error [5]. This is still true for an amplitude at or close to zero.

As one can see in Figs. 6.11 and 6.12, the features seen in Fig. 6.10 are typical for all the Fourier transform results. Both modules exhibit the same flat spectrum across all measured flow velocities. Both modules show the slight rise in amplitude towards the beginning of the regime of counted amplitudes at the upper end of the frequency spectrum.

Both modules show the strong peak in amplitude at the low end of the spectrum as well. However, this peak also appears to vary wildly in magnitude. The peculiar thing about this variation is that it does not seem to be correlated to the gas flow at all. This lack of correlation indicates that the peak at the low frequency end is indeed due to noise, as one would expect an actual low frequency mode to be either correlated to the flow, or independent, but constant. Additionally, only the layer 4 module exhibits any resonances below 100 Hz (Figs. 5.10 and 5.7). However, the low frequency rise is the same for both modules. And the layer 4 FFT results do not show a peak or lobe at 50 Hz, where the resonance is.

But in order to be certain that the modules do not vibrate in some extremely low-frequency mode with a dangerous amplitude, longer measurements are necessary. With longer measurements, the lower frequency end of the discrete Fourier transform can be pushed lower. Thus, numerical effects due to being close to the low end of the spectrum get pushed down as well. This could allow to distinguish an actual low frequency mode from numerical edge effects and noise. But in the scope of this thesis, the duration of single measurements is limited by the counting algorithm [17], which is not stable when processing overly large files.

6.3 Conclusion

The aim of the measurements described in this chapter was to verify that the local cooling flow of the Mu3e cooling system does not induce vibrations in the detector modules that are large enough to decrease the vertex resolution of the detector. To this end, the vibration

[5] compare also 4.4 and its discussion

of module prototypes of the third and fourth detector layers caused by the local flow were measured using a Michelson Interferometer.

At the planned local cooling flow of 20 $\frac{\mathrm{m}}{\mathrm{s}}$, the observed vibration amplitudes are smaller than 10 μm. The average amplitudes are all 6 standard deviations or more smaller than that. However, because the amplitude distribution is not Gaussian, this does not mean that these amplitudes rarely occur. Still, because the movement amplitudes at this velocity are so small, they can be considered not to impede detector resolution much.

This is not true for all flow velocities at which measurements were done. The highest observed amplitudes for flow velocities of 30 $\frac{\mathrm{m}}{\mathrm{s}}$ are larger than 10 μm in several cases. Thus they are not negligible compared to the thickness of one detector chip of 50 μm[1], or the spatial detector resolution of about 30 μm[13]. Therefore the local cooling flow velocity should be kept well below that amount.

The average frequency of the directly observed vibrations was usually several hundred Hz or higher (Figs. 6.7 and 6.8), and the detector modules have resonances at frequencies lower than this(Fig. 5.7). Thus, the possibility remained that the modules vibrated in lower frequency modes, with larger and potentially dangerous vibration amplitudes. In order to check whether such hidden modes of vibration had been overlooked in the first analysis, a FFT analysis of the time integrated movement amplitude was performed. The result of the FFT showed that there were no such hidden modes of vibration (Figs. 6.11 and 6.12).

Thus, the overall conclusion of this chapter is that vibrations induced by the local cooling flow do not influence the resolution of the detector system, as far as they could be reliably observed. Two problems remain unresolved, however.

The first is the effect of the global cooling flow. On the one hand, since the global flow is far slower than the local flow, one should expect even less of an influence. On the other hand, the global flow is in contact with far more of the module surface. Thus its influence on module vibration should be investigated.

The second is the low frequency rise in the FFT analysis. It is not correlated with the flow velocity, and does not agree with the resonances observed in this frequency range. This could indicate that it is not a physical effect, but a numerical one. But the maximum of the rise is larger than 100 μm in some instances, which is large compared to e.g. the thickness of one chip of 50 μm. The effect of such a vibration on detector resolution, if it does occur, would be devastating. Thus it needs to be investigated in more detail.

To do this, several approaches are possible.

The one mentioned previously is increasing the measurement duration to better cover the low frequency range.

One can also think of ways to improve the identification of turning points, and thus the reliability of the results, by modifying the setup. A simple modification would be to excite a module vibration at a frequency much higher than typical flow induced vibration frequencies - tens of kilohertz high. Such a vibration has an amplitude far lower than $\frac{\lambda}{4} \approx 160\,\mathrm{nm}$. Thus it shows up in the interferogram as a small intensity modulation on top of the usual peak-turning point pattern (Fig. 5.9). If the sine in (4.1) is near an extremum, this modulation is small. If a turning point occurs away from that maximum the modulation is large. By using this forced modulation as an indicator of true turning

points, counting errors due to modulation of the visibility could be reduced. However, in the case of a turning point coinciding with an extremum, this method does nothing to reduce ambiguity.

Another setup modification to reduce ambiguity in assigning turning points is the use of quarter wave plates. The joined, interfering beam is split into two beams, both showing interference. In each beam, a quarter-wave plate is placed, and rotated such that the wave plates' ordinary axis is aligned with the beams polarization in one beam, and orthogonal to it in the other. The two beams will thus be phase shifted by $\frac{\pi}{2}$ with respect to one another. Then the two beam intensities need to be measured with two photo-diodes. Placement of the diodes will need to be such that they detect the intensity in equivalent areas of the two interference patterns. The phase $\Phi(t)$ of the light can then directly be determined from the ratio of the two intensities [6] $I_1(t), I_2(t)$:

$$\Phi(t) = \arctan\left(\frac{I_1(t)}{I_2(t)}\right) \tag{6.6}$$

The result is only the absolute phase modulo 2π, but knowledge of the absolute phase is not required. The ambiguity of turning point identification is removed, since Φ is a linear function of the module displacement.[7]

[6] Minus the baseline intensity I_0, which needs to be measured as well

[7] The idea to introduce an optical phase shift, although by different means, has been adapted from [16]

Chapter 7

Module Tilt when Introducing Local Flow

While measuring flow induced vibration with the Michelson Interferometer, the laser beam shifted very noticeably when the local flow changed. This shift of the laser beam reflected from the mirror on the module made the module beam stop overlapping with the reference beam. In order to have the beams overlap and interfere again, the reference mirror and the module were tilted slightly. Because tilting the module was able to eliminate the immediate problem, the observed shift of the laser beam was attributed to the module deforming when the local flow changes. This deformation would be different from the vibration phenomena studied before, because those are small oscillations around a constant mean baseline. Here, the dependence of this baseline on the flow characteristics is the point of interest. In this chapter, the modified setup used to quantify the module tilt, as well as the results of those measurements and their implications are described.

7.1 Setup

The Setup used to measure the module tilt is illustrated in Fig 7.1. The angle α is the tilt of the module at the point where the laser beam is reflected by the mirror. In order to access this quantity, the final beam tilting angle ϵ is measured.

To measure ϵ, a screen 12 cm wide and 12 cm high, made of a 8 mm thick metal was used. On the screen, a square sheet of millimeter scale graph paper was taped. Thus the laser spot position could be read off with millimeter precision. The laser spot size depends on the chosen collimation lens position and the screen position. Typically, the spot was between one and two centimeters wide along its long axis.

For each measurement of ϵ, the screen was placed in two parallel positions, separated by a fixed distance, which was also measured. The spot position was determined by reading off the position of the edges of the spot in both x and y direction (given by the two directions of the graph paper, where x is taken to be horizontal and y vertical) and taking the average of theses two values as the position of the center of the laser beam in x and y direction.

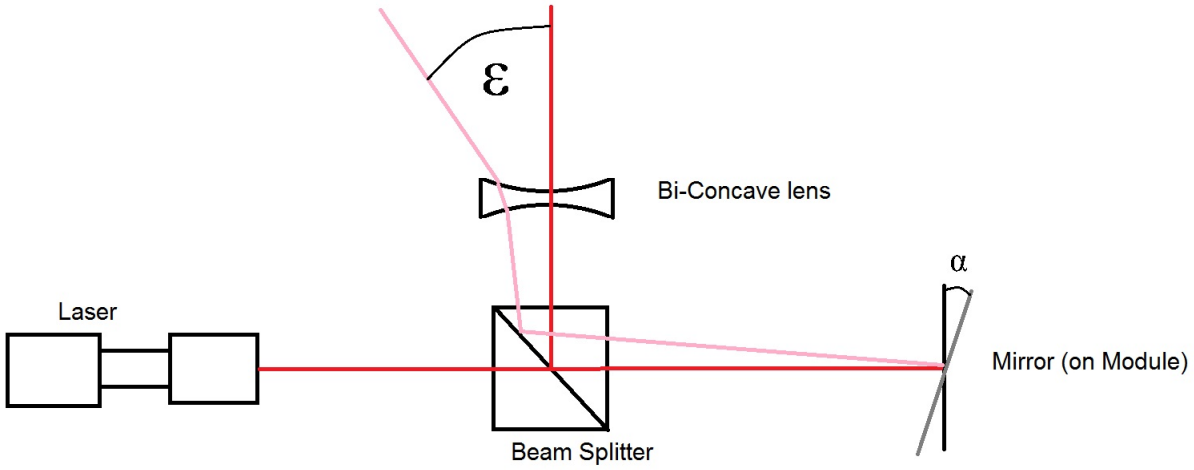

Figure 7.1: Sketch of the setup for measuring the module tilt

Along with the screen displacement between the two screen positions d_S, the spot position (Δx,Δy) was then used to calculate (ϵ_x,ϵ_y) using :

$$\epsilon_i = \arctan\left(\frac{\Delta i}{d_S}\right) \qquad i \in \{x, y\} \tag{7.1}$$

There are two main reasons for using this setup, instead of a more simple one where the laser is pointed at an angle onto the module and mirror and then the movement of the laser spot on a sufficiently distant screen is measured.

Firstly, the setup used is very similar to the one used for the interferometer measurements. This makes it easy to ensure that the conditions of the measurements are similar to those under which the module tilt was first observed. If in a future measurement the problem of module tilt were to reappear, quantifying the problem could be done quickly. Only minor modifications to the setup would be necessary, as opposed to taking the entire setup apart and building another one.

Secondly, the incident beam hitting the mirror normal to its surface means that for small tilting angles α, only the tilt of the module surface affects the beam tilt, and a translational displacement of the surface does not affect the beam shift.

Apart from it making switching setups easier, the advantage of using the biconcave lens here is that it strongly increases the final tilting angle ϵ without requiring a proportionately larger setup.

7.2 Relating Beam Tilt and Mirror Tilt

To find the relation between the module tilt angle α and the mirror tilt angle ϵ, geometrical optics was used. Instead of considering the entire beam, an idealized central ray is used in the calculations. Because the ray is just reflected in the beam splitter, its tilt does not change there, so the problem can be described by the simplified geometry in Fig. 7.2. Because the incidence angle equals the reflectance angle for specular reflection, $\beta = 2\alpha$ (Fig. 7.3).

Using the sum of angles in euclidean geometry, one arrives at the following three relations:

$$\begin{aligned} \pi &= \kappa_1 + \beta + (\pi - \delta_1) \\ &\iff \delta_1 = \kappa_1 + \beta \end{aligned} \tag{7.2}$$

$$\begin{aligned} \pi &= \delta_2 + \epsilon + (\pi - \kappa_2) \\ &\iff \delta_2 = \kappa_2 - \epsilon \end{aligned} \tag{7.3}$$

$$\begin{aligned} \chi + \theta_1 + \theta_2 = \pi &= \chi + \delta_1 + \delta_2 \\ \Rightarrow \theta_1 + \theta_2 &= \delta_1 + \delta_2 \end{aligned} \tag{7.4}$$

With the Law of Sines one gets:

$$\frac{\sin(\kappa_1)}{x_1 - R} = \frac{\sin(\beta)}{R} \tag{7.5}$$

$$\frac{\sin(\pi - \kappa_2)}{R + d_L} = \frac{\sin(\kappa_2)}{R + d_L} = \frac{\sin(\epsilon)}{R} \tag{7.6}$$

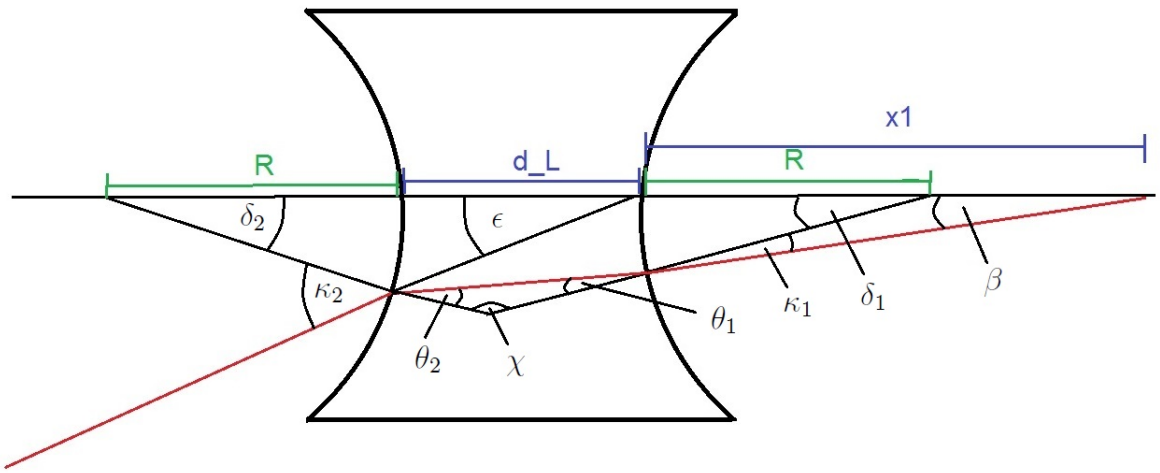

Figure 7.2: Geometry for determining $\alpha(\epsilon)$

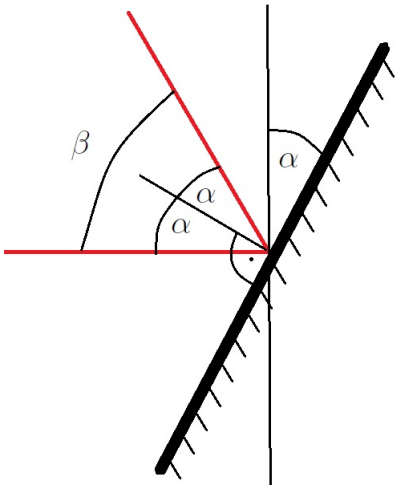

Figure 7.3: Relation of α and β

Finally, using Snell's Law of Refraction with n the refractive index of the lens material and approximating the refractive index of air as 1, the set of equations is completed:

$$\frac{\sin(\kappa_1)}{\sin(\theta_1)} = n \tag{7.7}$$

$$\frac{\sin(\kappa_2)}{\sin(\theta_2)} = n \tag{7.8}$$

To solve this set of equations ((7.2) through (7.8)), first δ_1 and δ_2 are eliminated by inserting (7.2) and (7.3) in (7.4) resulting in :

$$\theta_1 + \theta_2 = \kappa_1 + \kappa_2 + \beta - \epsilon \tag{7.9}$$

Using (7.7) and (7.8) in (7.9) then eliminates θ_1 and θ_2:

$$\arcsin\left(\frac{\sin(\kappa_1)}{n}\right) + \arcsin\left(\frac{\sin(\kappa_2)}{n}\right) = \kappa_1 + \kappa_2 + \beta - \epsilon \tag{7.10}$$

To get rid of κ_1 and κ_2, (7.5) and (7.6) are inserted in (7.10). Using that $\beta = 2\alpha$ (Fig. 7.3), the solution is:

$$\begin{aligned}\arcsin\left(\frac{x_1/R - 1}{n}\sin(2\alpha)\right) - \arcsin\left(\left(\frac{x_1}{R} - 1\right)\sin(2\alpha)\right) - 2\alpha \\ = \arcsin\left(\left(\frac{d_L}{R} + 1\right)\sin(\epsilon)\right) - \arcsin\left(\frac{d_L/R + 1}{n}\sin(\epsilon)\right) - \epsilon\end{aligned} \tag{7.11}$$

Using this relation to get $\alpha(\epsilon)$ for various measured values of ϵ would, however, require numerically solving it for every single value separately. This makes analysis of the measurement data time consuming and since it is by no means obvious that there is only one

α for every ϵ that solves (7.11), it might introduce ambiguity. To avoid ambiguity and enable speedy evaluation, a linearized version of (7.11) was used:

$$\alpha(\epsilon) = \frac{\epsilon}{2}\frac{d_L(1-n)+R}{x_1(n-1)+R} \tag{7.12}$$

Since in this approximation, the Taylor series of the sine function around 0 is used only up to linear order, small angles are required. This assumption is justified, however, as will be demonstrated in the following section.

7.3 Testing the Setup

To verify that (7.12) describes the relation of α and ϵ and that no crucial aspect of the test setup was ignored, a test measurement was performed. In the test measurement, the mirror on the module in the setup (Fig. 7.1) was replaced with a mirror on a rotating stage. The rotating stage allowed turning the mirror around its vertical axis with a precision of $5'$, which was used as the error on α. The mirror was then turned, the angle α by which it was turned read off and the resulting beam tilt ϵ was measured. The error on ϵ was

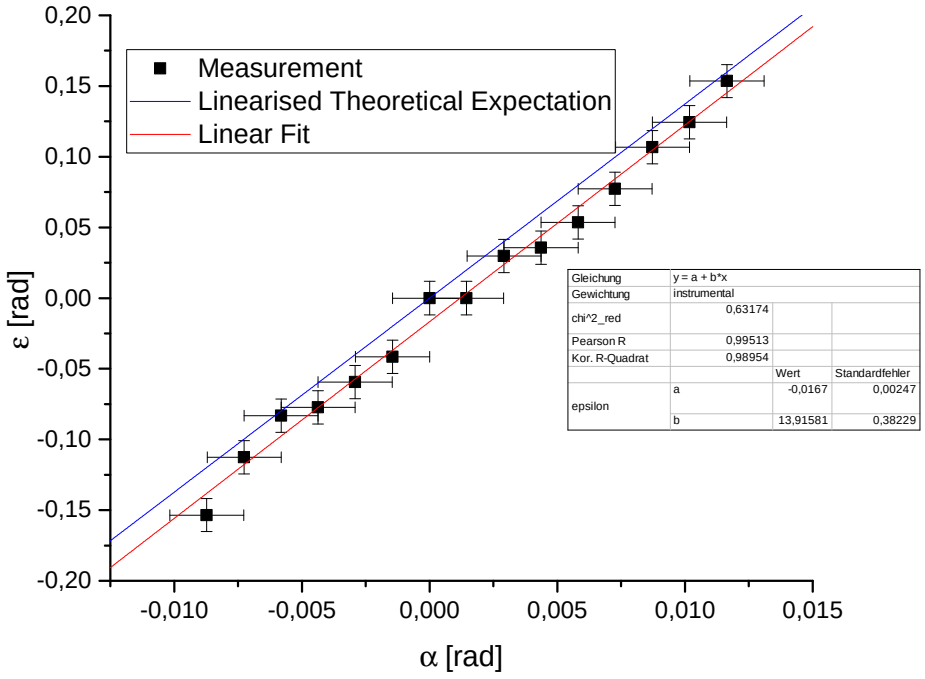

Figure 7.4: Verification of the method for measuring module tilt

calculated according to (7.1) by gaussian error propagation as:

$$\delta\epsilon = \frac{\sqrt{(\frac{\delta\Delta x}{d_S})^2 + (\frac{\Delta x \delta d_S}{d_S^2})^2}}{1 + (\frac{\Delta x}{d_S})^2} \tag{7.13}$$

The error of a single beam spot shift was estimated based on the accuracy of the graph paper and the ambiguity in determining the end of the spot by eye as $\delta\Delta x = 1\,\text{mm}$. The error of the distance between the front and back screen positions was estimated as $\delta d_S = 1\,\text{mm}$ also.

The results are plotted in Fig. 7.4, along with a linear fit to the data and a graph of the theoretical expectation (7.12) using the following parameters:

- $n = 1.778$
- $d_L = 3\,\text{mm}$
- $R = 39.6\,\text{mm}$
- $x_1 = 278\,\text{mm}$

There is no significant deviation from the linear relation assumed in (7.12). Furthermore, the expected slope based on (7.12) and the parameters given above is $\frac{\epsilon}{\alpha} = 13.73 \pm 0.05$ while the linear fit to the data gives a slope of $\frac{\epsilon}{\alpha} = 13.9 \pm 0.4$. The deviation of the linear model from the measurement is below one standard deviation, and thus not significant. The fitted curve has an offset which is larger than three times the fit error. This indicates that the alignment of the zero-positions of the rotating stage and the screen was slightly off. The alignment offset is not a problem for the measurement of the module tilt, because only the change in the modules tilt as the local cooling flow is switched on is of interest. In conclusion the method works and the theoretical description is does not deviate significantly from the measurement result.

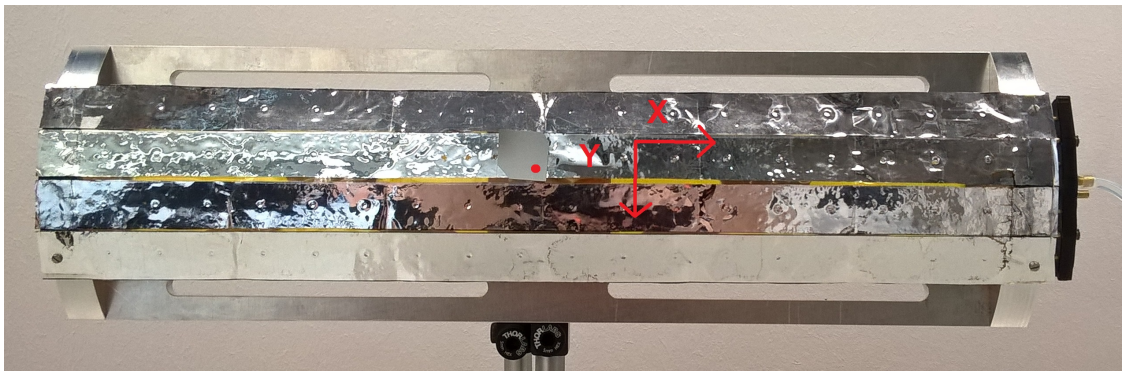

Figure 7.5: Picture of the layer 4 module prototype used for the measurements. The arrows indicate the coordinate system as used in this chapter, the dot marks the approximate reflection point.

7.4 Measurements

There were six sets of module tilt measurements carried out in total:

- measurements with local helium flow
  - on the layer 4 module prototype (Fig. 7.5)
    - beam reflected off the central mirror
  - on the layer 3 module prototype (Fig. 7.6)
    - beam reflected off the central mirror
    - beam reflected off the mirror near the edge of the module
- measurements with local air flow
  - on the layer 4 module prototype (Fig. 7.5)
    - beam reflected off the central mirror
  - on the layer 3 module prototype (Fig. 7.6)
    - beam reflected off the central mirror
    - beam reflected off the mirror near the edge of the module

The mirror used in the layer 4 module prototype measurements was the $2 \times 2\,\mathrm{cm}^2$ large and 0.3 mm thick glass mirror. The mirrors used in the layer 3 module prototypes measurements were the $2 \times 6\,\mathrm{cm}^2$ large and $50\,\mu\mathrm{m}$ thick glass mirrors. For all measurements, the volume flow of the gas used was measured with a rotameter (one calibrated for helium, another one calibrated for air), and the gas pressure was measured using barometers. The layer 4 module prototype was mounted on the same breadboard as the remainder of the optical setup, while the layer 3 module prototype was mounted on a separate mount on the side

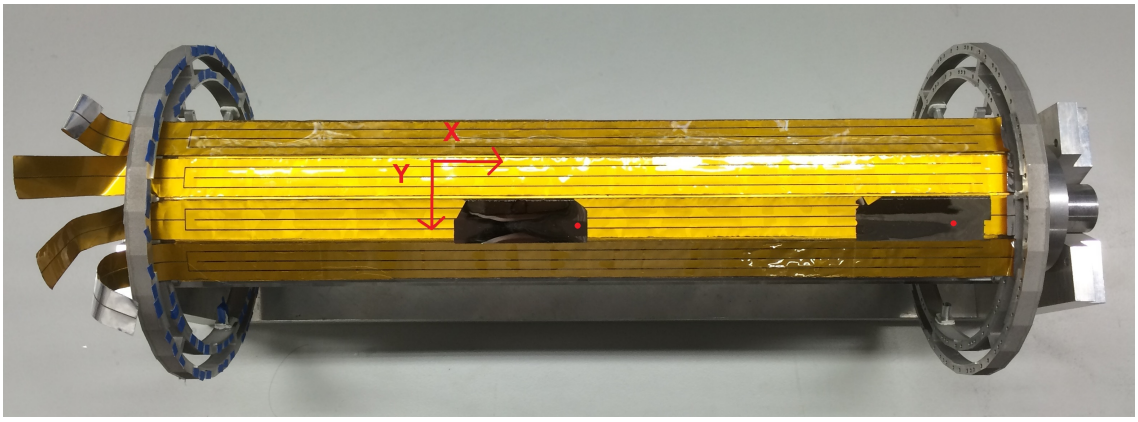

Figure 7.6: Picture of the layer 3 module prototype used for the measurements. The arrows indicate the coordinate system used in this chapter, the dots mark the approximate reflection points.

Table 7.1: Setup Parameters of the Module Tilt Measurements

Measurement	n	d_L [mm]	R [mm]	x_1 [mm]	d_S [mm]
layer 4, central mirror, helium flow	1.778	3	39.6	288	134
layer 3, central mirror, helium flow	1.778	3	39.6	417	138
layer 3, peripheral mirror, helium flow	1.778	3	39.6	403	138
layer 4, central mirror, air flow	1.778	3	39.6	274	135
layer 3, central mirror, air flow	1.778	3	39.6	414	135
layer 3, peripheral mirror, air flow	1.778	3	39.6	403	138

of the breadboard that carried the remaining optical components. The parameter values used in the evaluation of (7.12) and (7.1) are given in table 7.1.

In all measurements, the uncertainties are based on the read-off accuracy of the respective measurement device. For the air rotameter, this corresponds to an uncertainty of $0.025\,\frac{\mathrm{Nm}^3}{\mathrm{h}}$, for the helium rotameter one of roughly $1.1\,\frac{\mathrm{Nl}}{\mathrm{min}}$. The estimated error for the barometer used in the helium measurements was 0.05 bar, for the one used in the air measurements the estimated error was 0.25 bar. The density dependency of the rotameters was corrected for using (6.1) and converted to flow velocities using (6.2). As with the flow induced vibration measurements, coolant gas pressure and normed gas flow were correlated (Figs. 6.1 and 6.2). Thus (6.4) and (6.5) were used to estimate the uncertainties of the coolant gas flow. The parameters used for these estimates are given in tables 7.2 and 7.3.

Since (7.1) was used to calculate the beam tilt ϵ_i, (7.13) was used to calculate the uncertainties for ϵ_i, $\delta\epsilon_i$. The parameters used for this were the uncertainty of the beam spot position $\delta\Delta x = 1\,\mathrm{mm}$ and the uncertainty of the distance between the front and back positions of the screen $\delta d_S = 1\,\mathrm{mm}$. In (7.12), the errors of the lens parameters d_L, n, and R were assumed to be negligible. The uncertainty of α was then calculated according to

measurement	$\tilde{p}$ [bar]	q [Nl/min]	$\chi^2_{red.}$
layer 4	1	75.7	0.52
layer 3, near edge	0.98	57.5	0.24
layer 3, near center	0.97	58.2	0.24

Table 7.2: Fit parameters for the helium flow uncertainty estimate

measurement	correlation coefficient
layer 4	0.95389
layer 3, near edge	0.98909
layer 3, near center	0.99352

Table 7.3: Correlation coefficients used for the air flow uncertainty estimate

module	mirror position	total tilting angle [rad]
layer 4	center	0.0319 ± 0.0015
layer 3	center	0.0053 ± 0.0009
layer 3	edge	0.004 ± 0.001

Table 7.4: Scale of module deformation when switching on local helium flow

Gaussian error propagation as:

$$\delta\alpha = \sqrt{\left(\frac{\delta\epsilon}{2}\frac{d_L\,(1-n)+R}{x_1\,(n-1)+R}\right)^2 + \left(\frac{\epsilon}{2}\frac{d_L\,(1-n)+R}{(x_1\,(n-1)+R)^2}\delta x_1\,(n-1)\right)^2} \tag{7.14}$$

with an estimated uncertainty of the distance between mirror and lens of $\delta x_1 = 2\,\mathrm{mm}$.

7.5 Results

7.5.1 Comparison of Layer 3 and Layer 4

Scale of Deformation

The tilting of the module when increasing the local flow is shown in Fig. 7.7. The most striking difference is the one between the layer 4 module prototype and the layer 3 module prototype. The layer three module prototype tilts five to six times less than the layer 4 module prototype, although the applied local flow is similar. The layer 4 tilt happens almost exclusively in the vertical direction, whereas the tilt in the horizontal direction is far smaller (Fig. 7.7). The proposed flow speed for the local helium cooling is $20\,\frac{\mathrm{m}}{\mathrm{s}}$ [11, 12]. This implies a total layer 4 module tilt of (Figs. 7.9 and 7.10):

$$\sqrt{\left(\alpha_x(0) - \alpha_x\left(20\frac{\mathrm{m}}{\mathrm{s}}\right)\right)^2 + \left(\alpha_y(0) - \alpha_y\left(20\frac{\mathrm{m}}{\mathrm{s}}\right)\right)^2} = 0.0319 \pm 0,0015\,\mathrm{rad}$$

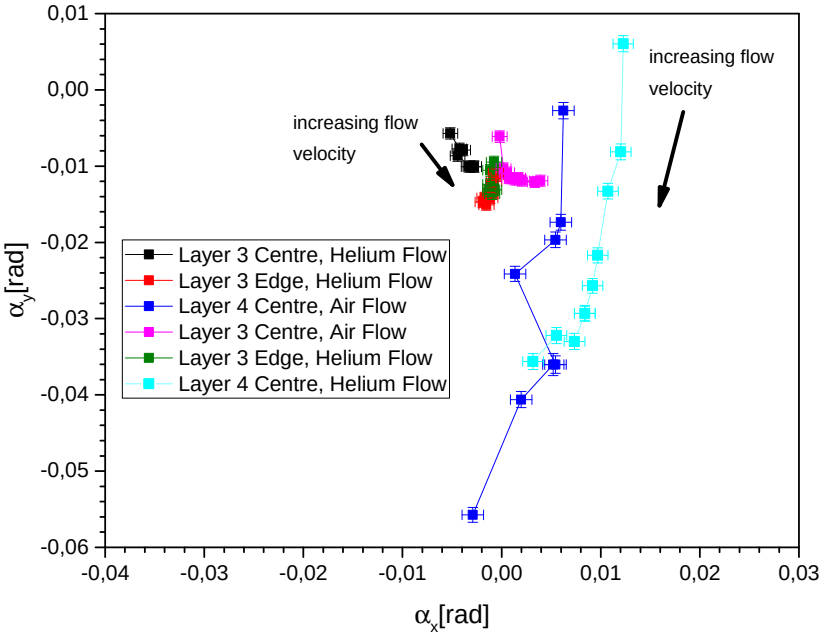

Figure 7.7: Overview of the observed module tilting angles in the $\alpha_x - \alpha_y$ plane. The topmost data-point in every set is the tilt of the module when no flow is applied. The other points of the same color mark the measured module tilt in x and y direction as the flow is gradually increased.

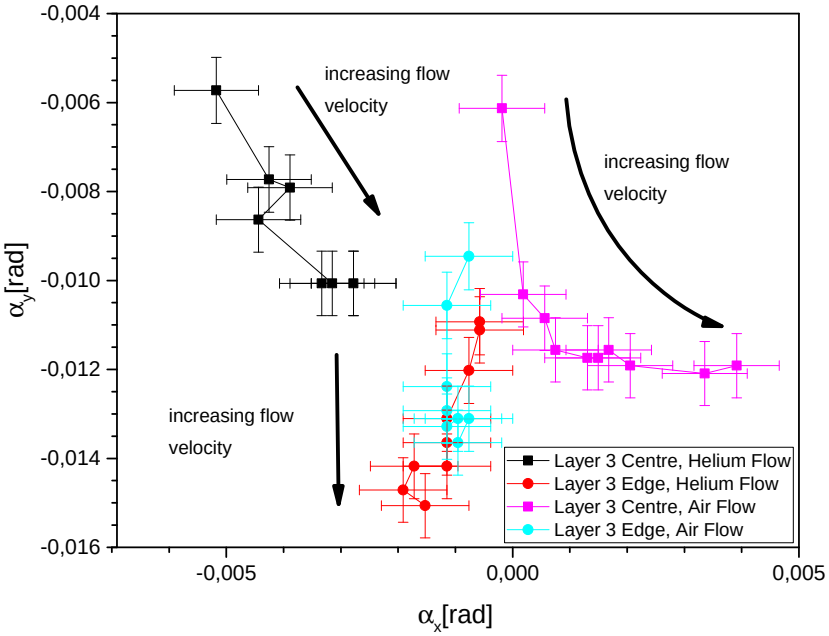

Figure 7.8: Zoomed in view of Fig. 7.7

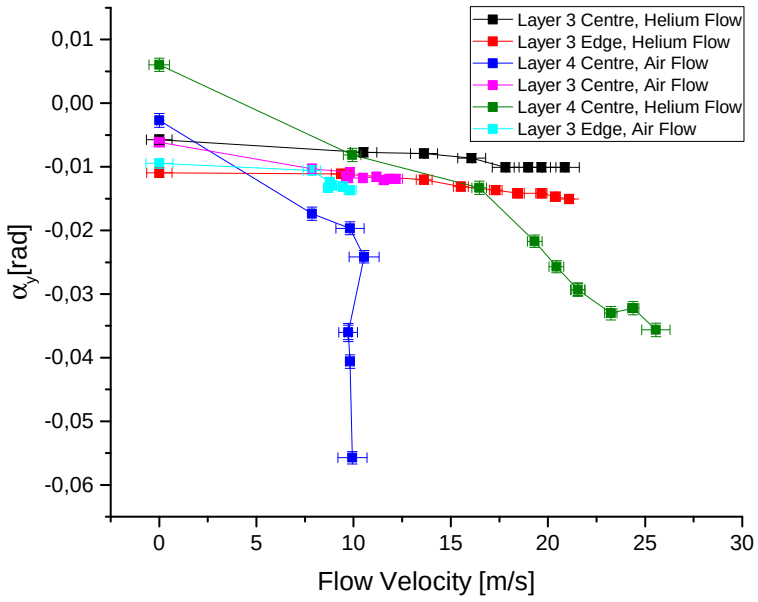

Figure 7.9: Vertical module tilt gas flow dependency

Since the mirror used in those measurements was thick enough[1] not to be bent easily, the relative displacement of the parts of the module where the mirror was glued on (which were roughly one cm apart) was about $0.0318 * 1\text{cm} = 318\,\mu\text{m}$. This is large enough to influence detector resolution. For comparison, the module tilting angles incurred by switching on $20\,\frac{\text{m}}{\text{s}}$ of local helium flow for the layer 3 module prototype are given in Table 7.4. The deformation is smaller by almost an order of magnitude.

Doing the same conversion to a length scale as for layer 4, one gets $5.3\,\mu$m for the measurement near the center of layer 3, and $4\,\mu$m near the edge of layer 3. These values make the layer 3 deformation seem insignificant in terms of detector resolution. However, the mirrors used in the layer 3 prototype were only $50\,\mu$m thick, and directly built into the module. The layer 4 mirrors the other hand were to glued on to the module. Because of this difference one cannot say that the force of the layer 3 deformation was strong enough to displace part of the mirror by that length scale. Still, because the mirror and the parts of the module have sizes in the cm range, these length scale estimates should at least indicate the order of magnitude of the effect. Since it is well below $50\,\mu$m, it seems to be negligible
.

Shape of Module Deformation

The next big difference between the deformation curves of the layer 3 and layer 4 prototypes is their shape (Figs. 7.7 and 7.8). Because there is no data for the behavior of the layer 4 module near its edge, only the data taken at the central mirror positions can be compared. The shape of the deformation of the layer 4 module is dominated by the tilt in y direction, with a slight tendency towards decreasing α_x (Fig. 7.7). The shape of the layer 3 module deformation has roughly equal components in α_x and α_y, with the movement being mainly in α_y for low flow values and mainly in α_x for high flow values (Fig.7.8). Overall, the two modules seem to deform in two completely different ways. This suggests that the underlying mechanics are just as different. The difference in mechanical properties can be attributed to three causes: different structural integrity, different mirrors, and different mounting and gas distribution systems.

The structural integrity of the two modules differs because the glass plates of the layer 4 module were in some cases broken into many smaller parts. This decreased the mechanical stability of the module. The stability of the module was further decreased by the fact that some of the v-shapes transporting the local cooling flow were bent and deformed. Because there was no fully intact layer 4 module prototype available, this systematic uncertainty due to different structural integrity could not be eliminated. However, it is to be expected that the module 3 layer prototype was free of this kind of systematic distortion, making the layer 3 measurements more reliable.

The mirrors on the two prototypes are very different concerning how they distort the measurement. The layer 4 module had a 3 mm thick glass mirror glued onto its surface with instant glue. This added a lot of mass and a lot of stiffness to the module, and changed the overall geometry and mass distribution. On the other hand, the layer 3 module prototype was constructed with two glass plates replaced by metallized glass plates (of the same dimensions), which were then used as mirrors. Here the influence of the mirrors on the measurement is negligible. So while the added mirror is another systematic distortion of the layer 4 measurements, the layer 3 measurements were not affected in this way.

Finally, the gas distribution systems were different, with the layer 3 module prototype using a recent design built to make the flow speeds and pressures in the different gaps as equal as possible. The layer 4 module prototype used an older design, which caused different pressures and velocities across the different gaps. Depending on the cause of the module deformation, this may have led to bigger internal stresses in the layer 4 module prototype, and thus to a bigger deformation, as well as a different behavior (because the direction of the dominant forces was different). So, apart from the two systematic influences of structural integrity and mirror placement, it may be that the difference in the evolution of the deformation is due to the change in the gas distribution systems.

[1] 0.3 mm

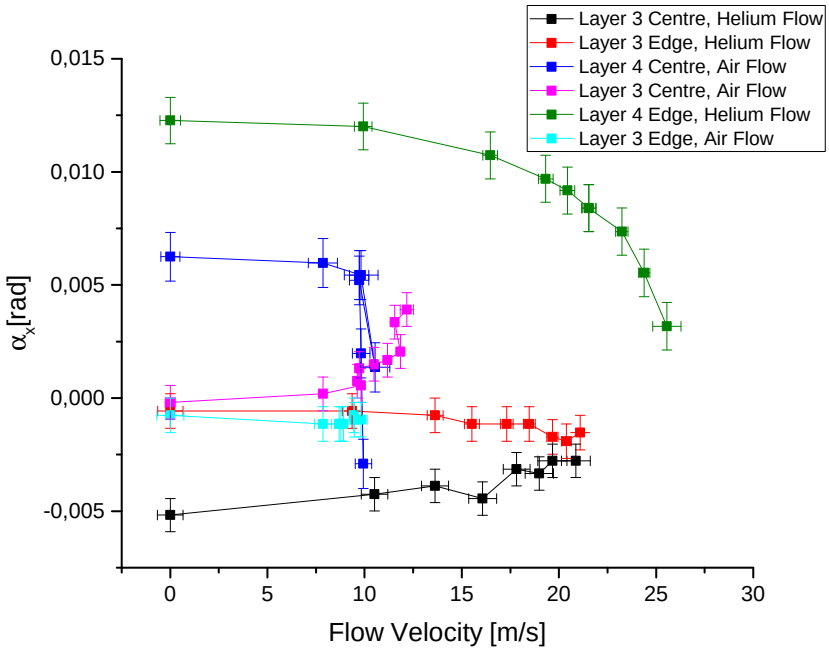

Figure 7.10: Horizontal module tilt gas flow dependency

7.5.2 Comparison of Central and Peripheral Deformation

Another possible comparison is that between the module deformation near the edge of the layer 3 module, and the module deformation near the center of layer 3. Here, there is no significant difference in the scale of the deformation, but a difference in the shapes (Fig.7.8). The Module tilts by about the same angle in α_y near the center and near the edge. But there is a measurable contribution of α_x in the central deformation which is missing in the near-edge deformation.

One possible explanation of this behavior is that the connection of the module to the end-ring. This increases the stability against deformation near the edge of the module, by imposing a boundary condition on the module surface, forcing it to follow the endring position.

Another explanation could be asymmetric (in x) properties of the gas flow, such as a pressure gradient. A pressure gradient should be expected, since it is used to accelerate the gas.

7.5.3 Tilt as a Function of Flow Speed and Pressure

There is one comparison that has not yet been mentioned: the comparison of air-flow induced and helium-flow induced module tilt. Looking at the path of the deformation (Figs. 7.7 and 7.8), there seems to be very little difference, considering that the different starting points are due to different setup alignment. The general scale of the tilting is

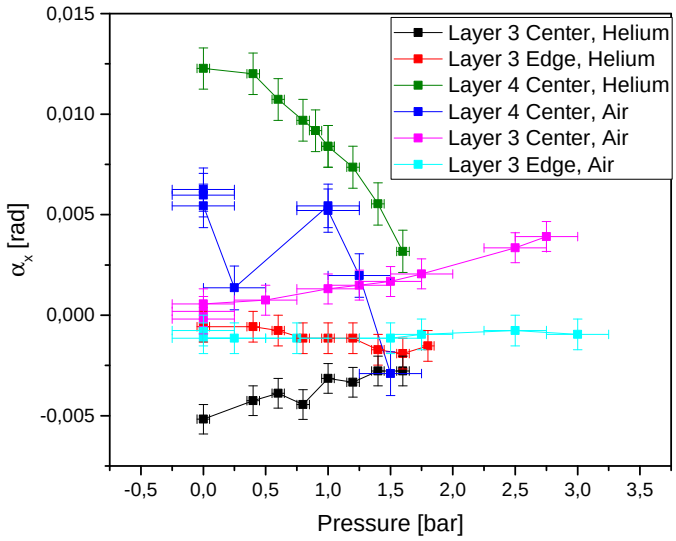

Figure 7.11: Pressure dependency of the horizontal module tilt

similar. The paths of the module tilt through the $\alpha_x - \alpha_y$ plane are similar too.

However, the same is not true if one looks at the flow velocity dependency of the module tilt (Figs. 7.10 and 7.9). The scales in which the flow velocity is varied differ significantly between air and helium, but this difference is not reflected in the angles observed. Furthermore, for the layer 4 air measurement, the relation of flow and tilting angle does not seem to be bijective. The flow velocity does not change although the module tilt is significantly changed. This could be due to the large uncertainties of these measurement, though.

To try to resolve this problem and explain the similarity of the deformation path shapes and scales, one can consider the pressure dependency of the module tilt instead (Figs. 7.11 and 7.12). Similar module tilt happens at similar pressures, for both helium and air. Because the pressure was used to adjust the flow velocity, this could indicate that pressure is the parameter determining the module deformation.

However, the precision of the pressure measurements is low. This means that at low pressures, this statement can not be tested. A similar problem happens to the flow velocity for high pressures. For high pressures, the flow velocity does not increase, because fluid turns compressible. So instead of accelerating the gas, pressure increases at high pressures lead to higher densities. To a lesser degree, the same thing happened in the flow induced vibration measurements (chapter 6).

Over the whole range of pressures, neither flow speed nor pressure are satisfactory parameter choices. Pressure is imprecise at low pressures, and flow speed changes slowly or not at all at high pressures. The uncalibrated[2] rotameter values describe the entire range

[2]See (6.1) and its discussion for more detail on rotameter calibration

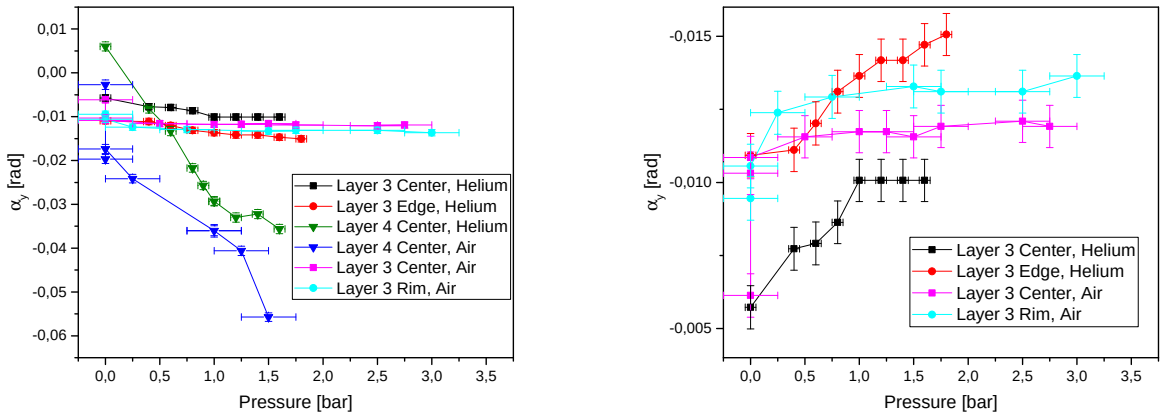

Figure 7.12: Pressure dependency of the vertical module tilt(left: overview right: only the layer three curves)

adequately, but do not correspond to a physical flow quantity. For a better parameter, one might choose flow momentum instead of flow velocity, or mass flow instead of volume flow. These quantities have a physical interpretation. They can still be used when the flow turns compressible, because they are affected by increasing density.

7.6 Conclusion

In the beginning of this chapter it was mentioned that the tilt of the module was originally noticed because the resulting beam tilt inhibited the interferometric measurements. This problem mainly occurred during measurements on the layer four module prototype. Since a sufficiently large module deformation due to cooling flow would either need to be removed, or accounted for during alignment of the setup, a dedicated measurement of this phenomenon was done. The main results of these measurements are:

1. The module tilt is indeed dangerously large in the case of the layer 4 module.
2. The module tilt seems small enough to be negligible in the case of the layer 3 module.
3. The module tilt is neither symmetric nor homogeneous along the length of the module.

It will be necessary to either make the modules more stable, or to do the alignment while the cooling system is already active and running. To prevent overheating of the detector, the latter is necessary in any case. A more stable design on the other hand would mean an increased material budget. Thus alignment with the cooling system running is the obvious choice. This has the advantage of not making additional work necessary, because the detector would have to be aligned anyways.

Chapter 8

Interferometric Measurement of Module Deformation

In chapter 7, the static module deformation induced by the local cooling flow has been measured as a tilting angle. To double check these results, and gain a better insight into the actual displacements associated with the module tilts, another series of measurements of flow induced static module deformation has been carried out. This time, the measurements were done using the Michelson Interferometer. This means losing directional information, but in turn one gains the ability to directly observe the actual module displacement, instead of inferring it indirectly, as in chapter 7. This chapter describes these measurements, their results, and their interpretation.

8.1 Measurements

Measurements were performed on both the layer 4 and the layer 3 module prototype.

The setup was the same as described in the chapter on the Michelson Interferometer (Fig. 4.1), with one important modification: Because the module tilt in y direction of the layer 4 module is so large (Fig. 7.7), in measurements of the layer 4 module prototype a convex lens was added. The convex lens was placed in front of the mirror on the module prototype, with a distance of precisely one focal length (4 cm).

The lens focused the collimated beam on one spot on the surface of the mirror. If the beam was then reflected at an angle, the reflected beam would necessarily originate from the focal point of the lens. Because of this, the lens merely collimates the beam again, and displaces it slightly. Thus, strong tilts of the mirror on the module lead only to small displacements of the reflected beam. This made it possible to have the beams from the reference mirror and the beam from the module mirror overlap at the photodiode, both with no local flow, and high local flow, without readjusting the mirrors in between. Thus, the interference of the two beams could be observed throughout the entire process of turning on the flow.

As the beam passing through the added lens was mirrored around the center of the

Figure 8.1: Laser reflection points in the deformation measurement of the layer 3 module

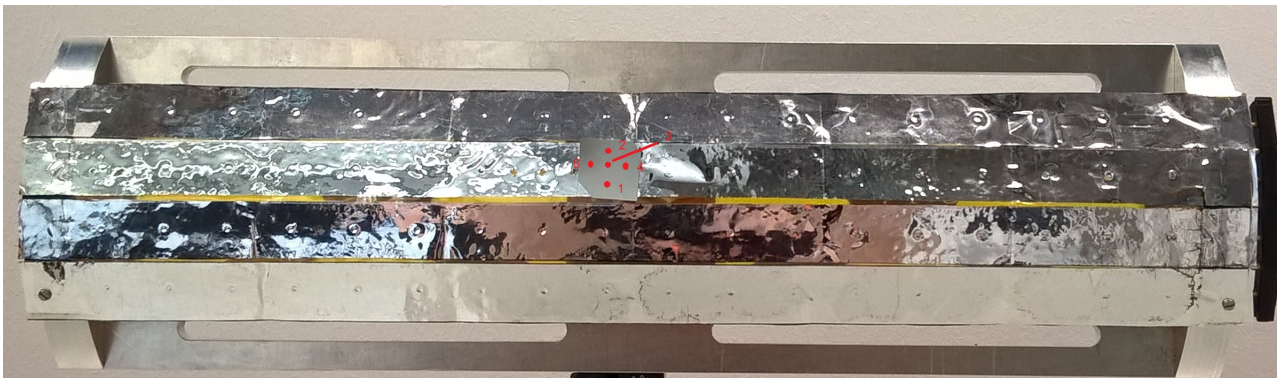

Figure 8.2: Laser reflection points in the deformation measurement of the layer 4 module

lens, the visibility of the interference was reduced, as the laser diode has a rather poor spatial coherence. However, the visibility was still high enough to distinguish the maxima and minima in the interferogram, as long as the setup was very carefully aligned.

For the layer 3 module prototype, adding the lens was not necessary, and so the standard setup described in Fig. 4.1 was used.

The measurements of module tilt show that the modules do indeed tilt when one switches on the local flow. Thus the measurements of module displacement were done not only in one, but in several places across the mirrors on the modules (Figs. 8.1 and 8.2). In each position, several[1] individual switching on procedures were recorded. When switching on the flow, the flow was first adjusted to the precise flow value aimed at using the slow valves at the helium bottle or the pressurized air supply, respectively. Then, a fast switch was used to turn the gas flow on and off quickly.

For each switching on procedure, a 2 s long interferogram was taken, with roughly one second of data before and after the flow was switched on. Thanks to the strong frequency

[1] 6 for Spots 1 and 2 on layer 4, both with helium and air, 3 for the remaining Spots on layer 4, 3 for the Spots on layer 3

Spot Position No. (Fig. 8.2)	Gas Used	Local Displacement	$[\mu m]$	
1	Air	107.1	$\pm$	6.5
1	Helium	94.4	$\pm$	9.8
2	Air	2.3	$\pm$	0.5
2	Helium	1.1	$\pm$	0.8
3	Helium	22.7	$\pm$	8.9
4	Helium	16.9	$\pm$	2.2
5	Helium	7.5	$\pm$	1.9

Table 8.1: Deformation of the layer 4 module prototype when turning on flow to 20 $\frac{\mathrm{m}}{\mathrm{s}}$ flow velocity

dependence of the flow-induced vibrations (Figs. 6.8 and 6.7), the transition from no flow to high flow is easy to identify in the interferograms.

In order to get the module deformation, several movements before and after the transition were counted by hand[2], and the alternating sum over time of these movements length was calculated. From the resulting data, the static displacement was read off as the difference of the respective averages of the module position values before and after the flow was switched on.

On the layer 3 module, all measurements were done using helium. On the layer 4 module, measurements were done with helium on all marked positions (Fig. 8.2) and additionally, with air on positions 1 and 2.

8.2 Results

8.2.1 Layer 4

The results of the measurements on the layer 4 module prototype are given in table 8.1. While the module displacements observed do vary wildly, there is a displacement significantly larger than 50 μm (position 1).

The displacement expected due to the module tilt measurements would be around 300 μm, estimating the distance between positions 1 and 2 as 1 cm. The deviation can not be explained by a large overall displacements of the whole module, since the module hardly moved at all in position 2. Part of the difference may be due to the tilt in x direction, which effectively rotates the tilting axis away from the vertical axis, meaning that a large displacement due to tilt in y may be reduced by a smaller tilt in x direction, causing displacement with the opposite sign. Some small tilt in x direction has been observed (Fig. 7.7), however, it is a lot smaller than the vertical tilt, and thus insufficient to explain why the displacement is only a third of what was expected.

[2]The automated counting algorithm used for the flow induced vibration and frequency response measurements was not reliable enough to do this.

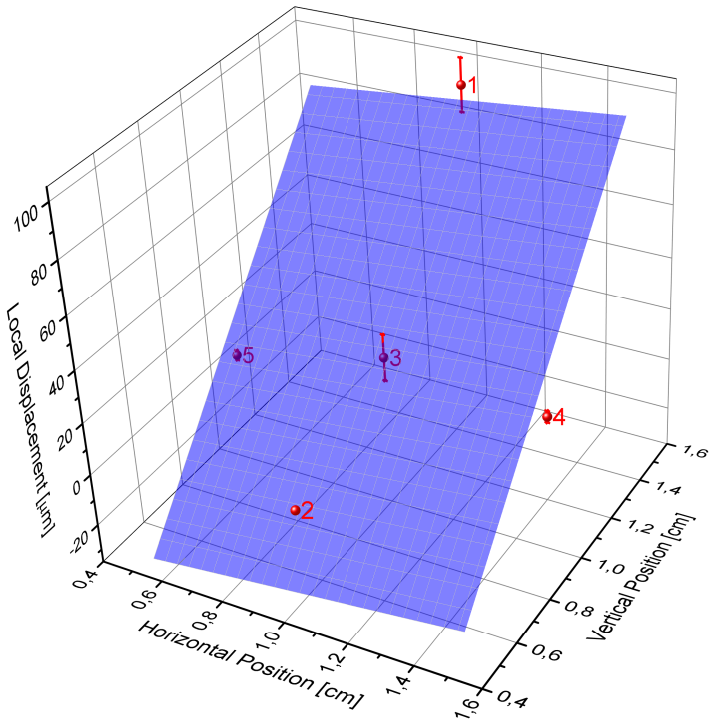

Figure 8.3: Fit of a plane surface to the layer 4 module deformation data

Comparing the measurements performed with air to those done with helium, there is a small difference of $1.1\,\sigma$ [3] for position 1 and $1.3\,\sigma$ for position 2. However, the differences are not statistically significant. This is in line with the qualitative observation made in chapter 7: The module deforms more or less the same, irrespective of which gas is used to supply the local flow.

In order to see whether the assumption of the rigid mirror is compatible with the data, a plane surface was fit to the data. Because only two positions were measured with air, only helium data was used. The model used was:

$$z\,(x, y) = z_0 + ax + by \tag{8.1}$$

where z denotes the local module displacement, z_0 is a global offset displacement fit parameter, x and y denote positions on the non-tilted mirror surface and a and b are fit parameters describing the slope of the plane in the two surface dimensions. Since the interferogram does not give information about absolute movement directions, there is a freedom in assigning relative signs to the displacement data. To account for this, the fit was repeated with changing relative sign assignments.

The result of the fit to the sign permutation with the lowest $\chi^2_{red.}$ is shown in Fig. 8.3. The fit has $\frac{\chi^2}{red.} = 0,057$, indicating that the data points don not significantly deviate from

[3] square sum of the standard errors

the plane surface model. However, such a low $\chi^2_{red.}$ also implies that he parent distribution of the distribution of data may deviate from the normal distribution. This could be due to the low number of individual points in each of the samples. The slopes determined by the fit are $a = 0.0012 \pm 0.0041$ and $b = 0.0121 \pm 0.0047$.

Since the mirror tilts are small, the slope $\tan(\alpha)$ of a surface tilted by an angle α can be approximated by that angle. Thus the slope parameters may directly be compared to the mirror tilt angles from Chapter 7. As expected from Fig. 7.7, the module tilts far stronger in vertical than in horizontal direction. However, the interferometric measurement is not precise enough to pick up the small tilt in x. The tilt in y is still far smaller than expected. The layer 4 tilt just in y was 0.0278 ± 0.0011 rad in the direct measurement. The fit parameter b differs from that by $3.3\,\sigma$. This means that the difference is just on the edge of significance. However, $\chi^2_{red} = 0.057$ is rather low, and could indicate that the errors were overestimated. Since a fit with a too small χ^2 also underestimates the standard errors of the fit parameters, the error of b may have been underestimated. In that case, the observed difference would not be significant.

8.2.2 Layer 3

The local displacement of the mirror surface on the layer 3 module prototype resulting from turning on the flow is shown in Fig. 8.4. At all 24 spot positions, the average module displacement is smaller than $2\,\mu$m, meaning that the module does not deform so strongly that the difference is of any consequence to the detector resolution. In fact, the observed deformations are of about the same size as the flow induced vibration amplitudes (Fig. 6.4). Therefore there is a high chance of the observed local displacements being not due to static module deformation, but the result of flow induced vibration. This means that the actual static local displacement of the module could possibly be even smaller.

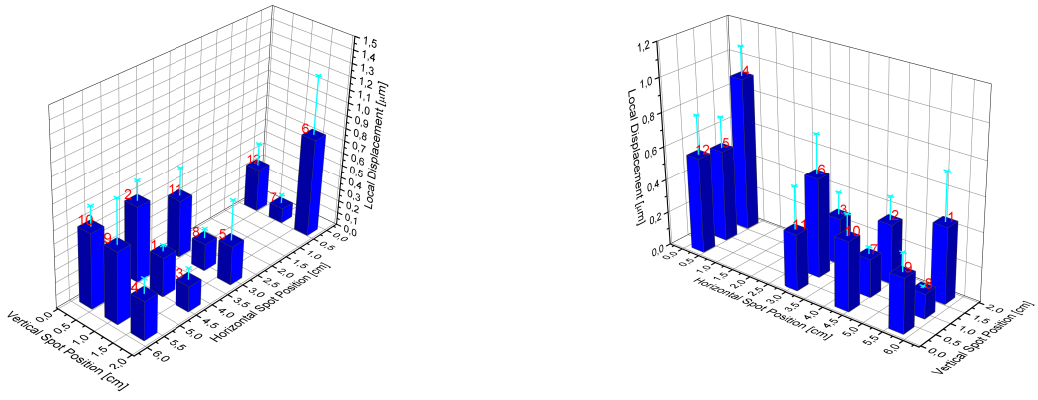

(a) Central mirror (b) Peripheral mirror

Figure 8.4: Deformation of the layer 3 module prototype

In principle, by taking the averages over many more module position values - both before and after local flow is switched on - such a deformation could be detected by the method used here. In practice however, the ambiguity in determining and counting the individual module movements contributing to the alternating sum introduces an error, which does not decrease with increasing the number of averaged samples. The error does not decrease because the alternating sum is an integrated quantity, and carries with it all previous errors. So as the sample sizes increases, so does the total amount of wrongly attributed turning points. Thus static displacements smaller than the average vibrational displacement amplitude cannot be detected by this method. This is not a problem, however, because the vibration amplitudes themselves are so small.

Comparing the results in Fig. 8.4a with the relevant entry in table 7.4 allows another interesting conclusion about the module deformation: it happens on rather short length scales across the module surface. The mirror was observed to tilt by $0.0040(1)\,\mathrm{rad}$ and $0.0053(9)\,\mathrm{rad}$, respectively, but the module never moved by more than $2\,\mu\mathrm{m}$ in any of the positions measurements were done at. Thus the module deformation causing the tilt of the module must change at a length scale of $\frac{2\,\mu\mathrm{m}}{0.004} \approx 0.5\,\mathrm{mm}$ or smaller, since a constant tilt across a larger distance would cause a local module displacement larger than what was observed. However, the above consideration assumes that the 12 positions on the mirror surface where measurements were done are representative of the entire mirror surface. That does not need to be the case. If e.g. the positions where data was taken all happened to be in places where the surface hardly deformed, but the surface was deformed very strongly in other places in between, the length scale at which the tilt changes could be of the same magnitude as the distance between neighboring measurement positions, which was about $7\,\mathrm{mm}$ for direct neighbors.

8.3 Conclusion

In this chapter, the static module deformation when subject to local flow was measured as a set of local module displacements at different points on the module surface.

For the layer 4 prototype, displacements as large as $100\,\mu\mathrm{m}$ were directly observed. These could be large enough to negatively affect detector precision if they are not accounted for. Insofar the findings in this chapter agree with the conclusions from chapter 7.

An attempt was made to check whether the local displacement data are in agreement with the module tilt data from chapter 7 by fitting a plane surface to the data. But while no significant deviation could be found, the method is not precise enough and the data sample is too small to be able to draw confident conclusions.

Since the mechanical properties of the layer 4 module prototype mirror surface differ significantly from those of the actual module due to the thick and heavy mirror glued on top, the large deformation observed may differ from the deformation of an actual module[4]. At the same time, it cannot be conclusively ruled out that they do not.

[4]See also the more extensive discussion of the issue in section 7.5.1.

The layer 3 prototype, on the other hand, does not have this issue of a large and heavy additional mirror. Thus, its mechanical properties can be assumed to be very similar to those of the actual detector modules. All local static displacements found in layer 3 were smaller than $2\,\mu$m, as large as or smaller than the average amplitudes of flow induced vibrations in the module. Thus the actual deformation may be even smaller than the measurement suggests, but in any case they do not pose a threat to detector resolution.

In conclusion, a dangerously large module deformation of $100\,\mu$m was found in the layer 4 module prototype, which may or may not be a systematic effect of the measurement setup. In the layer 3 module prototype, which does not suffer from the same uncertainty, no such deformation could be observed and the largest deformation found was still smaller than $2\,\mu$m.

Chapter 9

Conclusion and Outlook

In this thesis, the effects of vibration on the layer 3 and 4 Mu3e tracking detector modules were studied, especially with regard to flow induced vibration. Furthermore, static module deformation due to coolant flow was studied.

Firstly, the frequency responses of layer 3 and 4 were measured (chapter 5). Many strong resonances were found in the range between 50 Hz and 1000 Hz. Thus, this region can be considered especially dangerous for module vibration.

Secondly, the flow induced vibration due to the local cooling flow was measured (chapter 6). At the planned cooling flow velocity of about $20\,\frac{\mathrm{m}}{\mathrm{s}}$, the maximum vibration amplitude was lower than $10\,\mu$m for both layer 3 and layer 4. The average vibration amplitudes at this flow velocity were lower than $2\,\mu$m for both layers. Both averages and maxima are significantly below the thickness of one detector chip of $50\,\mu$m. Therefore, a local helium cooling flow of $20\,\frac{\mathrm{m}}{\mathrm{s}}$ velocity is likely not to limit detector resolution.

However, much higher flow velocities should be avoided. Since at flow velocities of about $30\,\frac{\mathrm{m}}{\mathrm{s}}$ vibration amplitudes up to $39\,\mu$m were observed, the flow induced vibrations at this point can affect the detector resolution.

Modes of vibration at lower frequencies than the highest one that is large enough to be detected can not be found directly by counting maxima in the interferogram (section 4.2). To search for such hidden modes, the individual movement amplitudes found were integrated over time, and a discrete Fourier transform was performed on the result. In the medium frequency range, no dangerous amplitudes were found. But very large ($\geq 100\,\mu$m) movement amplitudes were observed in the very low frequency range ($\ll 100$ Hz). Whether these amplitudes are due to counting errors, numerical distortions, or actual module movement could not be determined conclusively.

Thirdly, the static deformation of the detector module due to the cooling flow was measured with two different techniques (chapters 7 and 8). While large deformations were observed for layer 4, these could be due to the systematic effect of the mirror used. No such deformations were observed for layer 3. While the observed deformations of layer 4 are large enough to influence detector resolution, they do not pose a significant problem. Since detector alignment will need to be done with the cooling system running to prevent overheating, any *static* displacement of the modules will not pose a problem. This does

however require the coolant flow to be kept constant.

Thus the overall conclusion is that the planned local cooling system of the Mu3e silicon pixel tracker does not impede the detector resolution, insofar as can be told by the measurements. But two open problems remain for further study: the effect of the global flow, and very low frequency vibrations.

The global flow velocity is about a factor of 5 lower than the local flow velocity [12], so one might suspect that it is not a problem. But the global flow has contact with the detector surface over a much larger area. In addition, its flow properties are very different due to the different geometry. Computational fluid dynamics calculations show a potential for flow vortices due to the interaction of global and gap flow [11]. So to be on the safe side, an experimental study of the effects of global cooling flow in terms of flow induced vibration is recommended.

Low frequency vibrations (or hidden modes) were studied in the chapter on flow induced vibration. Over the frequency range where the results were judged reliable, no vibration amplitudes relevant to vertex resolution were found. However, there are peaks at the low frequency end of the spectrum which come close to the 200 μm mark. It cannot conclusively be ruled out that these are neither numerical effects nor noise introduced by counting errors. Thus further investigation of this phenomenon is advisable[1].

[1] Examples of how one might improve upon the investigation presented in this thesis are given in section 6.3.

Appendices

Appendix A

Laser Specifications

A.1 Thorlabs CPS635F Data Sheet

Table A.1: Laser Specifications

General Specifications	
Housing Material	Aluminum
Housing Dimensions	Ø11.0 mm X 54.0 mm
Beam Shape (Collimated)	Elliptical, 5.0 mm X 1.9 mm
Operating Temperature	-10 to 50 °C
Storage Temperature	-30 to 70 °C
Operating Voltage	4.9 V to 5.2 V
Laser Safety Class	3R

Optical and Electrical Specifications			
	Min	**Typical**	**Max**
Wavelength	630 nm	635 nm	645 nm
Power	4.0 mW	4.5 mW	5.0 mW
Polarization Extinction Ratio	-	24 dB	-
Power Stability (8 hours)	-	-	2%
Power Stability (1 Minute)	-	-	1%
Axis Deviation	-	-	5 mrad
Beam Divergence (Collimated)	-	-	1.6 mrad
Focal Range (From Exit Window)	80 mm	-	Collimated
Focused Spot Diamter (100 mm, $1/e^2$)	-	30 µm	-
Operating Current	-	50 mA	70 mA

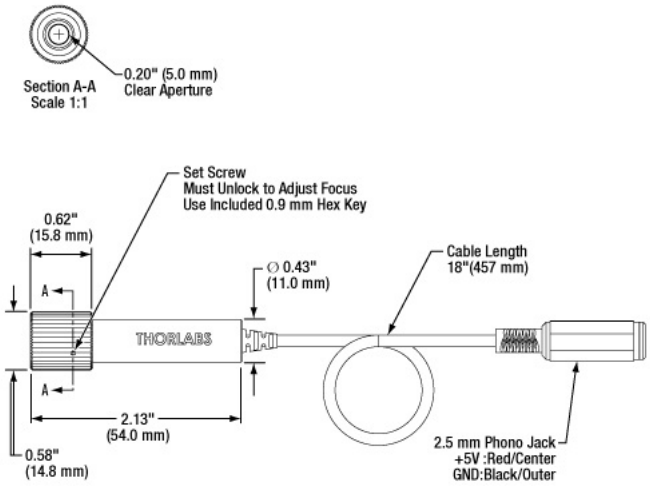

Figure A.1: Original Laser Dimensions

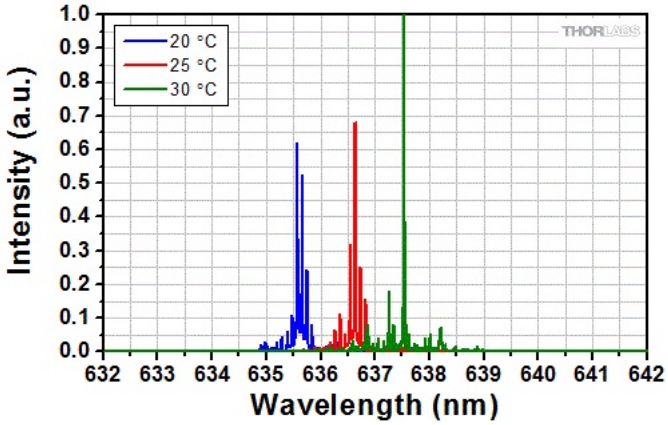

Figure A.2: Three Typical Spectra

A.2 Custom Housing

The custom housing (fig. A.3) was designed and constructed by the PI mechanical workshop. It contained the original laser diode, optics, housing and electronics, with the exception of the endcap that allowed focus adjustment (Fig. A.1). In addition it contained two absorptive grey filter plates with transmissivities of 0.25 and 0.79, respectively. The plates reduced the intensity of the laser beam after exiting the housing to below 1 mW. This was necessary in order to comply with laser safety regulations. The filter plates were placed between the diagonal parts of the main housing (fig. A.4) and the counter piece (fig. A.5). The counter piece and the filter plates were held in place by the surrounding fixation hull, which was held onto the main piece of the housing with screws (fig. A.6). At the other end of the laser, the collimation screw is screwed onto the main housing (A.7). By turning it, the laser inside the main housing is pressed against the spring separating the laser from the collimating lens. Thus the distance of laser diode and lens can be varied, and the focus adjusted. The focal adjustment can be fixed via a small hex-screw in the hull of the collimation screw. Drawings courtesy of D. Litsch.

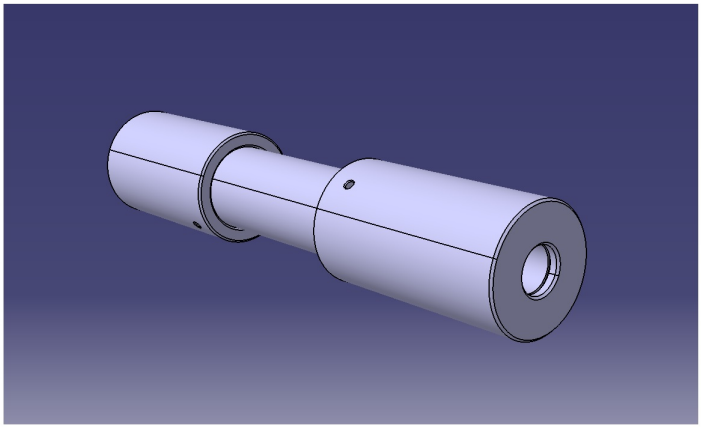

Figure A.3: The Custom Laser Housing

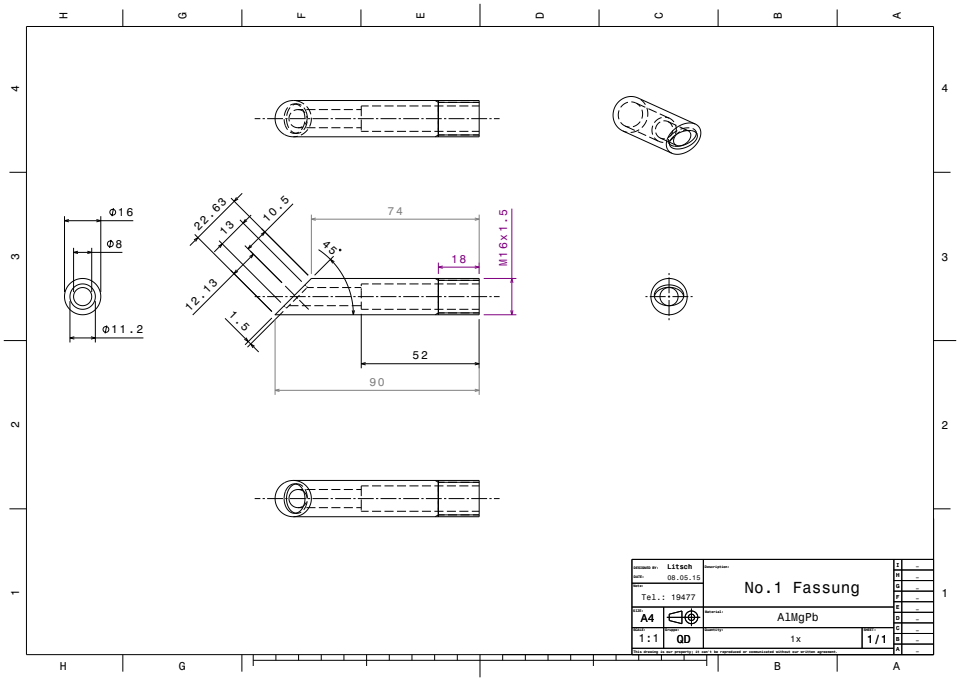

Figure A.4: Custom Laser Housing: Main Piece

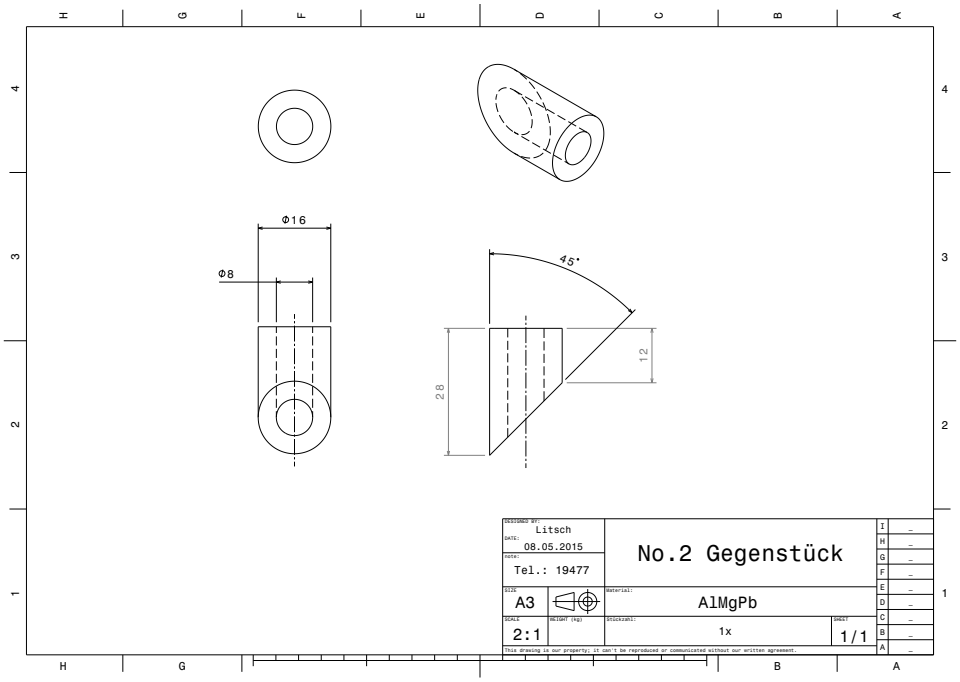

Figure A.5: Custom Laser Housing: Counter Piece

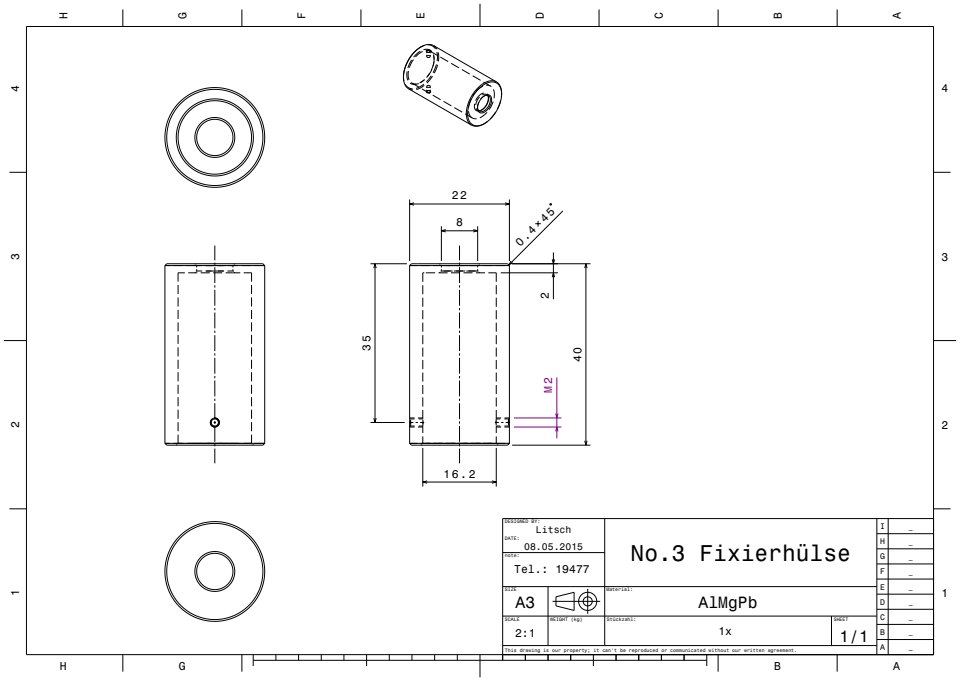

Figure A.6: Custom Laser Housing: Fixation Hull

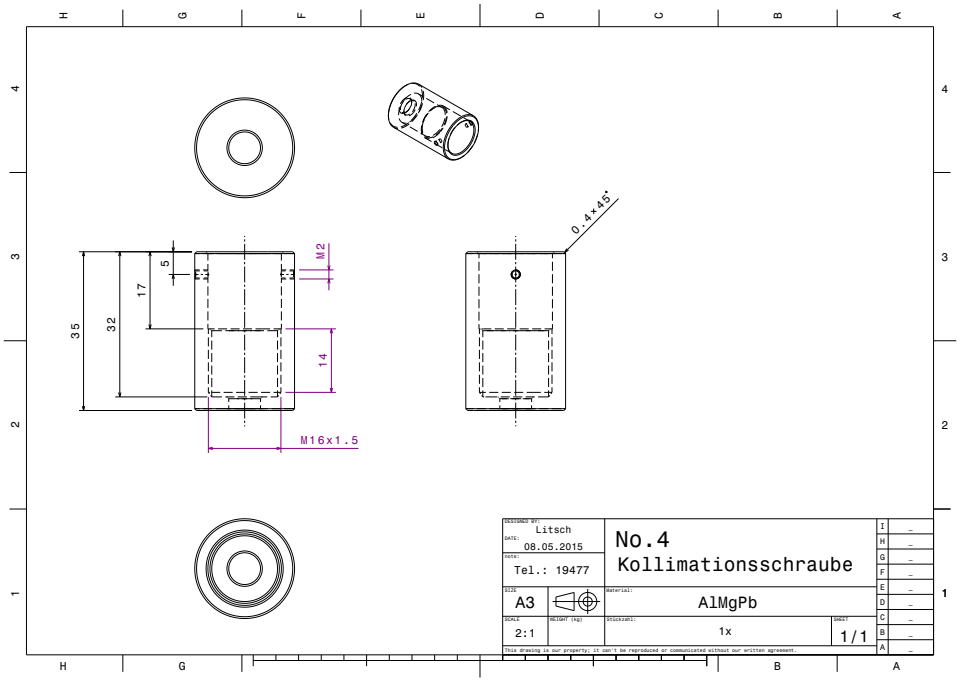

Figure A.7: Custom Laser Housing: Collimation Screw

List of Figures

List of Tables

Bibliography

[1] N. Berger et al. [Mu3e Collaboration] "*Research Proposal for an Experiment to Search for the Decay $\mu \to eee$*", 2012

[2] M. Thomson, "*Modern Particle Physics*", Cambridge University Press, 2013

[3] Wikimedia Commons, "*Standard Model of Elementary Particles*" retrieved August 2015

[4] J. Marciano et al. "*Charged Lepton Flavor Violation Experiments*" Annual Review of Nuclear and Particle Science Vol. 58: 315-341, 2008

[5] U. Bellgardt et al. [SINDRUM Collaboration], "*Search for the Decay $\mu^+ \to e^+e^+e^-$*", Nucl. Phys., B299 1, 1988

[6] R.M.Djilkibaev and R. V. Konoplich "*Rare Muon Decay $\mu^+ \to e^+e^+e^-\nu_e\bar{\nu}_\mu$*", Phys. Rev. D 79 073004, 2009

[7] K.A. Olive et al. (Particle Data Group),"*Review of Particle Physics*" Chin. Phys. C, 38, 010009 (2014)

[8] I. Peric, "*A novel monolithic pixelated particle detector implemented in high-voltage CMOS technology*", Nucl. Instrum. Meth., A582 876-885, 2007.

[9] A. Damyanova, " *Developement of a Scintillating Fibre Tracker /Time-of-Flight Detector with SiPM Readout for the Mu3e Experiment at PSI*" Master Thesis, University of Geneva,2013.

[10] P. Eckert, "*The Mu3e Tile Detector*" Ph.D. Thesis, Heidelberg University, 2015.

[11] Y. Ng, "*Finite Element Analysis of the Cooling System for the Mu3e Experiment*", Master Thesis, University of Applied Science Jena, 2015.

[12] A. Herkert, "*Gaseous Helium Cooling of a Thin Silicon Pixel Detector for the Mu3e Experiment*" ,Master Thesis, Heidelberg University, 2015.

[13] H. Augustin et. al., "*The MuPix high voltage monolithic active pixel sensor for the Mu3e experiment*", JINST 10 C03044, 2015

[14] H. Augustin, "*Characterization of a novel HV-MAPS Sensor with two Amplification Stages and First examination of thinned MuPix Sensors*", Master thesis, Heidelberg University, 2014.

[15] R. Philipp, "*Characterisation of High Voltage Monolithic Active Pixel Sensors for the Mu3e Experiment*", Master thesis, Heidelberg University, 2014.

[16] K. Weir et al., "*A Novel Adaptation of the Michelson Interferometer for the Measurement of Vibration*", J. Lightwave Technol. 10 5, 1992

[17] R. P. Austermühl, "*Analyse von Michelson-Interferometriedaten von Vibrationsmessungen eines dünnen gasgekühlten Pixeldetektors*", Bachelor Thesis, Heidelberg University, 2015

Acknowledgments

I would like to express my gratitude to Prof. Dr. André Schöning for giving me the opportunity to work in the Mu3e group and for supervising my thesis. I would like to thank Prof. Dr. Ulrich Uwer for surveying my thesis as second examiner.

I want to thank the entire Mu3e group for providing a very enjoyable work environment and their help whenever it was needed.

I am especially grateful towards Dr. Dirk Wiedner for the advice and help he gave whenever necessary. René Philipp Austermühl also deserves special thanks, as the flow induced vibration and frequency response parts of this thesis benefited tremendously from his work on the amplitude counting algorithm.

I also thank Dr. Jens Wagner, who was always ready to help. Furthermore, I thank Dominic Litsch for designing and producing a laser casing compliant with safety regulations that retained all the capabilities of the original, Thomas Wolf and Volker Schultheiss for sputter-depositing Au-Pd onto the glass plates that became the mirrors on the module surface, and Jessica Riedinger and Simon Rabenecker for constructing the layer 3 module prototype, as well as various other parts of the setup.

Erklärung

Ich versichere, dass ich diese Arbeit selbstständig verfasst und keine anderen als die angegebenen Quellen und Hilfsmittel benutzt habe.

Heidelberg, den 01.10.2015, ...